



**HAL**  
open science

# Experimental analysis of laminar spherically expanding flames

Emilien Varea

► **To cite this version:**

Emilien Varea. Experimental analysis of laminar spherically expanding flames. Other [cond-mat.other]. INSA de Rouen, 2013. English. NNT : 2013ISAM0002 . tel-00800616

**HAL Id: tel-00800616**

**<https://theses.hal.science/tel-00800616>**

Submitted on 14 Mar 2013

**HAL** is a multi-disciplinary open access archive for the deposit and dissemination of scientific research documents, whether they are published or not. The documents may come from teaching and research institutions in France or abroad, or from public or private research centers.

L'archive ouverte pluridisciplinaire **HAL**, est destinée au dépôt et à la diffusion de documents scientifiques de niveau recherche, publiés ou non, émanant des établissements d'enseignement et de recherche français ou étrangers, des laboratoires publics ou privés.

# THESE

Présentée à l'

**Institut National des Sciences Appliquées de Rouen**

En vue de l'obtention du titre de :

**Docteur de l'INSA de Rouen**

Discipline : Physique

Spécialité : Energétique

Laboratoire d'accueil : CORIA CNRS UMR-6614

Par :

**Emilien Varea**

**Experimental analysis of laminar spherically expanding flames**

Soutenue le 30 Janvier 2013

*Devant le jury composé de :*

Christine Rousselle	Professeur, Prisme, Orléans	Rapporteur
Thierry Schuller	Professeur, EM2C, Ecole Centrale Paris	Rapporteur
Gladys Moréac-Njeim	Ingenieur de Recherche, Renault S.A.	Examineur
Fabien Halter	Maître de Conférences, Prisme, Orléans	Examineur
Laurent Selle	Chargé de Recherche, IMFT, Toulouse	Examineur
Mourad Boukhalfa	Professeur, INSA de Rouen	Examineur
Vincent Modica	Maître de Conférences, Université de Rouen	Co-directeur
Bruno Renou	Professeur, INSA de Rouen	Directeur





# Abstract

Laminar burning velocity is very useful for both combustion modeling and kinetic scheme validation and improvement. Accurate experimental data are needed. To achieve this, a spherical flame with constant pressure method was chosen, since it allows high-pressure and high-temperature initial conditions. Phenomenological considerations establish a link between stretched and unstretched velocities, and the stretch factor appears to be the scalar that controls the burning velocity. It is now admitted that non-linear relation must be used in the extrapolation to zero stretch. However, deriving the equations, various expressions for the burning velocity from the spherically expanding flame can be found. A theoretical review details all the expressions and models for the burning velocity and shows how they can be obtained experimentally. Their respective limitations are also pointed out. These models were compared considering basic fuels where the Lewis number can be easily estimated. As a result of this review, it is shown that the pure kinematic measurement method is the only one that does not introduce any assumptions. This technique makes it possible to determine the real velocity at which reactants go through the fresh gas isotherm. This kinematic measurement had needed the development and validation of an original post-processing tool measuring both the propagation of the flame front and the velocity of fresh gas at the entrance of the preheat zone. Following the theoretical review, the post processing development and its validation, a parametric experimental study is presented. The new technique is extended to extract burning velocity and Markstein length relative to the fresh gas for pure ethanol, isooctane and blended fuels at high pressure. These fuels are either representative components of alternative fuels or single-component alternative fuels. An empirical correlation is proposed with corresponding error assessments.



# Résumé

La vitesse de combustion laminaire est une caractéristique fondamentale d'un mélange réactif. Elle trouve son importance dans la modélisation de la combustion turbulente (estimation de la vitesse turbulente) ainsi que dans le processus de validation et d'amélioration des schémas cinétiques (donnée de référence). Bien qu'étudiée depuis plus de 100 ans, la détermination expérimentale de cette vitesse reste compliquée se confrontant aux limitations des configurations expérimentales (bruleurs à flammes plates, Bunsen, flammes à contre-courant, . . .).

Dans ce travail de thèse, la configuration de flamme sphérique en expansion a été choisie car elle permet d'atteindre des conditions thermodynamiques initiales élevées (hautes pression/température). De plus, grâce à cette configuration expérimentale, l'étirement, effets joints de courbure et cisaillement, est pris en compte de manière simple car directement lié à la topologie sphérique de la flamme. La vitesse de combustion peut être alors extrapolée non-linéairement à étirement nul.

Considérant la flamme sphérique en expansion, il apparaît plusieurs formulations permettant de remonter à la vitesse de combustion laminaire non étirée. Ces dernières sont liées au référentiel de mesure qui est

- lié au laboratoire
- lié au front de flamme
- au taux de réaction

Ces 3 formulations, bien que différentes par définition, doivent cependant converger vers une seule et unique valeur correspondant à la vitesse de combustion laminaire à étirement nul.

Des outils de post traitement spécifiques ont été développés afin de déterminer expérimentalement ces différentes vitesses. Une étude comparant les différentes formulations pour des mélanges gazeux au nombre de Lewis bien défini (méthane :  $Le \approx 1$ , propane :  $Le > 1$ , hydrogène :  $Le < 1$ ) a été menée. Le nombre de Lewis est connu pour modifier la dynamique de la flamme en agissant sur les diffusivités (thermique/moléculaire). Au vu des résultats, il est montré que la formulation associée au front de flamme permet d'extraire une vitesse de combustion s'abstenant de toute hypothèse. Cette technique, purement cinématique, a été ensuite appliquée pour déterminer la vitesse de combustion de mélanges isooctane/éthanol et leur dépendance en pression (jusqu'à 10bar). Ces mélanges de carburant sont représentatifs des carburants alternatifs à l'essence classique. Une base de données utile à la validation des schémas cinétiques est ainsi proposée.

# Contents

<b>Abstract</b>	<b>iii</b>
<b>Résumé</b>	<b>v</b>
<b>List of Tables</b>	<b>xi</b>
<b>List of Figures</b>	<b>xvii</b>
<b>Nomenclature</b>	<b>xix</b>
<b>I Introduction</b>	<b>1</b>
I.1 Background . . . . .	1
I.2 Laminar Burning Velocity . . . . .	2
I.3 Scientific Background . . . . .	5
I.3.1 Experimental Configuration . . . . .	5
I.3.2 The spherical expanding flame configuration. . . . .	6
I.4 Purpose of this study . . . . .	9
I.5 Structure of the dissertation. . . . .	10
<b>I Theoretical background</b>	<b>13</b>
<b>II One-dimensional flame</b>	<b>15</b>
II.1 Laminar Premixed Flame: Structure . . . . .	15
II.2 Laminar Premixed Flames: 1D Equations . . . . .	18

---

II.3	Flame speed definitions . . . . .	25
II.3.1	Definition . . . . .	25
II.3.2	Absolute and Displacement Speeds. . . . .	26
II.4	Concluding Remarks. . . . .	28
<b>III</b>	<b>From planar to stretched flames</b>	<b>31</b>
III.1	Stretch definition . . . . .	31
III.2	Stretched flames in literature . . . . .	35
III.2.1	Extrapolation to zero stretch. . . . .	42
III.2.2	Markstein lengths / Markstein numbers: analytical solutions . . . . .	44
III.3	Concluding Remarks. . . . .	48
<b>IV</b>	<b>On the determination of the consumption speed of spherically expanding flames</b>	<b>49</b>
IV.1	Consumption speed under the infinitely thin flame assumption. . . . .	50
IV.2	Consumption speed in finite flame thickness . . . . .	53
IV.2.1	Models for consumption speed . . . . .	56
IV.3	Concluding Remarks. . . . .	61
<b>V</b>	<b>Conclusion of the Theoretical Part</b>	<b>63</b>
<b>II</b>	<b>Experimental setup and results</b>	<b>67</b>
<b>VI</b>	<b>Experimental design and post-processing</b>	<b>69</b>
VI.1	Experimental Design . . . . .	70
VI.1.1	High pressure and temperature facility. . . . .	70
VI.1.2	Optical diagnostics . . . . .	72
VI.2	Post processing algorithm . . . . .	78
VI.2.1	Absolute flame speed estimation . . . . .	78
VI.2.2	Fresh gas velocity measurement . . . . .	80
VI.2.2.1	Test phase. . . . .	83

---

VI.3	Concluding Remarks. . . . .	86
<b>VII</b>	<b>Measurement of the Unstretched Laminar Burning Velocity from the Flame and Displacement Speeds</b>	<b>89</b>
VII.1	Methane/Air flames . . . . .	89
VII.1.1	Laminar flame speed measurements and comparison with literature . . . . .	89
VII.1.2	Fresh gas velocity measurements. . . . .	90
VII.2	Isooctane/Air flames. . . . .	97
VII.3	Ethanol/Air flames . . . . .	98
VII.4	Conclusion. . . . .	106
<b>VIII</b>	<b>On the experimental determination of consumption speed</b>	<b>109</b>
VIII.1	Consumption Speed from Mitcheson's formulation . . . . .	110
VIII.2	Bradley's and Poinot's Models . . . . .	114
VIII.3	Conclusion. . . . .	116
<b>IX</b>	<b>Flame response to stretch</b>	<b>119</b>
IX.1	Velocity . . . . .	119
IX.2	Markstein lengths . . . . .	125
IX.3	Conclusion. . . . .	131
<b>X</b>	<b>Ethanol-Isooctane Blends</b>	<b>133</b>
X.1	Numerical method. . . . .	137
X.2	Correlation description . . . . .	138
X.3	Results and discussion. . . . .	139
X.3.1	Results for atmospheric fuel/air flames . . . . .	139
X.3.2	Pressure effect . . . . .	143
X.3.3	Correlation validation . . . . .	145
X.4	Conclusion. . . . .	147



---

<b>III</b>	<b>Conclusion &amp; Appendixes</b>	<b>149</b>
<b>XI</b>	<b>Conclusion</b>	<b>151</b>
XI.1	Summary . . . . .	151
XI.2	Perspectives . . . . .	154
<b>A</b>	<b>Lewis number calculation</b>	<b>157</b>
A.1	Lewis number calculation . . . . .	158
<b>B</b>	<b>Confined spherically expanding flame: a criterion for pressure rise</b>	<b>161</b>
	<b>Bibliography</b>	<b>163</b>

# List of Tables

III.1	Markstein length evolution against Lewis numbers.. . . . .	48
VI.1	Extracted values of unstretched propagation speed $S_f^0$ and burned gas Markstein length $L_b$ for different seeding densities.. . . . .	74
IX.1	Stretch and Lewis number effects on burned gas density . . . . .	124
X.1	Experimental conditions of ethanol, isooctane and blends . . . . .	136
X.2	Correlation parameters $u_{n,i}^0$ from Eq. X.4 and $\beta(i)$ from Eq. X.8. . . . .	141
X.3	Dependence of pressure parameter $\beta$ with equivalence ratio . . . . .	144



# List of Figures

I.1	Marinov and Konnov models for an ethanol/air flame. P=0.1 MPa, T=300 K. . . . .	4
I.2	Laminar flames configurations. . . . .	5
I.3	Methane maximum velocity over the years . . . . .	6
I.4	Visualization sequence of a stoichiometric methane/air flame . . . . .	7
I.5	Animation of a propagative stoichiometric methane/air flame at P=0.1 MPa, T=298 K, <i>In pdf version, please press play button in the control bar above.</i> . . . . .	8
II.1	One dimensional flame: Model 1 . . . . .	16
II.2	One dimensional flame: Model 2 . . . . .	17
II.3	One dimensional flame: Model 3 . . . . .	17
II.4	Computed profiles . . . . .	25
II.5	Kinematic velocity scheme. . . . .	27
III.1	Straining and curvature scheme . . . . .	32
III.2	Curvature and strain effect on stretched flame . . . . .	34
III.3	Representation of stretched flames . . . . .	35
III.4	Stagnation plane flame. Stretched fresh gases velocity determination. . . . .	37
III.5	Stagnation plane flame, velocities and boundary conditions. . . . .	38
III.6	Visualization sequence of a stoichiometric methane/air flame . . . . .	39
III.7	Visualization sequence of a stoichiometric methane/air flame . . . . .	39
III.8	Methane maximum velocity over the years . . . . .	43
III.9	Comparison of the non-linear and linear relationships . . . . .	43

III.10	Variation of Markstein lengths across the flame front. . . . .	47
IV.1	Scheme of a spherical infinitely thin flame . . . . .	50
IV.2	Scheme of a spherically finite flame thickness. . . . .	54
IV.3	Evolution of the quantity $\rho Y_k$ assuming a linear variation within the flame thickness. 56	
IV.4	Consumption speed formulations. . . . .	60
V.1	Overview of the burning velocities formulations. . . . .	65
VI.1	Experimental apparatus. . . . .	71
VI.2	Experimental design pictures. . . . .	72
VI.3	Optical Setup, 1: Laser source, 2: Periscope, 3: Sheet generator (cylindrical/spherical lenses).. . . . .	73
VI.4	Seeding Effect.. . . .	75
VI.5	Visualization sequence of a stoichiometric methane/air flame . . . . .	76
VI.6	Animation of a propagative stoichiometric methane/air flame at P=0.1 MPa, T=298 K, <i>In pdf version, please press play button in the control bar above.</i> . . . .	76
VI.7	Synchronization diagram. . . . .	77
VI.8	Representation of the fresh gas velocity profile near the flame front . . . . .	78
VI.9	Animation of flame speed extraction from tomographic images. <i>In pdf version, please press play button in the control bar above.</i> . . . . .	80
VI.10	Synthesis of the algorithm for fresh gas velocity profile determination. . . . .	83
VI.11	Animation of fresh gas velocity extraction from tomographic images using direct cylindrical correlation. <i>In pdf version, please press play button in the control bar above.</i> . . . . .	84
VI.12	Synthetic images and corresponding profiles. . . . .	85
VI.13	Comparison between standard PIV algorithm and accurate profile from this work. . . . .	86
VI.14	Comparison of $S_f$ , $u_n$ and $S_c$ for a methane/air flame . . . . .	87

VII.1	Equivalence ratio effect: $CH_4$ /air, $P = 0.1$ MPa, $T = 298$ K. . . . .	91
VII.2	Linear and non-linear methodologies: $CH_4$ /air, $P = 0.1$ MPa, $T = 298$ K. . . . .	91
VII.3	Linear and non-linear extrapolations: $CH_4$ /air, $\Phi=1$ , $P = 0.1$ MPa, $T = 298$ K. . . . .	92
VII.4	Linear and non-linear extrapolations: $CH_4$ /air, $\Phi= 1.2$ , $P = 0.1$ MPa, $T = 298$ K . . . . .	92
VII.5	Variation of fresh gas velocity, $u_g$ : $CH_4$ /air/mixture, $P = 0.1$ MPa, $T = 298$ K. . . . .	94
VII.6	Variation of laminar flame speed, $S_f$ : $CH_4$ /air mixture, $P = 0.1$ MPa, $T = 298$ K . . . . .	94
VII.7	Variation of flame speed: $S_f, u_g, u_n$ and $\frac{\rho_b}{\rho_u} S_f$ : $CH_4$ /air, $\Phi= 1$ , $P = 0.1$ MPa, $T = 298$ K . . . . .	95
VII.8	$u_n^0$ linearly or non-linearly extrapolated: $CH_4$ /air mixture, $\phi = 1$ , $P = 0.1$ MPa, $T = 298$ K. . . . .	95
VII.9	$u_n^0$ linearly or non-linearly extrapolated: $CH_4$ /air mixture, $\phi = 1.2$ , $P = 0.1$ MPa, $T = 298$ K. . . . .	96
VII.10	$u_n^0$ non-linearly extrapolated plotted against equivalence ratio: $CH_4$ /air mixture, $P = 0.1$ MPa, $T = 298$ K . . . . .	96
VII.11	$C_8H_{18}$ /air mixture, $P = 0.1$ MPa, $T = 373$ K. Comparison between density ratio and direct measurement methods . . . . .	98
VII.12	$C_2H_5OH$ /air mixture, $P = 0.1$ MPa. Comparison with literature . . . . .	99
VII.13	$C_2H_5OH$ /air mixture, $P = 0.1$ MPa. Comparison between the two methods . . . . .	99
VII.14	Temperature profiles for stoichiometric mixtures of methane and ethanol . . . . .	101
VII.15	Unstretched laminar burning velocity plotted against pressure: $C_2H_5OH$ /air mixture, $\phi = 1$ , $T = 373$ K . . . . .	101
VII.16	Temperature profiles for stoichiometric mixtures of Ethanol under pressure . . . . .	102
VII.17	Gas velocity: $v_{gaz}$ , burning velocity: $S_l$ , and flame propagation: $S_f$ . . . . .	103
VII.18	Comparison of 1D idealistic case and real flame. . . . .	104
VII.19	Estimation of the propagation speed to zero stretch for different isolevels considering a constant propagation velocity. $\kappa = \frac{2}{R} \frac{dR}{dt}$ . . . . .	105
VII.20	Estimation of $\epsilon$ parameter under several conditions of pressure for 1D ethanol flames. $\epsilon = 1 - \frac{T_2}{T_{ad}}$ . . . . .	106

VIII.1	Methane pressure and time derivative pressure signal . . . . .	111
VIII.2	$S_f$ , $S_c$ and pressure component . . . . .	112
VIII.3	$S_c$ lean condition . . . . .	113
VIII.4	Evolution of the consumption speed, $S_c$ , calculated using a diffusive filter and Polynomial Fits (third and fourth degree) for a $CH_4$ /air flame at $P = 0.1$ MPa, $T = 298$ K. . . . .	114
VIII.5	Evolution of the flame thickness with equivalence ratio for a $CH_4$ /air flame at $P = 0.1$ MPa, $T = 298$ K . . . . .	115
VIII.6	Evolution of the consumption speed, $S_c$ , and Markstein length, $L_c$ , estimated with the two Poinso's models V.4 and V.5 for a $CH_4$ /air flame at $P = 0.1$ MPa, $T = 298$ K. . . . .	115
VIII.7	Evolution of the consumption speed, $S_c$ , and Markstein length, $L_c$ , estimated with Poinso's model V.5 and Bradley's model V.6 for a $CH_4$ /air flame at $P = 0.1$ MPa, $T = 298$ K. . . . .	116
IX.1	Comparison of $S_f$ , $u_n$ and $S_c$ for methane/air flames. . . . .	120
IX.2	Comparison of $S_f$ , $S_d$ and $S_c$ for a methane/air flame . . . . .	120
IX.3	Comparison of $S_f$ , $u_n$ and $S_c$ for a stoichiometric methane/air flame . . . . .	121
IX.4	Comparison of $\frac{\rho_b}{\rho_u} S_f^0$ , $u_n^0$ , $S_c^0$ for propane and hydrogen/air flames and comparison with literature for $u_n$ . . . . .	122
IX.5	$\frac{\rho_b}{\rho_u} S_f^0$ , $u_n^0$ , $S_c^0$ for propane/air flames. . . . .	123
IX.6	Stretch effect on temperature and burned gases density . . . . .	124
IX.7	Impacts of stretch on the velocities estimation of $\frac{\rho_b}{\rho_u} S_f$ and $S_c$ from Bradley model . . . . .	125
IX.8	Methane, Propane and Hydrogen Markstein length, $L_b$ , mm compared with literature. . . . .	126
IX.9	Evolution of $L_b$ for the three gases against Lewis number . . . . .	127
IX.10	Evolution of the displacement speed $u_n$ with stretch for methane case . . . . .	128
IX.11	Evolution of $L_u$ for the three gases against Lewis number . . . . .	129

---

IX.12	Variation of Markstein numbers across the flame front . . . . .	129
IX.13	Evolution of $L_c$ for the three gases against Lewis number . . . . .	130
IX.14	Evolution of $L_c$ from Bradley computations compared to this study . . . . .	130
X.1	Laminar burning velocities of ethanol/air flames . . . . .	140
X.2	Laminar burning velocities of isooctane/air flames . . . . .	140
X.3	Laminar burning velocities of ethanol/isooctane/air mixtures . . . . .	142
X.4	Variations of Markstein length relative to fresh gas ( $L_u$ ) with equivalence ratio . .	142
X.5	Log-log scatter-plot of normalized laminar burning velocities $u_n(\phi, P)/u_n(\phi, P^0)$ .	144
X.6	$\beta$ parameter as a function of equivalence ratio . . . . .	145
X.7	Variations of stoichiometric Markstein length relative to fresh gas ( $L_u$ ) . . . . .	146
X.8	Burning velocity obtained by correlation compared with the experimental data . .	147
A.1	Sketch of thermodiffusive instabilities . . . . .	158
B.1	Normalized stretched flame speed as a function of normalized stretch rate. . . . .	162





# Nomenclature

## Greek Alphabet

$\beta = \frac{E}{RT_b^2}(T_b - T_u)$  Reduced activation energy derived from the *Zeldovich Number*

$\delta_f$  Flame thickness based on thermal properties

$\delta_l$  Universal flame thickness

$\delta_p$  Flame thickness based on the thermo-diffusive zone

$\delta_r$  Reaction zone flame thickness

$\dot{\omega}_k$  species  $k$  reaction rate

$\dot{\zeta}$  Chemical reaction rate from Arrhenius law

$\gamma = \frac{T_b - T_u}{T_b}$  Expansion factor

$\kappa = \frac{1}{A} \frac{dA}{dt}$  Stretch factor

$\lambda$  Thermal conductivity

$\nu$  Stoichiometric coefficient

$\psi = Y/Y_u \in [0; 1]$  Reduced mass fraction

$\rho$  Density

$\theta = \frac{T - T_u}{T_b - T_u}$  Reduced temperature

## Latin Alphabet

$\dot{m}$	Mass flux
$\mathcal{C} = \nabla \cdot \vec{n}$	Curvature
$\mathcal{D}_k$	Diffusion coefficient of species $k$
$\mathcal{D}_{th}$	Thermal diffusivity
$\mathcal{H}_s$	Strain rate
$\mathcal{M}_k$	Molar mass of species $k$
$\vec{q}$	Heat flux density vector
$A$	Infinitesimal element of the surface
$C_p$	Constant pressure specific heat
$F, O, P$	Fuel, oxidizer and product
$h_k^0$	Formation enthalpies of species $k$
$Le = \alpha/D$	Lewis number
$P$	Pressure
$Q$	Molar heat release
$S_c$	Consumption speed
$S_d$	Displacement speed
$S_f$	Absolute flame speed
$S_l$	Laminar burning velocity
$T$	Temperature
$X_k$	Molar fraction of species $k$
$Y_k$	Mass fraction of species $k$

### Subscript and Superscript

- Related to mean spatial value
- 0 Related to unstretched condition
- ad Related to the adiabatic condition
- b Related to the burned gas
- c Related to the critical condition
- eq Related to equilibrium state
- u Related to the unburned gas

# Chapter I

## Introduction

### I.1 Background

Ever since prehistoric times, combustion has always been the major energy production process. The high level of development reached over the last century is mostly due to impressive technological improvements that result from massive utilization, transformation and control of the main energy resource: fossil oil. However, fossil energy combustion leads to high levels of pollutant emissions, such as carbon monoxide, greenhouse gases and particles. Current ecological and political contexts encourage scientists and engineers to improve combustion systems in order to limit consumption and curb toxic emissions. This objective cannot be reached nowadays only by empirical methods that would consist in improving macro-structure combustion installations. Such methods would only allow us to recover a few percent global efficiency, but at a very high financial and time cost. Moreover, because of the depletion of fossil fuels, new fuels, such as bio-blended fuels, appear. Bio-fuels can be produced from the direct transformation of traditional food crops (sugar, starch or vegetable oil) and are then called “first-generation bio-fuels”. However, the global impact of such transformation is non-negligible and “second generation bio-fuels”, obtained from plant residues, offer a more sustainable solution. They are generally used in ground-based transportation and countries like Brazil use pure ethanol since the 70’s. In France, ethanol in gasoline appears in ratios from 15% for conventional SI engines to 85% for adapted engines (Flex-fuels). However, we can report that their energy density is

lower than in conventional gasoline (partially oxidized) but they still appear as representative components of alternative fuels. When used in internal combustion engines, ethanol leads to an increase in the octane number of the blended fuel, which causes the compression ratio and engine performances to increase and prevents the engines from knocking. The effect of ethanol on pollutant emissions is varying and depends on the fuel blend: in the case of ethanol-gasoline fuel blends, engine tests indicate that carbon monoxide (CO) and unburned hydrocarbon (HC) emissions decrease as a result of the leaning effect induced by the ethanol. However, the results are different for ethanol-diesel fuel blends: CO and HC emissions increase and depend on the ethanol blending ratio and engine operating conditions (injection timing, engine load). In diesel engines, ethanol blending also reduces the quantity of particulate matter [1]. Pollutant emissions are directly related to laminar flame properties. Hence, it is necessary to acquire fundamental knowledge of the properties of these fuels. When we talk about combustion properties, one of the key parameters is laminar burning velocity.

## I.2 Laminar Burning Velocity

Idealistically, laminar burning velocity is defined in its one-dimensional configuration. Laminar burning velocity corresponds to the velocity at which the fresh premixed gases make a planar flame steady. It is generally referred to as  $S_l^0$ . This flame is supposed to be one-dimensional, unstretched and adiabatic so that the burned gases achieve equilibrium. This quantity is universal and only depends on the initial thermodynamical conditions (pressure, temperature) and the mixture considered.

Laminar burning velocity plays an important role in studying the combustion process by containing fundamental information regarding the reactivity, diffusivity, and exothermicity of a combustible mixture. Moreover, evaluating burning velocity is also important for the following points:

- Validation of chemical kinetic mechanisms for conventional and alternative fuels.

The chemical kinetics of a flame is achieved by solving balance equations of one-dimensional laminar flame numerically. However, the chemical kinetic data (transport coefficients) in

such models are not always sufficiently well known to be used with confidence, even less in the case of diluted or heavy fuels. Laminar burning velocity is therefore commonly used to validate the chemical kinetic schemes, for it allows the extension of the validity range of mechanisms at higher pressures or higher ranges of equivalence ratios.

In view of the application in bio-fuels, a number of detailed kinetic reaction mechanisms have been developed recently for either pure ethanol [2, 3, 4] or pure isooctane (a gasoline surrogate) [5, 6] or blended fuel [7] and partially validated for a range of experimental data, including flame structure and laminar burning velocity. If we look at Fig. I.1, we can observe that when ethanol is considered, two kinetic schemes, Marinov's [2] and Konnov's [3], do not lead to the same value, whereas thermodynamical conditions are standard ones, *i.e.* pressure  $P=0.1$  MPa and temperature  $T=300$  K. Since estimating laminar burning velocity at standard conditions is already a complex process, the validity of such schemes for thermodynamical conditions at high pressure and temperature is questionable. Furthermore, it is important to include the action of pressure and temperature on the laminar burning velocity of such mixtures for thermodynamical conditions similar to those encountered in SI engines. New experimental data will definitely be needed to validate these mechanisms.

- Laminar burning velocity is an important parameter in turbulent combustion modeling. This is well known for the flame surface density models in RANS where the mean reaction rate,  $\bar{\dot{\omega}}$ , is described as the product of the flame surface density  $\Sigma$  (*i.e.* the available flame surface area per unit volume) by the local consumption rate per unit of flame area [8] (Eq. I.1). This latter is the spatially-averaged consumption speed  $S_c$ , and is linked to the unstretched laminar flame speed by a stretch factor,  $I_0$  [9]. This stretch factor is very well represented by the Markstein-type correlation [10, 11] (Eq. I.2).

$$\bar{\dot{\omega}} = \rho_0 S_c \Sigma \quad (\text{I.1}) \quad I_0 = \frac{S_c}{S_l^0} = 1 - L_c \frac{\kappa}{S_l^0} \quad (\text{I.2})$$

where  $\rho_0$  is the fresh gases density,  $L_c$  is the Markstein length associated to the consumption speed,  $\kappa$  is the flame stretch. For mixtures with Lewis numbers close to unity, the factor  $I_0$

remains around unity. In first order approximations, strain effects are sometimes neglected in some models which simply set consumption speed as equal to the unstretched laminar flame speed. Notwithstanding, for mixtures with high/low values of Lewis numbers, this approximation is not valid. A flamelet library that tabulates the laminar consumption rate per unit flame surface for each range of stretch values must therefore be used.

In tabulated chemistry LES approaches, reaction and unresolved transport terms are tabulated according to the filtered progress variable, mixture fraction and filter size [12]. The turbulence/combustion interaction is then modeled through a wrinkling factor. However, recent work on forced ignition simulation [13] showed that strain rate effects need to be included in the modeling of the filtered burning rate to accurately predict the first stages of kernel propagation, where it is submitted to a high stretch level. This could also be done by measuring the Markstein length, which directly represents the flame's response to stretch.

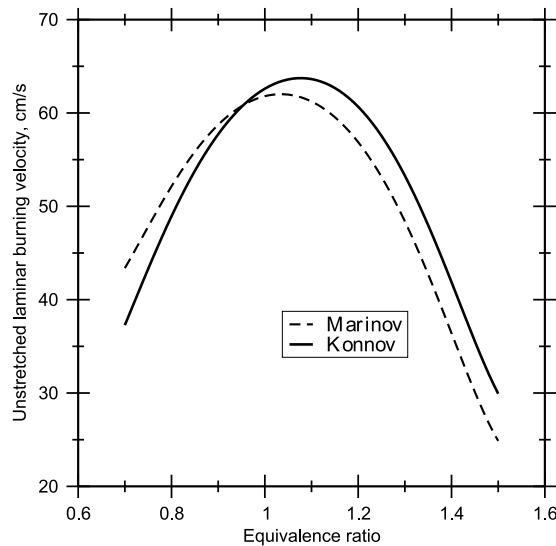


Figure I.1: Marinov [2] and Konnov [3] models for an ethanol/air flame.  $P=0.1$  MPa,  $T=300$  K

This shows the importance of laminar burning velocity, stretched/unstretched, and supports the idea that experimentalists have to provide measurements of this fundamental parameter as accurately as possible. Moreover, laminar burning velocity studies are still as relevant today as they were 50 or 100 years ago [14, 15] because of the increase in accurate modeling demand.



## I.3 Scientific Background

### I.3.1 Experimental Configuration

Experimentally, the 1D flame cannot be achieved due to heat losses (boundaries) and non-flat inlet profile of fresh gases. In experimental cases, the flame is submitted to stretch (non-homogeneous flow field), loss (at burner's level) or the two combined. Laminar burning velocity can be determined via several experimental approaches using different flame configurations such as Bunsen flames, burner flat flames stabilized by heat flux method, counterflow or stagnation flames, spherical expanding flames processed in closed vessels. These experimental flames setups are presented in Fig. I.2. If many experimental ways exist for velocity measurement, it is due to the various hypotheses and difficulties involved in those configurations (low cost solutions or hard engineering, stationary/non-stationary flames, planar/stretch free, stability, oscillations...).

In 1972, Andrews and Bradley [17] carried out a critical review of the various experimental

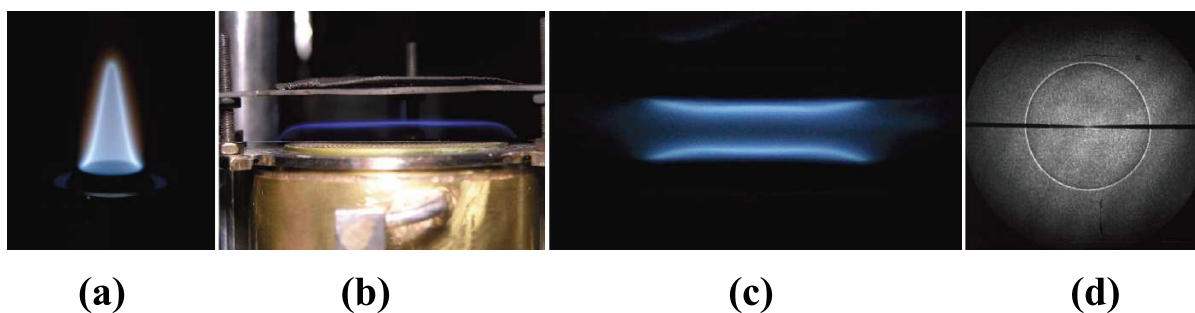


Figure I.2: Laminar flames configurations: (a) Bunsen flames, (b) burner flat flames stabilized using the heat flux method, (c) counterflow flames, spherical expanding flames using closed vessels. From [16]

techniques for the measurement of burning velocity. They found that, comparing all the techniques, a wide scatter on the maximum velocity of methane was observed. They recommended that maximum burning velocity for a methane air flame at 298 K and 1 atm should be  $45 \text{ cm/s} \pm 2 \text{ cm/s}$ . To some extent, they implied that observed discrepancies were due to the difference

in experimental methods between stationary and non-stationary configurations and proposed correction factors depending on the configuration used. Updated by Kelley and Law [18], the evolution of the maximum velocity for methane over the years now seems to tend to  $36 \text{ cm/s} \pm 2 \text{ cm/s}$  (Fig. I.3) with much less scatter range. This is probably due to the improvement in experimental configuration but also to the fact that, before the 80s, stretch effect ( $\kappa$ , linear or non-linear dependence) was not taken into account (Wu and Law [19]). Phenomenological considerations establish a link between stretched velocities and unstretched ones and the stretch factor  $\kappa$  appears to be the scalar that controls the burning velocity. It is now admitted that non-linear relation [20] must be used to zero stretch extrapolation and the so called Markstein length raises the burning velocity behavior toward stretch.

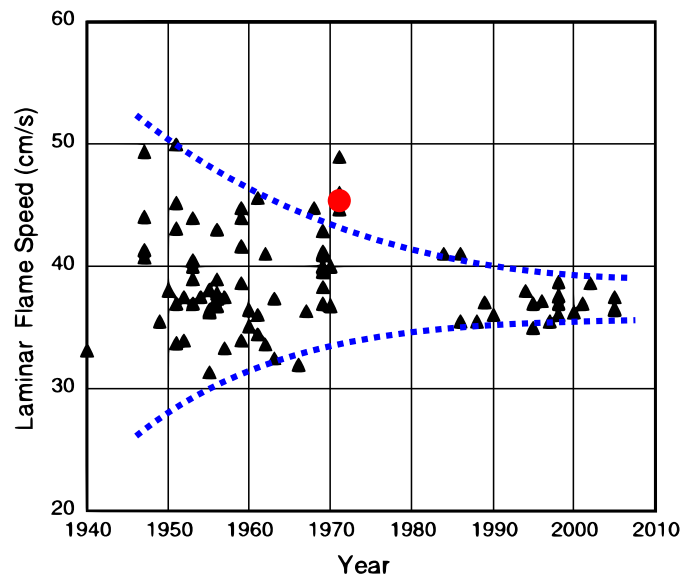


Figure I.3: Methane maximum velocity over the years showing the scatter discrepancy progression to be less than  $\pm 2 \text{ cm/s}$ ,  $P=0.1$ , ambient temperature, from Law *et al.* [18]. Red point: Bradley's recommendation 1972 [17]

### I.3.2 The spherical expanding flame configuration

In this study, we focus on the description of the spherical expanding flame technique at constant pressure. This configuration makes it possible to reach thermodynamic conditions before

ignition, at elevated pressures and temperatures, that are very difficult to reach using steady-state methods (flat flame burner, rim-stabilized conical flame, counterflow), which operational ranges are limited to a few atmospheres due to flame stability problems. In addition, the effect of stretch can be well integrated because it can be extracted from the direct topology of the spherical flame. As we know, this configuration consists in centrally igniting (spark electrodes) an homogeneous combustible mixture in a closed vessel at  $P = P_0$  and  $T = T_0$  where  $P_0$  and  $T_0$  represent the initial condition. A propagating expanding flame develops from the ignition point to the fresh gases and can be recorded by tomographic (Fig. I.4) optical diagnostic for example.

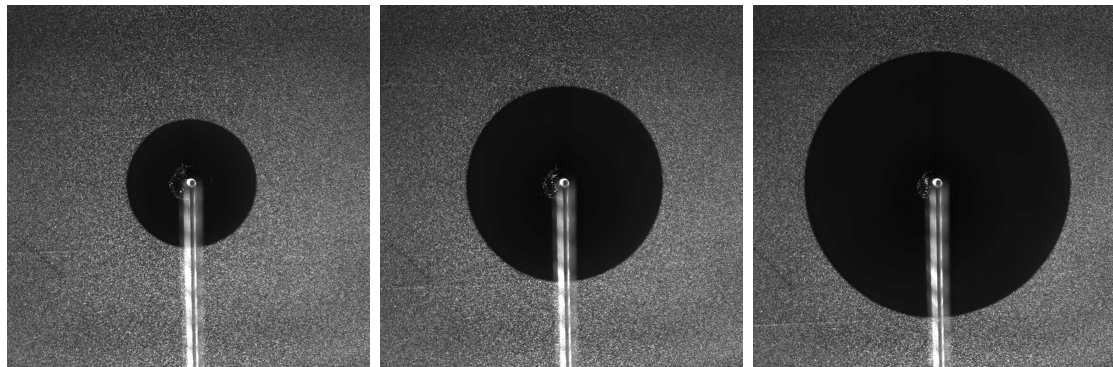


Figure I.4: Tomographic visualization of a propagation sequence of a stoichiometric methane/air flame at  $P=0.1$  MPa,  $T=298$  K

Depending on the considered reference frame, it is possible to extract various data from this spherical expanding flame.

- Laboratory reference frame

At first sight, looking at the flame propagation, one can easily measure the velocity at which the flame propagates via, for example, the time evolution of flame radius. This velocity is called *flame propagation speed*, or *absolute flame speed* and is linked to the velocity at which the burned gases expand due to the thermal jump across the flame. This technique is the simplest and the most widely used technique in literature. In fact, the flame front extraction is very simple.

- Flame reference frame

Figure I.5: Animation of a propagative stoichiometric methane/air flame at  $P=0.1$  MPa,  $T=298$  K, *In pdf version, please press play button in the control bar above.*

When the observer is positioned on the flame, it is possible to evaluate the velocity at which fresh gases pass through it. It corresponds to a relative speed also called *displacement speed* if we consider the fresh gases isothermal. Displacement speed is obtained by subtracting propagation speed (defined above) from the velocity of fresh gases just ahead of the flame front at the isothermal of fresh gases. However, this displacement speed can be evaluated at any isothermal and called indifferently  $S_d$ .

For their review, Andrews and Bradley [17] used hot wire anemometer to measure fresh gas velocity. Nonetheless, measuring fresh gas velocity has been long neglected because of the inherent difficulty in experimental technique and post-processing. With the improvement of technology and computer-aided post-processing algorithms, it is nowadays possible, though not trivial, to measure fresh gas velocity in the first millimeters ahead of the flame front with high accuracy ([21]).

- Chemical scale

Once again, we change the reference frame and we are now positioned at a chemical scale. It is possible to express the velocity at which the reactants are consumed (or products appear), that is called *consumption speed*. Consumption speed is directly linked to the reaction rate and can be obtained by numerical simulations where the reaction rate is known at each point of the domain. However, measuring this integral quantity in experimental setups is a complex process, for it implies to know the evolution of the density through the flame.

In a one-dimensional flame (adiabatic, premixed, planar, stretch free), the quantities defined above are directly linked to the laminar burning velocity and give the true estimation of  $S_l^0$ . In real cases, however, velocity may vary due to the impact of stretch on the flame.

## I.4 Purpose of this study

Laminar burning velocity is a crucial parameter in flame properties, on which it is interesting to deliver accurate data. In order to succeed, the spherical flame configuration is chosen. How-

ever, three velocities are identified and can give an estimation of the laminar burning velocity depending on the chosen reference frame. The objectives and questions of this research are:

- Do these formulations converge to a unique and identical value when stretch is null? These velocities represent the same phenomenon – burning velocity – seen from different angles. When extrapolated to zero stretch (planar flame), these velocities might be identical.
- What do we clearly measure? This study aims to identify the sources of uncertainty mainly induced by hypotheses and assumptions involved in the formulation of the burning velocity extracted from the three aforementioned formulations.
- How can these three velocities be accurately determined experimentally? It implies the development of a facility and specific post-processing tools that do not exist. These new tools are essential for the determination of fresh gas velocity .
- Which solution for high-pressure database of ethanol and isooctane?

## I.5 Structure of the dissertation

The dissertation is composed of three parts. In a first step, before getting into the experimental investigation, the theoretical background is exposed. It is composed of three chapters and organized as follows:

- Chapter II: *One-dimensional flames*. A thorough understanding of the idealistic one-dimensional flame and the governing equations is presented.
- Chapter III: *From planar to stretched flames*. Because idealistic 1D flame is not accessible experimentally, stretch definition and its impact on burning velocities is pointed out.
- Chapter IV: *On the determination of the consumption speed*. In this chapter, the consumption speed formulation is explored in order to identify the hypotheses and limitations involved. Two cases are differentiated: infinitely thin flame and finite flame thickness.

- The theoretical part ends with Chapter V that summarizes all the definitions that will be used latter.

The second part exposes the experimental setups and results. The following guideline is proposed:

- Chapter VI: *Experimental Setup*. The experimental setup is presented and the main point concerns the description of the kinematic-based technique, where the fresh gas velocity profile ahead of the flame front is investigated.
- Chapter VII: *Measurement of the Unstretched Laminar Burning Velocity from the Flame and Displacement Speeds*. Laminar burning velocities are achieved from methane, ethanol and isooctane flames. In this chapter, displacement speed and propagation speed formulation are compared in order to identify and explain possible discrepancies. *The majority of the material presented in this chapter has been previously published under [21]*
- Chapter VIII: *On the experimental determination of consumption speed*. The third velocity formulation called *consumption speed* is experimentally investigated.
- Chapter IX: *Flame response to stretch*. This chapter studies the flame response to stretch by comparing the estimation of the unstretched velocities from the three formulations and their associated Markstein lengths. Three fuels are investigated, each of which presents a distinct thermo-chemical parameters, namely the Lewis number ( $Le$ ).
- Chapter X: *Ethanol-Isooctane Blends*. An analysis of the influence of pressure on laminar burning velocity / Markstein length of pure isooctane, pure ethanol, and blended fuels by using the displacement speed formulation is developed in this chapter. *The majority of the material presented in this chapter has been previously published under [22]*

Finally, in a third part, the results of the present work are summarized in Chapter XI and suggestions for further research are presented.





## **Part I**

# **Theoretical background**



## Chapter II

# One-dimensional flame

In this chapter, several concepts are developed in order to define the flame properties in the simplified case of one-dimensional representation. This flame's concept is the first step towards answering the remaining question: How a flame can be modeled ? This chapter provides information on flame structure and the governing equations, as well as a clearer picture of what *laminar burning velocity* is. The main idea is to provide theoretical background to extrapolate the 1D concept to real flames.

### II.1 Laminar Premixed Flame: Structure

Laminar premixed flame structure is governed by aerodynamics through the following elements: convection, transport – heat and mass diffusion – and chemistry. Laminar flame being a very complex phenomenon, many studies have reduced the problem for practical combustion analysis. An ideal conception and representation is the model of a one-dimensional steady flame which is nowadays currently used. The flame is represented as an interface (infinitely thin or not) and separates the fresh gas or unburned gas (reactant side) – subscript  $u$  –, at the temperature  $T = T_u$  from burned gases (product side) – subscript  $b$  – at  $T = T_b$ .  $T_b$  is considered to be equal to the adiabatic flame temperature  $T_{ad}$ . The species mass fraction goes from the initial state  $Y = Y_u$  to  $Y = 0$  in burned gas. Associated with these definitions, laminar flame speed is generally considered as the velocity at which the flame front moves toward the fresh gases,

or, in the case of a steady flame, as the velocity at which the inlet gases make the flame sheet steady in the laboratory frame:  $S_l^0$ . Superscript <sup>0</sup> is for planar flames. We will see later that the exact definition of laminar flame speed is linked to the burning rate and corresponds to the velocity at which fresh gases are consumed by the flame.

In terms of flame structure, we can relate to Law and Sung's work [23]. They described three levels of laminar premixed flame complexity. For all these models, a kinematic analysis of the representation, as shown in Fig. II.1, allows us to determine the flame speed relation:  $S_l^0 = \dot{m}/\rho_u$  where  $\dot{m}$  and  $\rho_u$  are respectively the surface mass flux and the unburned gas density.

- The simplest model (Fig. II.1): The flame is considered as an interface (discontinuity) separating two thermodynamic states of unburned and burned gases considered at the equilibrium. Transport and chemistry are not taken into account.

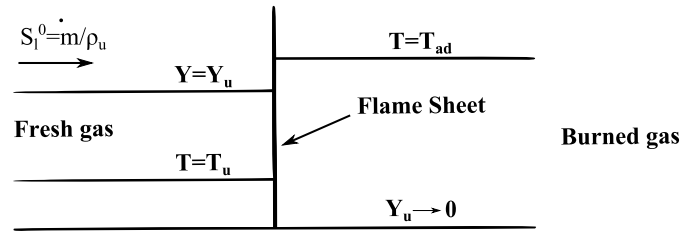


Figure II.1: Schematic structure of a one-dimensional, planar, steady flame. Simplest model.

- Transport-dominated model (Fig. II.2): The mixture approaches the flame and is gradually heated by heat conductivity produced in the heat-release region. The reaction is activated only when temperature is close to burned gas temperature (high-activation energy). The reaction zone is still considered an interface.
- Full description model (Fig. II.3): A flame's structure is divided into a thin reaction zone and a convective preheat-diffusing zone of respective thicknesses  $\delta_r$  and  $\delta_p$ . The reaction zone embeds the reaction rate as a peak function shape. The preheat-zone conserves its convection and heat/mass diffusion role. It can be assumed that  $\delta_r \ll \delta_p$  and  $\delta_l$  represents the total flame thickness. Expression of the thermal diffusion and reaction zones can be found in literature. It is important to note that thickness estimation is not a simple

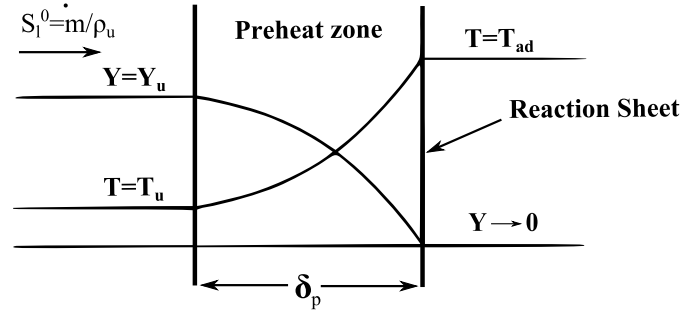


Figure II.2: Schematic structure of a one dimensional, planar, steady flame. Transport-dominated model.

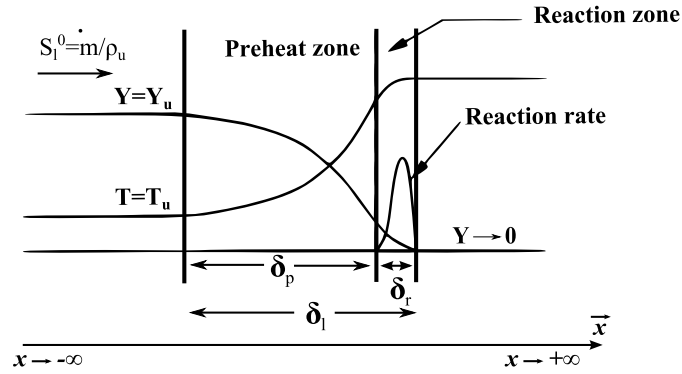


Figure II.3: Schematic structure of a one-dimensional, planar, steady flame. Full description model.

process. The diffusing thickness can be expressed as:

$$\delta_p = \frac{\lambda_u}{\rho_u C_p} \frac{1}{S_f^0} = \frac{\mathcal{D}}{S_f^0} \quad (\text{II.1})$$

where  $\mathcal{D}$  is the thermal diffusivity,  $\lambda$  is the thermal conductivity and  $C_p$  is the constant pressure heat capacity.

This expression of flame thickness results from the equilibrium between mass and heat diffusion. With typical values of  $\lambda$ ,  $C_p$ ,  $\rho$ , and assuming a flame speed of about 0.50 cm/s, we achieve an estimation of  $\delta$  of about  $10^{-2}$  cm. As described in [24], values obtained via the latter are too small compared to experimental flame thickness. A very useful flame thickness estimation can be obtained from thermal properties:

$$\delta_f = \frac{T_{ad} - T_u}{\max \left| \frac{\partial T}{\partial x} \right|} \quad (\text{II.2})$$

It can be noted that to estimate this thickness, the temperature gradient must be determined based on the temperature profile. A numerical simulation is needed and grid point number must be large enough to accurately define the reaction zone. A better approximation of the flame thickness, based on thermodynamic properties, comes from Blint's correlation[25]. Using assumptions that are described in [26] it is possible estimate a flame thickness prior to any calculation:  $\delta_l = 2\delta_p(T_{ad}/T_u)$ . This flame thickness estimation is in agreement with classical magnitude order  $\approx 0.5 \text{ mm}$ .

These flame representations make it possible to access different macroscopic flame information such as flame thickness and velocity. In order to better understand the inner flame structure and reactivity, it is necessary to explore the governing equations in a one-dimension direction.

## II.2 Laminar Premixed Flames: 1D Equations

The one-dimensional configuration provides substantial information on the flame characteristics – velocity, temperature, species – or on the overall reactivity of the flame by deriving the governing equations of continuity, momentum, species and energy. The basic reaction can be written as Eq. II.3.



where  $\nu_i$  are the stoichiometric coefficients of respectively  $F$  : *Fuel*,  $O$  : *Oxidizer* and  $P$  : *Products*.  $Q$  is the total molar heat release. Reactive Navier-Stokes conservation equations can be simplified when considering laminar one-dimensional premixed flames. As presented in [26], only the conservation equations of mass, species and energy are needed.

- Stationary flame: derivative in time are removed.
- Planar unstretched flame: 1D.
- Isobaric combustion.
- Viscous terms neglected.
- Molar mass constant through the domain so that a Fick's Law is recovered.

- Fourier's law for the heat flux density vector.

- Low Mach

1D equations yield:

- Mass conservation:

$$\rho u = \rho_u S_l^0 \quad (\text{II.4})$$

- Species  $k$  transport:

$$\frac{\partial}{\partial x}(\rho u Y_k) = \frac{\partial}{\partial x}(\rho \mathcal{D}_k \frac{\partial Y_k}{\partial x}) + \dot{\omega}_k \quad (\text{II.5})$$

where:  $\dot{\omega}_k$  is the species  $k$  reaction rate,  $\mathcal{D}_k$  is the diffusion coefficient of species  $k$ .

- Energy conservation:

$$\rho C_p u \frac{\partial T}{\partial x} = \frac{\partial}{\partial x}(\lambda \frac{\partial T}{\partial x}) + Q \dot{\zeta} \quad (\text{II.6})$$

$\dot{\zeta}$  is the chemical reaction rate from Arrhenius law and  $\dot{\omega}_k = -\nu_k \mathcal{M}_k \dot{\zeta}$ .  $Q = -\sum_{k=1}^n (a_k \mathcal{M}_k h_k^0)$  with  $a_k = \nu_k^{productside} - \nu_k^{reactantside}$  and  $h_k^0$  is the formation enthalpies of species  $k$ .

Before solving these equations and obtaining the different profiles, final values of species or temperature can be determined by a pure combination of these equations. The unknown reaction rate,  $\dot{\zeta}$ , vanishes from the equations.

- **Adiabatic temperature**

Starting from the species equation II.5 and writing it for fuel species ( $f$ ), combining with energy equation II.6 lead to:

$$\frac{d}{dx} \left[ \rho_u S_l^0 \left( C_p T + \frac{Q Y_f}{\nu_f \mathcal{M}_f} \right) \right] - \frac{d}{dx} \left[ \lambda \frac{dT}{dx} + \frac{\rho \mathcal{D}_f Q}{\nu_f \mathcal{M}_f} \frac{dY_f}{dx} \right] = 0 \quad (\text{II.7})$$

Integrating the equation above from  $-\infty$  to  $+\infty$  and applying boundary conditions, we found, for a lean mixture (depleted fuel:  $\phi < 0$ , where  $\phi$  is the equivalence ratio):

$$\rho_u S_l^0 \left[ C_p T + \frac{Q Y_f}{\nu_f \mathcal{M}_f} \right]_{-\infty}^{+\infty} = 0 \quad (\text{II.8})$$

A similar expression for the rich side, that corresponds to a complete depletion of the oxidizer ( $\phi > 0$ ), can be written and a system of equations can be expressed to determine  $T_{ad}$ , the adiabatic flame temperature:

$$T_{ad} = \begin{cases} T_u + \frac{(QC_p)Y_f^u}{\nu_f \mathcal{M}_f} & \phi < 1 \\ T_u + \frac{(QC_p)Y_o^u}{\nu_f \mathcal{M}_o} & \phi > 1 \end{cases} \quad (\text{II.9})$$

- **Species values**

Combining and integrating the two expressions of species for oxidizer and fuel, using the same methodology as for temperature, species final values can be determined as:

$$\begin{aligned} Y_f = 0, \quad Y_o = Y_o^u(1 - \phi) & \quad \text{for } \phi < 1 \\ Y_o = 0, \quad Y_f = Y_f^u(1 - \frac{1}{\phi}) & \quad \text{for } \phi > 1 \end{aligned} \quad (\text{II.10})$$

The above section provides estimation of laminar flame thickness, temperature and species value for a one-step chemistry as expressed in Eq. II.3. The temperature and species values on the burned side also depend on thermodynamic; the chemistry is not needed. Furthermore, determining the profiles of temperature and species implies solving the set of 1D flame equations. Such a procedure is problematic, for the reaction rate is unknown. The problem is mathematically ill-posed and a model is needed for reaction rate closure. For reaction rates, most of the time, an Arrhenius law is used. It is also important to note that we have introduced Fick and Fourier laws, for respectively the mass and heat diffusion. Other models could have been used, such as velocity diffusivity models or multiple species diffusion. It is worth noting that in a complex detailed chemistry system, many intermediate species and radicals are produced. Each one needs to be solved by integrating the set of equations. Every intermediate species has a different response within the flame brush. This leads to appreciate anew the definition of flame thickness depending on the studied species. Solving the 1D set of equations is rather problematic and many issues occur, such as the well known *cold boundary* issue. However, analytical solution for laminar flame speed can be achieved through thermodynamical consideration on flame structure. An example of laminar flame speed is given below.

- **Analytical solution for flame speed evaluation**

In this section, an analytical approach is used to give an explicit flame speed expres-



sion. This analytical/asymptotic formulation was first described by Zeldovich, Frank-Kamenetskii and Von Karman (ZFK) extended to high activation energy. It is based on a thermodynamical derivation of the 1D equations. This approach leads to an expression of the laminar flame speed coupling the flame equations along  $\vec{x}$  under several assumptions:

- $\rho = \rho(T)$  quasi isobaric
- Stationary
- One of the reactants is limiting the combustion, it can be either  $Y_f$  or  $Y_0$ . In this case, its mass fraction varies from  $Y_u$  ( $u$  for unburned) to zero.
- $\dot{\zeta} = \frac{1}{\tau_r} \rho_b B(T) Y^\eta e^{-E/RT}$  where  $\tau_r$  is a typical reaction time,  $B(T)$  is the pre-exponential function of Arrhenius's law and  $\eta$  is the order of the reaction. In the asymptotic case of high activation energy,  $B(T)$  can be considered a constant.

Different reduced variables are introduced:

Reduced Mass fraction:  $\psi = Y/Y_u \in [0; 1]$

Reduced activation energy:  $\beta = \frac{E}{RT_b^2} (T_b - T_u)$

Expansion factor:  $\gamma = \frac{T_b - T_u}{T_b}$

Reduced temperature:  $\theta = \frac{T - T_u}{T_b - T_u}$

It leads to rewrite  $\dot{\zeta}$  as  $\dot{\zeta} = \frac{1}{\tau_r} \rho_b B Y_u^n \psi^n e^{-\frac{\beta(1-\theta)}{1+\gamma(\theta-1)}}$ .

An analysis of the function  $f(\theta) = e^{-\frac{\beta(1-\theta)}{1+\gamma(\theta-1)}}$  for high-activation energy shows that the denominator term  $\gamma(\theta - 1) + 1$  can be neglected. In fact, it is non-null for  $\theta$  close to zero but in this case,  $f(\theta) = 0$ . For the  $\theta$  upper boundary,  $\gamma(\theta - 1) + 1$  is null. The exponential function is dominated by  $\beta$ . Finally  $\zeta$  is given by Eq. II.11:

$$\dot{\zeta} = \frac{1}{\tau_r} \rho_b B Y_u^n \psi^n e^{-\beta(1-\theta)} \quad (\text{II.11})$$

Eq. II.4, II.5 and II.6 can be rewritten with this new variables and give:

$$\rho_u S_l^0 = \rho_u = \rho_b u_b = \dot{m} \quad (\text{II.12})$$

$$\begin{aligned} \dot{m} \frac{d\psi}{dt} &= \rho \mathcal{D} \frac{d^2\psi}{dx^2} - \dot{\xi} \\ \dot{m} \frac{d\theta}{dt} &= \frac{\lambda}{C_p} \frac{d^2\theta}{dx^2} + \dot{\xi} \end{aligned} \quad (\text{II.13})$$

where  $\dot{\xi} = \dot{\zeta} \frac{\nu_u \mathcal{M}}{Y_u}$

This result gives a system of equations where  $\dot{m}$ ,  $\theta$  and  $\psi$  are the unknowns. At this point, the solution can be found by analyzing two zones separately. The transport-dominated zone, *i.e.* diffusing zone, corresponds to negative values of the flame position and the reaction zone takes place in positive values.

### 1. Solution in the thermo-diffusing zone (negative x values)

The chemical term can be neglected. This, taking into account respective limit conditions, yields:

$$\begin{aligned} \dot{m} \frac{d\psi}{dt} &= \rho \mathcal{D} \frac{d^2\psi}{dx^2} & x \rightarrow -\infty ; \psi \rightarrow 1 \\ & & x \rightarrow O^- ; \psi \rightarrow 0 \end{aligned} \quad (\text{II.14})$$

$$\begin{aligned} \dot{m} \frac{d\theta}{dt} &= \frac{\lambda}{C_p} \frac{d^2\theta}{dx^2} & x \rightarrow -\infty ; \theta \rightarrow 1 \\ & & x \rightarrow O^- ; \theta \rightarrow 0 \end{aligned} \quad (\text{II.15})$$

For negative values of x, the solutions of such equations are:

$$\psi = 1 - e^{-\frac{\dot{m}}{\rho \mathcal{D} \lambda} x} \quad (\text{II.16})$$

$$\theta = e^{-\frac{\dot{m} C_p}{\lambda} x} \quad (\text{II.17})$$

### 2. Solution in the reaction zone (positive x values)

Eq. II.13 can be written combining the two conservation (species and energy) equa-

tions and the problem is reduced to:

$$\begin{aligned}\frac{d}{dx^2} \left[ \rho \mathcal{D} \psi + \frac{\lambda}{C_p} \theta \right] &= 0 \\ \frac{d}{dx^2} [\psi + Le\theta] &= 0 \\ \psi + Le\theta &= ax + b\end{aligned}\tag{II.18}$$

where  $Le = \frac{\lambda}{\rho C_p D} = \frac{\mathcal{D}}{D}$  is the Lewis number and  $\mathcal{D}$  is the thermal diffusivity.  $a$  and  $b$  are the unknown to be defined. Considering the limit conditions and adiabatic assumption at  $x = 0 - \frac{\partial \theta}{\partial x} = 0 -$ , the solution comes down to one single equation, for energy and species are linked by  $\psi = Le(1 - \theta)$ .

### 3. Asymptotic connection between the two zones

Finally,  $\dot{m}$  is found by combining the solutions of  $\theta$  (or  $\psi$ ) between the two zones:

$$\dot{m} = \rho_u S_l^0 = \sqrt{2 \frac{\lambda}{C_p} \frac{n!}{\beta^{n+1}} \frac{1}{\tau_r} \rho_b B L e^n}\tag{II.19}$$

where  $\tau_r = \tau_r \frac{\nu_u \mathcal{M}}{Y_u}$ .

$S_l^0$  is unique for fresh gases.

### General remarks

This relation is valid for the lean or rich side as mentioned in the starter assumptions.

Because of the high energy activation, reaction occurs when temperature is close to  $T_{ad}$ , that is located in the reaction zone.

The strong dependence of Arrhenius law regarding temperature indicates that the adiabatic flame temperature strongly affects laminar flame speed.

$\lambda$  needs to be evaluated at burned gas temperature and flame speed is directly affected by its value.

The flame speed increases with  $T_u$  and flame thickness decreases (see expression II.1).

- **Computing 1D flame**

As said above, the resolution of 1D flame is necessary to achieve species, temperature and

velocity profiles along the flame brush. Numerous details on numerical methods can be found in Poinso and Veynante [26]. We will now expose the main idea and assumptions necessary to achieve successful 1D simulations. We assume a low Mach number that implies deflagration phenomenon, the pressure field is uniform and viscous effects are neglected. Because modeling heat losses is difficult, the flame is considered as an adiabatic system. In steady cases, the time rate of change of those quantities vanishes and the equations of mass, energy and species are combined with the state equation  $p = \rho r$ , where  $r = R/\mathcal{M}$ .  $R$  is the perfect gas constant. It (Eq. : II.4, II.5, II.6 and state equation) represents a closed system ( $n+3$ , where  $n$  is the number of species involved in the reaction scheme). The system can be cast into a specific form, classically expressed as:

$$B(u) \frac{d\vec{u}}{dx} = \vec{f}(\vec{u}) \quad (\text{II.20})$$

where  $\vec{u}$  is the unknown vector:  $\vec{u} = (T, S_l^0, Y_1, \dots, Y_n)$

We present below the results of a 1D steady flame obtained with Cosilab software in the case of a methane/air mixture at 0.1 MPa and 300 K initial conditions. GRI-Mech 3.0 [27] reaction mechanism has been used associated with the thermodynamical and transport property tables. The mechanism includes 325 reactions and 53 species. The profiles of temperature, heat-release rate, velocity and OH mole fraction are reported below (Fig. II.4). By this computation, we obtain an inlet fresh gas velocity of about 37.5 cm/s for a stoichiometric flame. Furthermore, the temperature profile makes it possible to determine the flame's thickness by the thermal definition as expressed in Eq. II.2. This gives  $\delta_f \approx 0.45 \text{ mm}$ , which is in good agreement with experimental values. As can be observed through these profiles, the reaction zone is very thin: the heat-release rate is a peak. In addition, the burned state takes time to reach equilibrium: the convergence to the adiabatic flame temperature profile is not directly obtained.

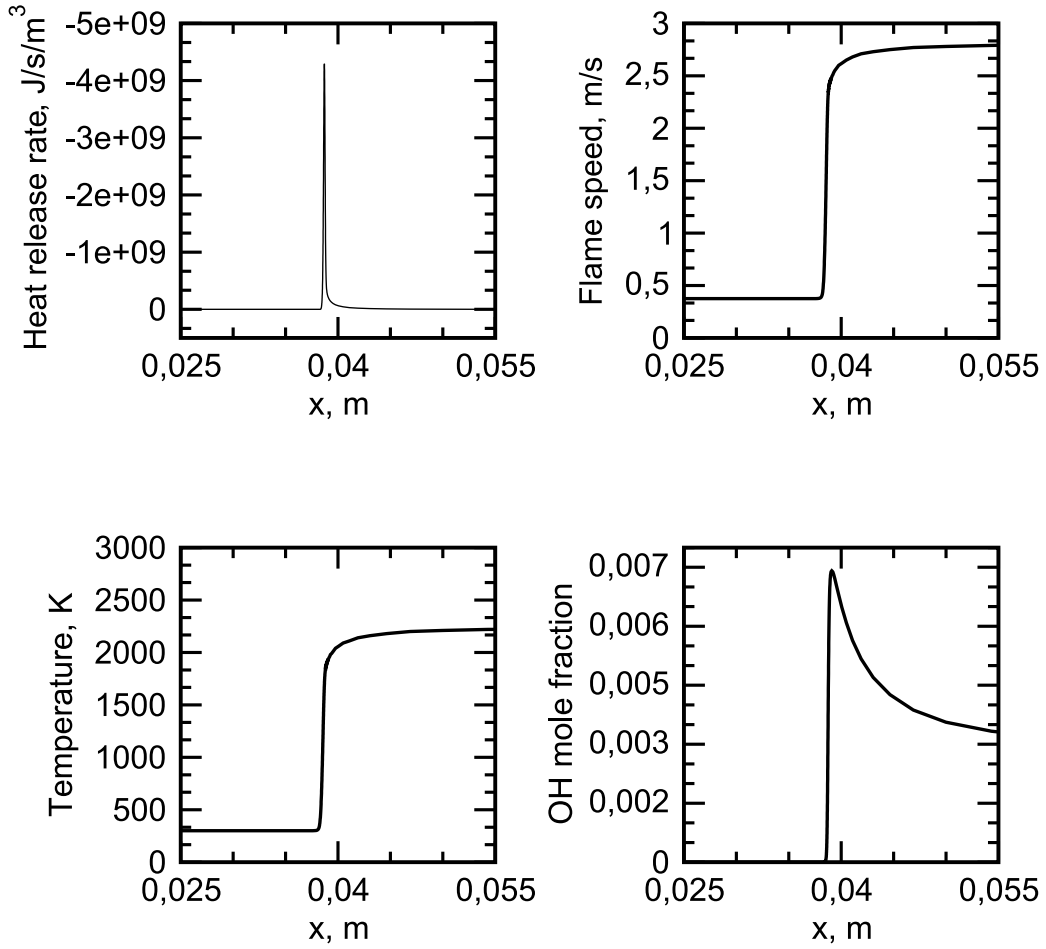


Figure II.4: Computed profiles of heat release rate, velocity, temperature and mole fraction of OH for a stoichiometric methane air flame at 300 K, 0.1 MPa.

## II.3 Flame speed definitions

### II.3.1 Definition

Laminar flame speed computed in 1D code is an eigenvalue of the system (II.20) and corresponds to the velocity of fresh gases that stabilizes the flame sheet in a steady position. Laminar burning velocity satisfies the relation presented below, that applies to fuel mass fraction. Writing the conservation equation of fuel mass fraction  $Y_f$  yields:

$$\rho_u S_l^0 \frac{\partial Y_f}{\partial x} = \frac{\partial}{\partial x} \left( \rho \mathcal{D} \frac{\partial Y_f}{\partial x} \right) + \dot{\omega}_f \quad (\text{II.21})$$

Integrating this relation across the domain between  $-\infty$  and  $+\infty$  and considering that diffusing terms are zero in these positions yields

$$\int_{-\infty}^{+\infty} \rho_u S_l^0 \frac{\partial Y_f}{\partial x} dx = \int_{-\infty}^{+\infty} \dot{\omega}_f dx \quad (\text{II.22})$$

$$S_l^0 = \frac{1}{\rho_u Y_f^u} \int_{-\infty}^{+\infty} \dot{\omega}_f dx$$

where  $Y_f$  in  $+\infty$  is  $Y_f^u$ , the fuel mass fraction of fuel on the fresh gas side, in  $+\infty$ , and  $Y_f$  in  $-\infty$  is zero.

The energy released by the reaction  $[\int_{-\infty}^{+\infty} \dot{\omega}_f dx]$  is directly proportional to the flame speed  $S_l^0$ . For thermodynamical purposes, this laminar flame speed can be associated to a *consumption speed*:  $S_c^0$ . This velocity corresponds to the mass of fuel that burns in the zone defined between the two temperature isolevels  $T_u$  and  $T_{ad}$ . Experimentally, it is not possible to determine laminar burning velocity using this formulation. It represents a global (integral) quantity that does not depends on any considered isothermal. This value is directly linked to  $\dot{\omega}_f$  and must be modeled. That is why new considerations in one-dimensional configuration are described further and pave the way to experimental measurements of laminar burning velocity.

### II.3.2 Absolute and Displacement Speeds

We observe that laminar burning velocity, as defined above with the integral formulation, cannot be obtained by experimental measurement. However, it can be shown that in a planar configuration, it is possible to establish a link between the exact definition of the laminar burning velocity and those that can be achieved by the experiments. Quantities defined in previous sections by various terms – *laminar flame speed, laminar burning velocity or consumption speed*– need to be carefully defined.

Let's consider a representation of a 1D flame where the inlet velocity,  $u_g$ , differs from the laminar burning velocity. In the laboratory frame, depending on the magnitude of  $u_g$ , a flame front can move either forward – towards fresh gases – or backwards – towards burned gases. Fig. II.5 illustrates a generalized form of a reaction layer available at any isolevel surface (in terms of temperature isolevel) surrounded by a fresh gas flow at velocity  $u$ . The local density at this isolevel is  $\rho$ . The typical normal  $\vec{n}$  is orientated towards the fresh gases and different speeds are

observed. Note that all velocities are coplanar.

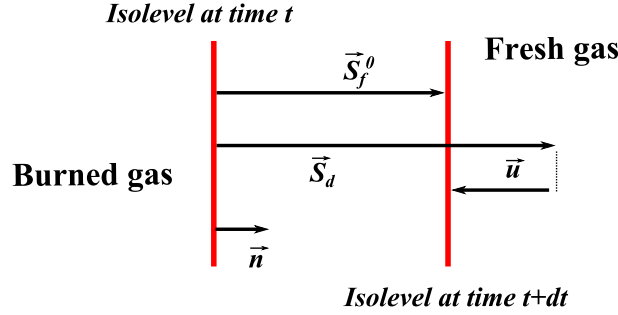


Figure II.5: Illustration of flame layers and corresponding velocities: absolute speed  $\vec{S}_f^0$ , fresh gas velocity  $\vec{u}$  (“seen” by the isothermal considered), and displacement speed  $\vec{S}_d$ .

Kinematically,  $S_f^0 = \vec{S}_f^0 \cdot \vec{n}$ , leads to the definition of the **absolute speed** in the laboratory frame and corresponds to the velocity at which one can observe the flame motion. This quantity is directly linked to a difference in the velocity at which gases are consumed and the one at which fresh gases blow towards the flame front:  $S_f^0 = S_l^0 - u_g$ .  $u_g$  is defined as the fresh gases inlet velocity. It is important to note that the absolute flame speed remains constant whatever the chosen isolevel [28, 26].

In addition,  $S_d^0 = (\vec{S}_f^0 - \vec{u}) \cdot \vec{n}$  leads to a **displacement speed** of the flame front relative to fresh gas. Here, the observer is positioned on a flame isothermal and sees the velocity at which the gases pass through the considered isothermal.

Drawing from the mass continuity equation (Eq. II.4) and because the surface mass flow rate is conserved, we obtain, between the fresh gas side (at fresh gas velocity  $u_g$ ) and any isolevel:

$$\dot{m} = \rho_u (\vec{u}_g - \vec{S}_f^0) \cdot \vec{n} = \rho (\vec{u} - \vec{S}_f^0) \cdot \vec{n} \quad (\text{II.23})$$

$u$  satisfies:

$$u = S_l^0 \left( \frac{\rho_u}{\rho} - 1 \right) + u_g \quad (\text{II.24})$$

Looking more precisely into this relation, if:

- $S_f^0$  is taken at the flame temperature isolevel then it corresponds to the absolute flame speed of the flame front in the laboratory frame

- $u$  is taken at the fresh gas isolevel  $T = T_u$ ,  $u_g$ . It corresponds to a density that is equal to the fresh gas density  $\rho_u$ ,

$$S_d^0 = (\vec{S}_f^0 - \vec{u}_g) \cdot \vec{n} = S_l^0 \quad (\text{II.25})$$

$S_d^0$  corresponds, in the flame front frame, to the relative speed at which the reactants go through the fresh gas isolevel.

Another point must draw our attention and concerns the absolute flame speed  $S_f^0$ . Starting from the mass continuity equation, it is possible to establish a relation between the burned and fresh sides as:

$$\begin{aligned} \frac{dm_u}{dt} &= \frac{dm_b}{dt} \\ \rho_u S_l^0 &= \rho_b^{eq} S_f^0 \\ S_l^0 &= \frac{\rho_b^{eq}}{\rho_u} S_f^0 \end{aligned} \quad (\text{II.26})$$

where  $\rho_b^{eq}$  is the burned gas density supposed uniform and at the equilibrium.

It can be noticed that, due to thermal expansion, the burned gas' flame speed,  $S_f^0$ , is greater than the fresh gas',  $S_l^0$ . This is due to the flow acceleration by thermal expansion  $\frac{\rho_b^{eq}}{\rho_u} < 1$ .

Finally, we conclude that, in planar flames, the relation can be expressed as follows:  $S_d^0 = S_c^0 = S_l^0 = \frac{\rho_b^{eq}}{\rho_u} S_f^0$ .

## II.4 Concluding Remarks

The above section deals with the meaning of the *laminar burning velocity* concept. First, we proposed to examine the flame structure through different levels of complexity, from the simplest to the fully descriptive one. We have exposed the standard structure of a one-dimensional flame defining the preheat and reaction zones. By the expression of the governing 1D equations, we showed that a full analytical and numerical description of the flame in terms of temperature and species is possible. Analytical expressions of the laminar burning velocity can be achieved through the ZFK formulation, for instance. However, this implies important assumptions. Theoretically, the exact formulation of laminar burning velocity is determined by integrating the



---

reaction rate observed along the flame brush – consumption speed. This velocity refers to a *chemical frame*. We have concurrently exposed 1D expressions of the displacement and absolute flame speeds. These velocities depend on the observer’s position. The observer is either positioned on the reference laboratory frame or on the flame front. These velocities are of deep interest because they can be achieved experimentally. However, in real cases, one-dimensional flames configuration does not exist and experimental measurements are achieved with non-planar flames that can be curved or stretched as well. The next chapter illustrates the meaning of these non-planar flames.



## Chapter III

# From planar to stretched flames

One-dimensional flames can not be achieved in experimental configurations. Laboratory flames are not planar and realistic configurations impose curved or stretched flames. However, the flames remain laminar. First, stretch is defined and examples of stretched flames are given. The corresponding expression of flame velocities and stretch are examined. Because the unstretched laminar burning velocity is one of the most fundamental characteristic of a given mixture, analytical formulations will allow us to go from stretched to planar flame velocity. These relations are expressed and flame velocity dependence on stretch is examined from a theoretical point of view.

### III.1 Stretch definition

The previous section describes the ideal flame, where surrounding flow field is uniform and do not disturb the flame's structure. Many practical flame configurations are described in the literature, all of which present specific structures/topologies. Spherical outwardly flames [29, 30, 31, 32, 33, 34, 35, 36, 37, 38], counterflow flames [39, 40, 41, 42, 43], Bunsen burner flames [44, 45, 46] can be observed. This section does not cite the heat flux method because stretch can be neglected; however, this method is rather complex and more details can be found in [47]. In this view, researchers have used the global topology of the flame, that can be curved, non-stationary or non-adiabatic, to introduce a parameter that couples effects of curved flame

motion and surrounding flow field. Williams [48] was the first to introduce stretch as:

$$\kappa = \frac{1}{A} \frac{dA}{dt} \quad (\text{III.1})$$

where  $A$  is the set of points that:

- belongs to the flame surface
- has the same normal velocity as the flame surface
- has the same tangential velocity as the surrounding flow

The figure below (Fig. III.1) shows a description of normal and tangential straining on a flame, represented as a thin sheet, moving at  $S_f$  in the laboratory frame and surrounded by fresh gas at the velocity  $u$ . From a kinematic perspective, it is possible to express the global parameter  $\kappa$

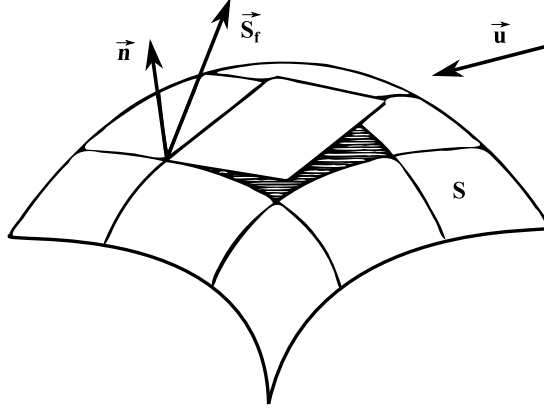


Figure III.1: Schematic of a surface submitted to strain and curvature

regarding its two components [49].

$$\kappa = \vec{S}_f \cdot \vec{n} \mathcal{C} + \mathcal{K}_s \quad (\text{III.2})$$

$$\kappa = S_f^n \mathcal{C} + \mathcal{K}_s$$

where  $\mathcal{C}$  and  $\mathcal{K}_s$  are respectively curvature and strain rate.

$$\begin{aligned} \mathcal{C} &= \nabla \cdot \vec{n} \\ \mathcal{C} &= -\left(\frac{1}{\mathcal{R}_1} + \frac{1}{\mathcal{R}_2}\right) \end{aligned} \quad (\text{III.3})$$

$$\begin{aligned} \mathcal{K}_s &= -\vec{n} \cdot \mathbf{E} \cdot \vec{n} \\ \mathcal{K}_s &= (\vec{u} \cdot \vec{n}) \mathcal{C} + \nabla_\tau \cdot \vec{u}_\tau \end{aligned} \quad (\text{III.4})$$

where  $1/\mathcal{R}_1$  and  $1/\mathcal{R}_2$  are the two radii of curvature.  $\mathbf{E}$  is the rate of strain tensor expressed by:  $\frac{1}{2}(\nabla\vec{u} + (\nabla\vec{u})^T)$ . The first RHS term of Eq. III.4 is normal straining. The second term is for tangential straining. Finally, the stretch factor can be recast as:

$$\begin{aligned}\kappa &= \overbrace{S_f^n \nabla \cdot \vec{n}}^{(1)} + \underbrace{(\vec{u} \cdot \vec{n}) \nabla \cdot \vec{n} + \nabla_\tau \cdot \vec{u}_\tau}_{\text{Global Straining}}^{(2)} + \overbrace{\nabla_\tau \cdot \vec{u}_\tau}^{(3)} \\ \kappa &= (S_f^n - u^n) \nabla \cdot \vec{n} + \nabla_\tau \cdot \vec{u}_\tau \\ \kappa &= (S_d) \nabla \cdot \vec{n} + \nabla_\tau \cdot \vec{u}_\tau\end{aligned}\tag{III.5}$$

$S_f^n - u^n$  expresses the displacement speed  $S_d$ , which is the normal flame speed velocity in the fresh gas reference frame. Further description is available in section II.3.2. Furthermore, analyzing the components (1), (2), and (3) of the equation above (Eq. III.5) and looking at Fig. III.2 the following can be observed:

1. Depending on the sign of the curvature, the normal propagation can expand or contract the flame.
2. Depending on the sign of the curvature, the normal fresh velocity component  $\vec{u} \cdot \vec{n}$  can contract or expand the flame.
3. The divergence of the tangential velocity component creates tangential straining and makes the flame compress or expand.

The first *RHS* term in Eq. III.5 represents the effect of non-stationary curved flame motion. If the flame is not curved,  $\nabla \cdot \vec{n} = 0$ , and this term vanishes. The second *RHS* term is due to local non-uniform flow in the tangential direction. Note that if the local flow velocity is not oblique to  $\vec{n}$ , this term vanishes, [49, 50]. It is important to note that in this situation, the flamelet theory is used. The three-dimensional aspect of the flame, *i.e.* flame shape integrating along the thickness, is not considered. In the case of non-flamelet model, De Goey *et al.* [51] showed that additional terms in the stretch factor appear. They related flame thickness variation with density evolution along the flame brush.

Moreover, additional effects can be found to change flame front structure, as is the case for

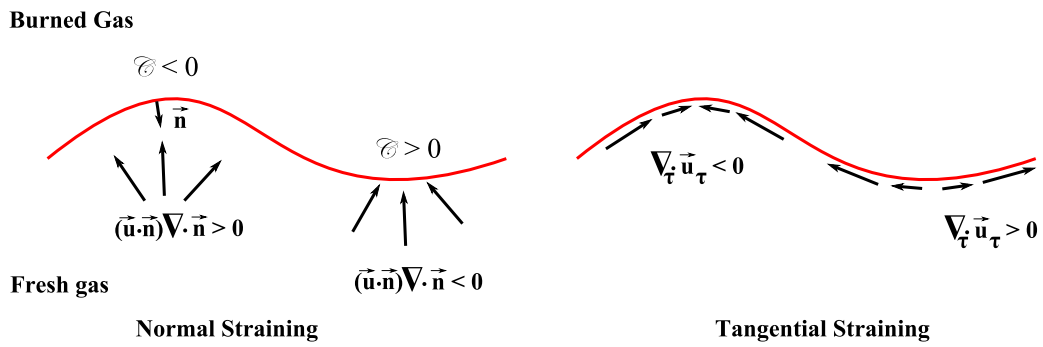


Figure III.2: Curvature and strain effect on stretched flame.

flames submitted to differential thermal and molecular diffusion. Appendix A describes these effects, that can either stabilize or disturb the flame's structure.

## III.2 Stretched flames in literature

This section deals with the presentation of the three main stretched flame configurations used in literature for laminar burning velocity determination. Fig. III.3 presents their schematic and real representation. The main idea is to point out their methodology but also their respective limitations and advantages. The formulations of stretch factor are also given.

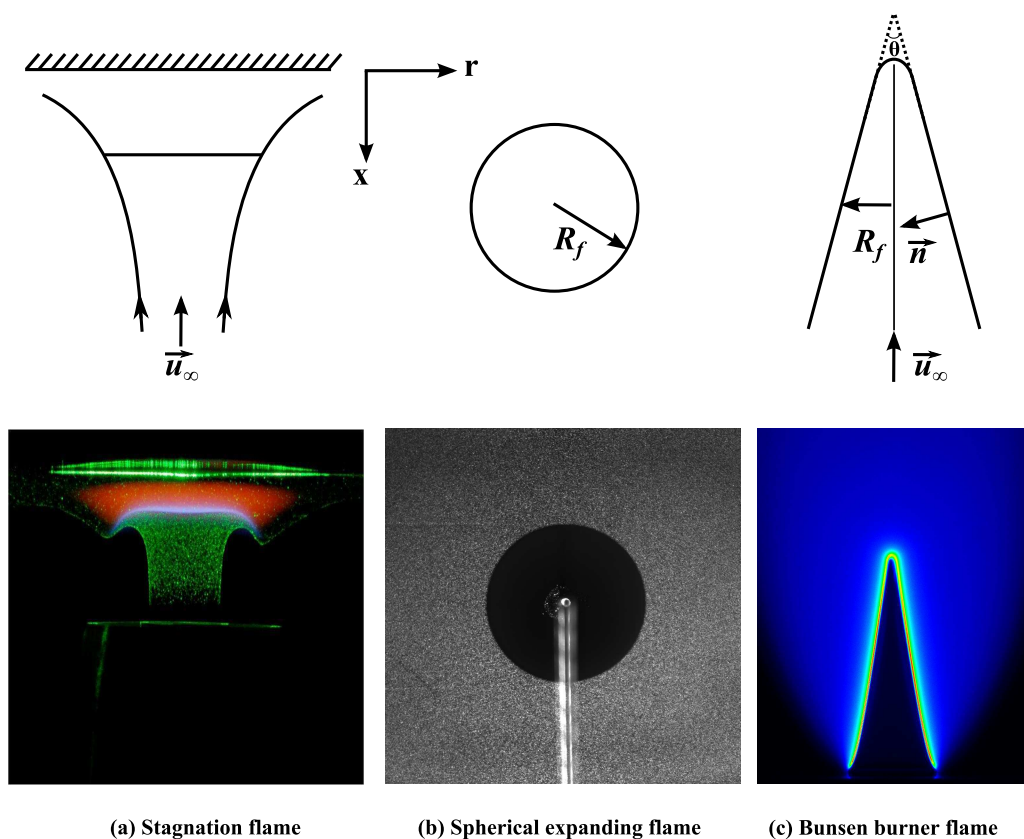


Figure III.3: Representation of stretched flames. Schemes and real visualization. From the left to the right: Stagnation flame, spherical expanding flame and Bunsen burner flame from [50].

- Counterflow flames or stagnation point flame Fig. III.3 (a)

- Description

Experimentally, this technique consists in impinging two symmetrical reactive flows or a premixed mixture on a plate. A stagnation plane is obtained and the flame is subjected to strain due to diverging upstream flow. The technique has been well

documented in these studies [52, 53]. Velocity strongly decelerates before reaching the flame's preheat zone. Hereafter, fresh gases are subjected to thermal expansion and an increase of the burned-flow velocity is consequently observed; see representation Fig. III.4. Theoretically, two models can describe the inlet axial velocity field. The first one is called *Potential Flow Boundary* and its schematic representation is in Fig. III.5(a). In this case, stretch is constant and also depends on the axial inlet velocity. In this case, assuming that  $S_f$  is null (stagnation plane), we observe that, imposing an inlet velocity as:  $\vec{u}_\infty(x, r) = u\vec{x} + v\vec{r}$  with  $u = -ax$ , assuming a non-compressible flow ( $\nabla \cdot \vec{u}_\infty = 0$ ) yields  $v = ar/2$ . Stretch  $k$ , (Eq. III.5) is then directly equal to  $a$  and is positive. The second situation is called *Plug Flow Boundary*, see Fig. III.5(b), and corresponds to more realistic experimental flames. Here, stretch is usually equal to the maximum gradient in the velocity profile upstream the flame. Moreover, as reported in Bouvet's thesis [16], experimentally, it is preferable to use the radial strain rate determination instead of the approach using the axial velocity because the latter is less accurate.

Determining laminar burning velocity is a complex task and different views are reported. For Law and Wu [50], the flame front is located at the isothermal thermo-diffusive zone. The stretched unburned velocity and corresponding gradient are extracted at the point called  $u_{Ref}$ . However, for Clavin and Joulin, [54], the flame front is located at *last combustion isolevel*. We therefore need to extrapolate stretched flow velocity at the extreme isolevel flame front position, abscissa  $x = 0$  in graph III.4. It is a virtual flow velocity equal to the one in a cold flow at this isolevel position. This velocity is called  $u_{Extrap}$ . These two quantities are correlated as follows:  $u_{Ref} = u_{Extrap} - \delta \frac{du}{dx}_{x=0}$  where  $\delta$  is the flame thickness (transport and reactive zones). In practical cases, the  $u_{ref}$  is chosen but one must be careful when comparing experimental or numerical data.

#### – Advantages

The main advantage of this technique is that the flame is kept away from the burner



exit and heat transfers to the burner are limited. The inlet flow can be easily insulated from ambient gas and pushed away from the burner lips, generally by  $N_2$  co-flow. However, this co-flow can influence the flame stagnation plane as reported in [16]. Another advantage of the technique is that species profiles and flow velocimetry can be performed quite easily because the flame is stationary.

– **Drawbacks**

Very few experimental studies report the use of counterflow flame at high pressure due to the development of unstable or oscillating flame. Generally, experiments can be achieved up to several bars and very few studies up to 1 MPa [16, 55]. The system must be adapted with a housing positioned around the burner. However, it is important to adequately stabilize the flame by adjusting the  $N_2$  co-flow and the separating distance between the two burners in the case of twin counterflow flames. As describe above, the choice of a reference plane is needed for laminar burning velocity and strain.

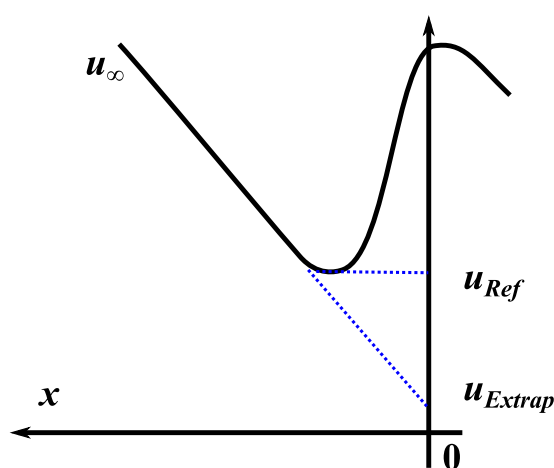


Figure III.4: Stagnation plane flame. Stretched fresh gases velocity determination.

• **Spherical expanding flame Fig. III.3 (b)**

– **Description**

This technique consists in centrally ignite an homogeneous combustible mixture in a

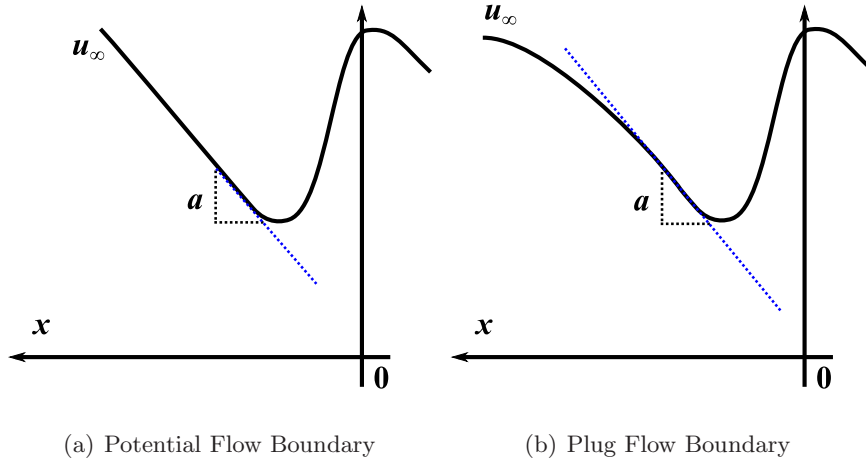


Figure III.5: Stagnation plane flame, velocities and boundary conditions.

closed vessel of  $R^0$  internal radius. A propagating expanding flame develops from the ignition point to the fresh gases. Two methods can be used to measure flame speed. The experiment consists in recording either the flame front – space-measured – or the pressure rise history – time-measured – and makes it possible to determine laminar burning velocity.

- \* **The constant pressure method:** The time rate of change of  $R_f$  is measured in the laboratory frame, by either tomographic III.6 or Schlieren III.7 images. The time derivative radius function gives the flame speed  $S_f$  as  $S_f = \frac{dR_f}{dt}$ . Considering a large radius chamber, studies have shown a quasi-steady state stage where the flame is almost not affected by ignition energy (in the early stage) or by pressure rise (later stage). In this view, pressure rise (and temperature) due to compression is assumed to be neglected and the flame is only affected by stretch (strain and curvature). Also, because flame radii are small enough, flame surface instabilities such as cellular instabilities have no time to develop. The stretched burning velocity is obtained thanks to the *density ratio method* (mass conservation equation through the flame) that gives  $S_l = \frac{\rho_b}{\rho_u} S_f$ . The calculation of  $\kappa$  is determined thanks to the surface ( $\mathcal{A}$ ) evolution where  $\mathcal{A}$  grows with time:  $\mathcal{A} = 4\pi R_f^2$  in 2D configuration. It yields to  $\kappa = \frac{2}{R_f} \frac{dR_f}{dt}$ . Also, it is possible to see the separated effects of strain and curvature for this flame topology as Eq. III.5,

as exposed in the table below (III.2):

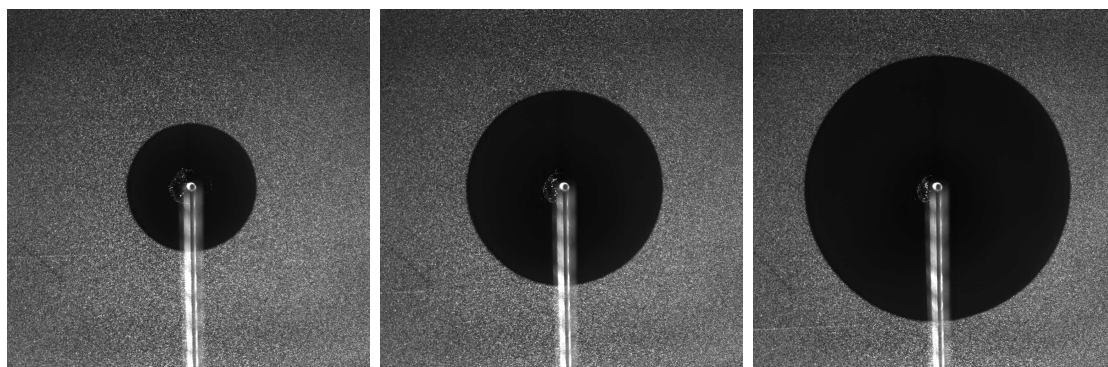


Figure III.6: Tomographic visualization of a propagation sequence of a stoichiometric methane/air flame at  $P=0.1$  MPa,  $T=298$  K, from present work.

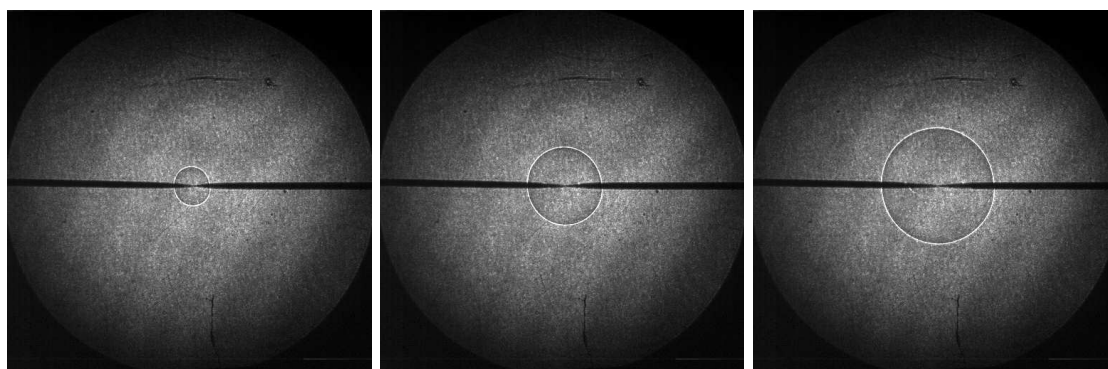
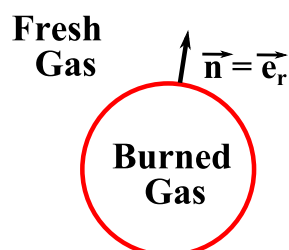


Figure III.7: Schlieren visualization of a propagation sequence of a stoichiometric methane/air flame at  $P=0.1$  MPa,  $T=300$  K, from [38].



Stretch due to		Total Stretch
Curvature	Strain	$\kappa$
$\frac{2}{R_f} S_d$	$\frac{2}{R_f} u$	$\frac{2}{R_f} (S_d - u)$
		$\frac{2}{R_f} S_f$

- \* **The constant volume method:** The pressure chamber history, *i.e.*  $P$ , is recorded during the propagation of the spherical expanding flame in the vessel. Deriving the equations governing the flame propagation leads to different expres-

sions of the stretched burning velocity considering the burned or fresh side. Those equations are not developed here but are fully described in the next chapter. As mentioned in [17], in the early stages of the flame propagation, *i.e.*  $R_f \ll R^0$ , pressure rise is very small, and in this *prepressure* period, measurements need an extremely accurate pressure sensor and mostly lead to misestimations.

– **Advantages**

These techniques are designed for high pressure and temperature conditions, where other techniques, such as counterflow, rim-stabilized and flat flame burners are not convenient. They have been largely used since 1980, for they are a good compromise between accuracy and a large range of possibilities (large equivalence ratios, temperature, pressure). The effect of stretch (strain and curvature) extracted from the flame's topology (flame radius) can be properly integrated, which is a crucial point for zero stretch extrapolation.

– **Drawbacks**

Spherical expanding flame techniques require important installations, including a robust chamber with resistant optical accesses and sensors for controls. Similarly, implementing chain measurement can be rather complex. This leads to an expansive experimental setup and requires high-level technical staff with adequate background. Spark ignition remains a problem. It can generate instability and moreover, primary flame propagation records can not be used because of the remaining influence of the deposit of energy. A critical minimum radius is imposed, below which measurement is not relevant. Furthermore, for the constant pressure method, it is essential to check that pressure rise is limited. Generally, a maximum radius of 1/3 of the chamber radius is selected in order to prevent any influence by pressure rise [56].

It is worth noting that this technique assumes a zero burned gas velocity that is not necessarily verified. Moreover, for both of these techniques, the article [57] reports some errors that are introduced by the assumptions inherent to these two methods. This paper shows that for the constant pressure method, the induced flow velocity by

compression might be taken into account for accurate measurement. Moreover, the upper flame radius that ensures that flame is not affected by pressure rise seems to be restricted.

- **Rim-stabilized flame:**

- **Description**

This method can also use Bunsen burner with circular exit or 2D slot burner Fig. III.3 (c).

The technique consists in visualizing a slice of the (axi)-symmetrical flame by Schlieren or chemiluminescence. The absolute flame speed is null – steady configuration – and the stretch factor is expressed as:  $\kappa = -\frac{u_\infty \sin(\theta)}{2R_f}$ . The flame is subjected to both strain and curvature. Methodology for burning velocity determination follows to ways:

- \* Applying the mass conservation equation over the entire surface area of the flame  $\mathcal{A}$ , the flame speed is given by:  $S_l = \dot{Q}_v / \mathcal{A}$ , where  $\dot{Q}_v$  is the volumetric flow rate.
- \* The normal component velocity to the flame front is directly linked to the cone apex angle  $\theta$ :  $S_l = -\vec{u}_\infty \cdot \vec{n} = u_\infty \sin(\theta)$ .

- **Advantages**

One of the main advantages is that the experimental setup configuration is very simple and experiments are easy to conduct. It is the cheapest way to estimate laminar burning velocity at atmospheric pressure.

- **Drawbacks**

This technique involves assumptions that neglect strain effects or heat losses at the burner's lips. It is important to mention that non equi-diffusive mixtures affect the cone apex, which is strongly curved, resulting in a modification of the cold flow. This point is rarely taken into account. Nevertheless, for slot burners, Selle *et al.* [58] have quantified the three-dimensional errors by computing a two-dimensional DNS.

They also carried out an experimental determination of the true velocity profiles at the burner exit for 3D-error correction. They finally found that  $S_l^0 = \eta S_l$  where  $\eta$  is a correction factor for the above-mentioned errors.

### III.2.1 Extrapolation to zero stretch

Looking at the evolution of methane maximum velocity over the years (Fig. III.8), we observe that the large discrepancy in measurement before the 80s – about 25 cm/s – tends to fall to  $\approx 2$  cm/s in the last decade. Even though experimental techniques and methodologies have noticeably progressed over the last 30 years (High speed recording as tomography, PIV, Schlieren), the discrepancy can be explained by the fact that before the 80s, stretch effect was not considered. Wu and Law [19] were the first to show the importance of stretch and its effect on experimental flame. Linear formulations were consequently used, followed by non-linear techniques that allowed variance in measurements to be further reduced. The non-linear formulation is the generalized expression which can be applied even for highly-stretched flames. These elements show the importance of the stretch extrapolation technique, which makes it possible to determine the unstretched laminar burning velocity from stretched flame record.

As said in the previous section, adiabaticity, flow straining, flame curvature, and non-stationary flame affect laminar burning velocity. Considering that a flame is perturbed in terms of enthalpy loss, or gain, from its transport zone by the mechanisms described previously, it is possible to determine a non-linear relation between a stretched velocity and its corresponding unstretched one as [18]:

$$\tilde{s}^2 \ln \tilde{s}^2 = -2\sigma \quad (\text{III.6})$$

where  $\tilde{s} = s/s^0$ .  $s$  can be either  $S_f$ ,  $S_d$  or  $S_c$ .  $\sigma$  is found to be a generalized gain/loss parameter as  $\sigma = L\kappa/s^0$ .  $L$  measures the sensitivity of the flame speed, displacement speed or consumption speed to stretch and refers to as the Markstein length.

In the case of weakly-stretched flames assuming small variations of the flame speed from the unstretched value, *i.e.*  $\sigma$ , is small, the non linear relation linearizes to:

$$\tilde{s} = 1 - \sigma \quad (\text{III.7})$$

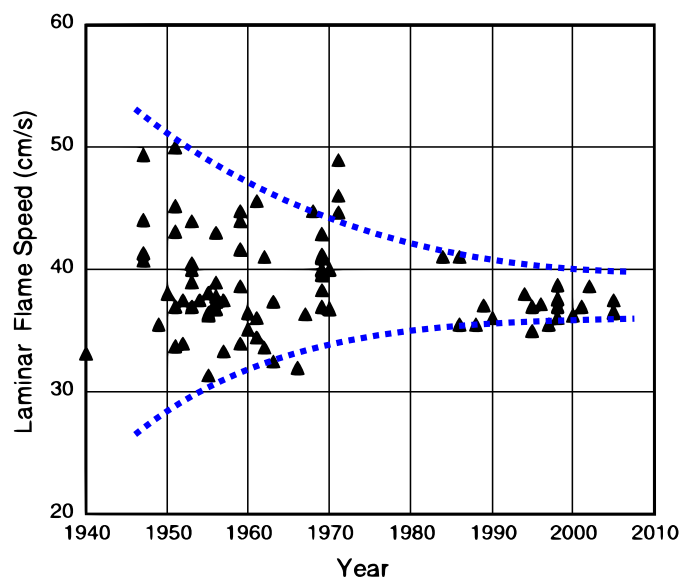


Figure III.8: Methane maximum velocity over the years showing the scatter discrepancy progression to be less than  $\pm 2$  cm/s,  $P=0.1$ , ambient temperature, from Law *et al.* [18]

As shown in Fig. 5 of Kelley and Law's article [20], or Halter *et al.* [59, 60] reproduced here in Fig. III.9, the non-linear and linear relationships, respectively III.6 and III.7, give different trends, except for very small values of  $|\sigma|$ .

In those linear or non-linear relations, the sensitivity to stretch – Markstein length – appears.

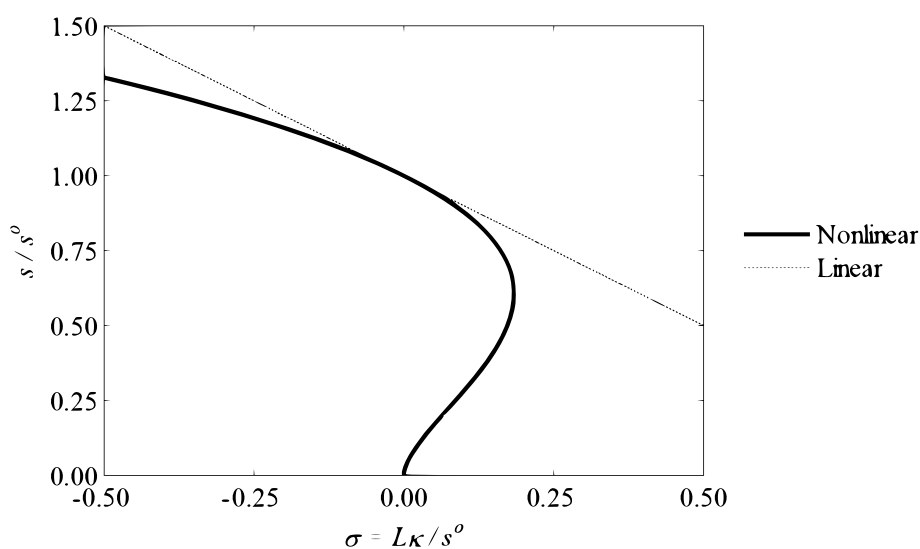


Figure III.9: Comparison of the non-linear and linear relationships between flame speed and stretch, from [20]

Markstein length is difficult to determine experimentally. Even though in terms of laminar flame speed, the discrepancy can nowadays be less than  $\pm 2 \text{ cm/s}$ , *i.e.* less than 10%, the discrepancy in Markstein lengths can reach about 300%, depending on the extrapolation technique that is used. As explained in [61], one possible interpretation of such data variation is that experimental points are out of the range of validity of the linear and non-linear relation. This shows the real importance of respecting the basic hypothesis for velocity extrapolation to zero stretch. In the case of constant-pressure expanding flames, Chen [61] tested, numerically and experimentally, the validity of the linear and non-linear relations in terms of laminar burning speed and Markstein lengths. He also mentioned the existence of another non-linear formulation. He found that these models are extremely sensitive to the Lewis number and care must be taken when using one or the other formulation.

### III.2.2 Markstein lengths / Markstein numbers: analytical solutions

Phenomenological considerations, as described above, establish a link between stretched velocities and unstretched ones. In those developments, the stretch factor appears to be a scalar that controls normal burning velocity. Flame sensitivity to stretch is found to be highlighted by Markstein length. The latter can be explicitly written as a function of the physico-chemical properties of the mixture by an analytical formulation, in the case of weakly-stretched flames. We introduce two parameters, called Markstein and Karlovitz numbers, which are defined in a generalized form, as:

$$Ma = \frac{L}{\delta_p} \quad (\text{III.8})$$

$$Ka = \frac{\delta_p}{s^0} \kappa \quad (\text{III.9})$$

$\delta_p$  is found to be the thermal thickness given by Eq. II.1.  $L$  and  $s^0$  are respectively the generalized Markstein length and unstretched velocity.

The linear formulation III.6 may be recast, for:

- Displacement speed

$$\frac{S_d}{S_d^0} = 1 - Ma^d Ka \quad (\text{III.10})$$



Clavin and Williams [62] proposed expressions for Markstein numbers considering the fresh side,  $Ma^d$ . In the case of a flame with variable density and a one-step overall chemical reaction, one can find, for the fresh side:

$$Ma^d = \frac{L_d}{\delta_p} = \frac{1}{\gamma} \ln\left(\frac{1}{1-\gamma}\right) + \beta \frac{Le-1}{2} \left(\frac{1-\gamma}{\gamma}\right) \int_0^{\frac{\gamma}{1-\gamma}} \frac{\ln(1+x)}{x} dx \quad (\text{III.11})$$

where  $\beta$  is the reduced activation energy,  $\gamma$  is the expansion parameter defined as  $\gamma = 1 - \rho_b/\rho_u$ . Considering that for ordinary mixtures,  $\gamma$  is found to be greater than 0.8, this Markstein number,  $Ma^d$ , takes strictly positive values. Hence, and looking at the linear relation III.10, positive stretch seems to have a stabilizing effect by lowering burning velocity. However,  $Ma^d$  can sometimes take negative values, depending on a critical Lewis number,  $Le_c$  yielding:

$$Le_c^d = 1 - \frac{1}{\beta} \frac{2}{1-\gamma} \ln\left(\frac{1}{1-\gamma}\right) / \int_0^{\frac{\gamma}{1-\gamma}} \frac{\ln(1+x)}{x} dx \quad (\text{III.12})$$

In the case of very non equi-diffusive flames such as very lean hydrogen flame,  $Le_c$  can be reached and negative values of  $Ma^d$  can be found as developed in the asymptotic theory in [63].

However, particular attention must be paid to the choice of the isotherm to define  $S_d$ . This choice not only influences the value of  $Ma^d(L_d)$ , but can also reverse its dependence on the stretch [64, 65]. Classically, the isothermal corresponding to the entrance of the preheat zone is chosen because, as described above,  $S_d^0$  and  $S_c^0$  are identical. However, in the literature, as summarized in Baillot *et al.* [66], different front locations have been employed for displacement speed estimation, leading to different values of  $L_d$ : the isotherm at the beginning of the thermal-diffusive thickness [28, 19, 67, 68], the isotherm of the maximal final combustion temperature [54], or the iso-scalar of the fuel mass fraction [69]. Regarding the chosen isothermal, Davis *et al.* [70] reported, in a numerical study, the differences plotting the evolution of the Markstein number –  $Ma^d$  – for different extraction positions (Fig. III.10). They also found that, according to the theory and previous studies,  $Ma^d$  is very sensitive to the chosen isothermal and changes sign from the unburned to the burned side. Special attention must therefore be paid when comparing data.

- Absolute flame speed / Propagation speed

$$\frac{S_f}{S_f^0} = 1 - Ma^b Ka \quad (\text{III.13})$$

Looking at the burned side, we obtain a similar expression of the Markstein number relative to burned gases –  $Ma^b$  – as [63]:

$$Ma^b = \frac{L_b}{\delta_p} = \frac{1}{\gamma} \left\{ \ln\left(\frac{1}{1-\gamma}\right) + \beta \frac{Le-1}{2} \left(\frac{1-\gamma}{\gamma}\right) \int_0^{\frac{\gamma}{1-\gamma}} \frac{\ln(1+x)}{x} dx \right\} \quad (\text{III.14})$$

$$Le_c^b = 1 - 2 \frac{1}{\beta} \ln\left(\frac{1}{1-\gamma}\right) \frac{\gamma}{1-\gamma} / \int_0^{\frac{\gamma}{1-\gamma}} \frac{\ln(1+x)}{x} dx \quad (\text{III.15})$$

The expression of  $Ma^b$  and  $Ma^d$  are similar and give, up to a factor  $\gamma$  in the second RHS term, the same critical Lewis number. However, the change of sign, depending on the value of  $\beta(Le-1)$  can be more easily obtained for standard mixture, as described in [63]. As explained in [63], this contradiction can be justified by the fact that the flame is modified differently by the flow field according to whether burned or unburned gases are concerned. Furthermore, theory has also shown that even if  $S_d^0 = \rho_b/\rho_u S_f^0$ ,  $L_d \neq \rho_b/\rho_u L_b$ . Davis *et al.* in [70] computed methane-air and propane-air flames in a counterflow configuration using a detailed chemical kinetic (469 reactions 71 species). Fig. III.10 shows a flame crossing from fresh side (LHS) to burned side (RHS). They report the reaction rate, and different Markstein Numbers:  $Ma' = \rho_b/\rho_u Ma^d$  and  $Ma^d$ , the displacement-speed-associated Markstein number. They showed in their study that  $Ma' = \rho_b/\rho_u Ma^d$  and  $Ma^d$  clearly differ.  $Ma^d$  varies much more than  $Ma'$  when going through the flame. However, the determination of  $Ma^b$  seems to be more accurate because both variations of absolute flame speed and stretch in the burned side are less dependent on the chosen isothermal.

- Consumption speed

Regarding consumption speed and the impact of stretch, the observed linear relation is

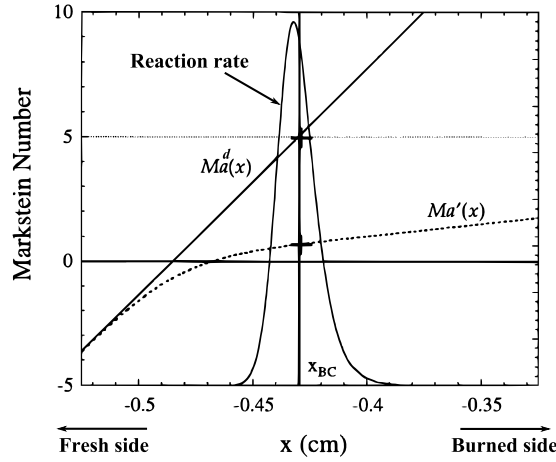


Figure III.10: Variation of Markstein lengths,  $Ma' = \rho_b/\rho_u Ma^d$  and  $Ma^d$ , across the flame front.

similar to those described above:

$$\frac{S_c}{S_c^0} = 1 - Ma^c Ka \quad (\text{III.16})$$

As evoked in [71], we observe the following consumption-speed-related Markstein length relation:

$$Ma^c = \frac{L_c}{\delta_p} = \beta \frac{Le - 1}{2} \left( \frac{1 - \gamma}{\gamma} \right) \int_0^{\frac{\gamma}{1-\gamma}} \frac{\ln(1+x)}{x} dx \quad (\text{III.17})$$

In this case, the critical Lewis number, that triggers a change of slope corresponds to unity.

These asymptotic relations make it possible to determine to what extent Markstein lengths associated with various velocities – displacement speed ( $S_d$ ), flame speed,  $S_f$ , consumption speed ( $S_c$ ) – depend on critical Lewis numbers. This notion is summarized in Tab. III.1. Theoretically,  $L_c$  changes sign for unity Lewis numbers whereas  $L_d$  or  $L_b$  change sign for their respective critical Lewis number.

Lewis number	$L_d$ or $L_b$	$L_c$
0	-	-
$Le_c$	0	-
1	+	0
$\infty$	+	+

Table III.1: Markstein length evolution against Lewis numbers.

### III.3 Concluding Remarks

In this section, the link between theoretical flame analysis and real experimental flames is investigated. The case of real stretched flames is discussed and phenomenological considerations establish that the stretch factor appears to be the scalar that controls the burning velocity. Various experimental setups are reviewed: counterflow, spherical and rim-stabilized flames. The expression of stretch factor in each case is discussed and the way to extract the stretched burning velocity is exposed. Their respective advantages and drawbacks are pointed out. The spherical flame technique seem to be the best candidate to determine laminar burning velocity from stretched flames because of its large range of use in terms of pressure temperature and equivalence ratio. Moreover, the spherical expanding flame enables us to determine, with high accuracy, the stretch factor calculated using the flame topology (radius). Unlike counterflow flames, the velocity field is not needed to determine stretch. Depending on the velocities considered – flame speed, displacement speed or consumption speed –, the expressions of Markstein lengths/numbers – flame velocity sensitivity to stretch – may change sign depending on a critical Lewis number. This parameter is crucial in the analysis of the flame’s sensitivity to stretch. However, determining Lewis number for reacting mixtures is difficult to achieve because, in reactive systems, we observe many Lewis numbers and some discrepancies with theoretical development may appear.

## Chapter IV

# On the determination of the consumption speed of spherically expanding flames

In this chapter, consumption speed equations are developed according to spherical coordinates. As described previously, consumption speed is associated with a *chemical scale*. Consumption speed in 1D flames, as expressed in Chapter II (Eq. II.22), is generalized for any species  $k$  in the case of spherically expanding flames [71]:

$$S_c = \frac{1}{R_f^2 \rho_u [Y_k^b - Y_k^u]} \int_0^{+\infty} r^2 \dot{\omega}_k dr \quad (\text{IV.1})$$

where  $Y_k^b, Y_k^u$  are respectively the values of the mass fraction of species  $k$  in burned and fresh gases. This expression gives the definition of consumption speed for any species considering a one-step reaction: reactants  $\rightarrow$  products,  $k$  is either reactants or products.

However, the source term  $-\dot{\omega}_k$  is unknown. Integrating the species transport equation along the domain, we observe the following:

$$\int_0^{+\infty} r^2 \dot{\omega}_k dr = \frac{d}{dt} \int_0^{+\infty} r^2 \rho Y_k dr \quad (\text{IV.2})$$

so that the consumption speed can be expressed as:

$$S_c = \frac{1}{R_f^2 \rho_u [Y_k^b - Y_k^u]} \frac{d}{dt} \int_0^{+\infty} r^2 \rho Y_k dr \quad (\text{IV.3})$$

$\rho Y_k$  is unknown and can take different values considering a finite or infinitely thin flame thickness. In this chapter, we will investigate this equation for spherically expanding flame, exploring two different cases.

## IV.1 Consumption speed under the infinitely thin flame assumption

The representation of an infinitely thin flame is shown in Fig. IV.1. The flame radius is positioned at  $R_f = R_u = R_b$ . With the one-step reaction, we investigate both the fresh and burned gas

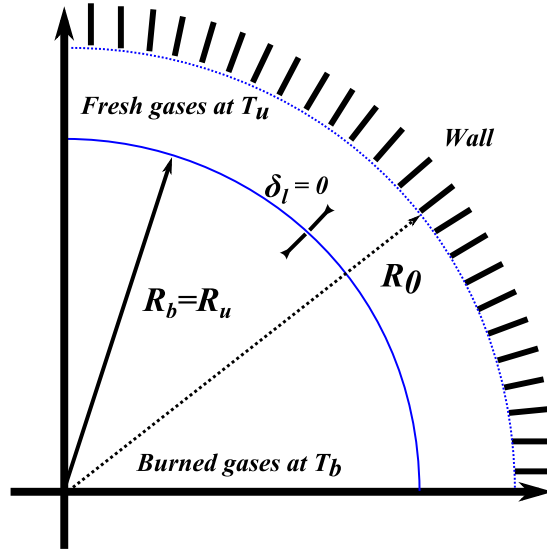


Figure IV.1: Scheme of a spherical infinitely thin flame

species, and the expressions of consumption speed yields:

### 1. Fresh gas side

On the fresh side, the values of  $Y_u^b = 0$  and  $Y_u^u = 1$ .  $S_c$  can be broken down as follows:

$$S_c = -\frac{1}{R_f^2 \rho_u} \frac{d}{dt} \left[ \int_0^{R_f} r^2 \rho Y_u dr + \int_{R_f}^{R_0} r^2 \rho Y_u dr \right] \quad (\text{IV.4})$$

Assuming that on the fresh side  $\rho = \rho_u$ , does not vary in space,  $Y_u = Y_u^u = 1$  and that on

the burned side, no fresh gas remains:

$$\begin{aligned}
 S_c &= -\frac{1}{R_f^2 \rho_u} \frac{d}{dt} \left[ \int_{R_f}^{R_0} r^2 \rho_u Y_u dr \right] \\
 S_c &= -\frac{1}{R_f^2 \rho_u} \frac{d}{dt} \left[ \rho_u \int_{R_f}^{R_0} r^2 dr \right] \\
 S_c &= -\frac{1}{R_f^2 \rho_u} \frac{d}{dt} \left[ \rho_u \frac{1}{3} (R_0^3 - R_f^3) \right] \\
 S_c &= \frac{dR_f}{dt} - \frac{R_0^3 - R_f^3}{3R_f^2 \rho_u} \frac{d\rho_u}{dt}
 \end{aligned} \tag{IV.5}$$

Considering an isentropic compression assumption ( $P\rho_u^{-\gamma_u} = cte$ ), Eq. IV.5 yields:

$$\boxed{S_c = \frac{dR_f}{dt} - \frac{(R_0^3 - R_f^3)}{3R_f^2} \frac{1}{\gamma_u P} \frac{dP}{dt}} \tag{IV.6}$$

In further developments, expression IV.6 will be referred to as Mitcheson's formulation, for it comes from Bradley and Mitcheson's [72]. More recently, Bonhomme et al. [73] have also derived this equation and used it for consumption speed.

## 2. Burned gas side

The same work as above can be done by deriving the equation for the burned gases side.

In this case  $Y_b^b = 1$  and  $Y_b^u = 0$ .  $S_c$  can be decomposed as:

$$S_c = \frac{1}{R_f^2 \rho_u} \frac{d}{dt} \left[ \int_0^{R_f} r^2 \rho Y_b dr + \int_{R_f}^{R_0} r^2 \rho Y_b dr \right] \tag{IV.7}$$

Assuming that on the burned side  $\rho = \rho_b$  does not vary in space, that  $Y_b = Y_b^b = 1$  and that there are no burned gases on the fresh side:

$$\begin{aligned}
 S_c &= \frac{1}{R_f^2 \rho_u} \frac{d}{dt} \left[ \int_0^{R_f} r^2 \rho_b Y_b dr \right] \\
 S_c &= \frac{1}{R_f^2 \rho_u} \frac{d}{dt} \left[ \rho_b \int_0^{R_f} r^2 dr \right] \\
 S_c &= \frac{1}{R_f^2 \rho_u} \frac{d}{dt} \left[ \rho_b \frac{1}{3} R_f^3 \right] \\
 S_c &= \frac{\rho_b}{\rho_u} \frac{dR_f}{dt} + \frac{R_f}{3\rho_u} \frac{d\rho_b}{dt}
 \end{aligned} \tag{IV.8}$$

Considering an isentropic compression assumption ( $P\rho_b^{-\gamma_b} = cte$ ), Eq. IV.8 yields:

$$\boxed{S_c = \frac{\rho_b}{\rho_u} \frac{dR_f}{dt} + \frac{\rho_b}{\rho_u} \frac{R_f}{3\gamma_b P} \frac{dP}{dt}} \tag{IV.9}$$

The main difficulty in this expression remains the estimation of the burned gas density – mean spatial value – and its evolution in time. In fact, stretch (strain and curvature) affects the flame’s temperature and, therefore, the burned gases’ value. If  $\rho_b$  and its evolution are known, (DNS), equations IV.9 and IV.6 must be equal. Furthermore, as explained in Bradley *et al.* [17], where the different ways to determine laminar burning velocities from experiments (spherical flames, flat burners, tubes) are reviewed, the values of laminar burning velocity obtained with the two previous developments Eq. IV.6 and IV.9 are not accurate. This may result from the difficulty to obtain a good resolution of the pressure signal. The latter is even greater in the early stages of the flame’s development, when pressure rise is close to zero – *pre-pressure period*. However, with the improvement of technologies which are, quite logically, more accurate nowadays (40 years later), we can reasonably hope for more satisfactory results. This point will be developed in chapter VIII in which Mitcheson’s formulation will be applied and analyzed.

### 3. Link with the Absolute flame speed / Propagation speed

By a simple observation in the laboratory frame, one can measure the time rate of change of the flame radius  $R_b$  or  $R_u$  as described in III.2. The time derivative radius function gives the flame speed  $S_f$  as  $S_f = \frac{dR_f}{dt}$ . This propagation speed is associated to the burned side by the visualization of the velocity at which the burned gases expand. Generally, the spherical expanding flame is used under the assumption of constant pressure. In this case, it is possible to recast the expression of the consumption speed, Eq. IV.9 where the time derivative pressure term vanishes:

$$\boxed{S_c = \frac{\rho_b}{\rho_u} \frac{dR_f}{dt}} \quad (\text{IV.10})$$

### 4. Displacement speed

Displacement speed described in previous sections corresponds to the velocity at which fresh gases entered the preheat zone. The observer is positioned at the fresh gas isothermal,  $T = T_u$  and sees the velocity at which the gases go through the considered isothermal. As



explained in [28], this speed can be expressed as:

$$\frac{dm_u}{dt} = -4\pi R_u^2 \rho_u S_d. \quad (\text{IV.11})$$

Moreover, considering the spherical expanding flame, the mass variation of fresh gases corresponds to the time derivative function of the mass of fresh gases within the sphere of radius  $R_f$ :

$$\frac{dm_u}{dt} = -\frac{d}{dt} \left[ \int_0^{R_f} 4\pi r^2 \rho dr \right] \quad (\text{IV.12})$$

This expression comes from the equality:  $\frac{dm_u}{dt} = -\frac{dm_b}{dt}$ , where  $\frac{dm_b}{dt} = \frac{d}{dt} \int_0^{R_f} 4\pi r^2 \rho dr$ .

Because of the assumption of an infinitely thin flame, the density at the position within the sphere of radius  $R = R_f$  is  $\rho_b$  and the equation yields to:

$$\begin{aligned} S_d &= \frac{1}{R_f^2 \rho_u} \frac{d}{dt} \left[ \int_0^{R_f} \rho r^2 dr \right] \\ S_d &= \frac{1}{R_f^2 \rho_u} \frac{d}{dt} \left[ \rho_b \int_0^{R_f} r^2 dr \right] \end{aligned} \quad (\text{IV.13})$$

and the expression of  $S_c$  considering the burned gases side is recovered IV.6:  $S_d = S_c$ .

Furthermore, considering that:

$$\frac{dm_u}{dt} = \frac{d}{dt} \int_{R_f}^{R_0} 4\pi r^2 \rho dr$$

The same development can be applied and leads to equality between  $S_d$  and  $S_c$  calculated from the fresh gas side IV.6.

Finally, results obtained in infinitely thin flames are identical to 1D flame results:

$$\boxed{S_c = S_d = \frac{\rho_b}{\rho_u} \frac{dR_f}{dt}}$$

## IV.2 Consumption speed in finite flame thickness

The same spherically expanding flame is described but it is now considered under a finite flame thickness consideration. Closed vessel of  $R_0$  internal radius and one-step chemistry are preserved.

In this configuration, fresh gases consumption starts at the  $R = R_u$  radius. Their concentration decreases when going through the flame and reaches 0 on the burned side. Burned gases start appearing in the flame front. All these notions are described in Fig. IV.2. Consumption velocity

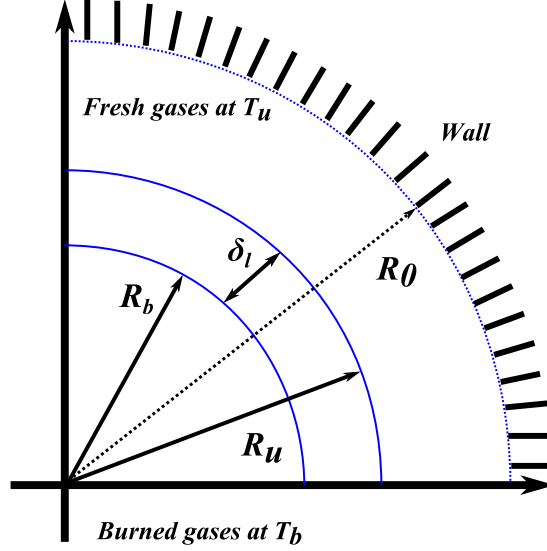


Figure IV.2: Scheme of a spherically finite flame thickness.

equations are developed for fresh and burned gas sides.

### 1. Fresh gas side

On the fresh side, the values of  $Y_u^b = 0$  and  $Y_u^u = 1$ .  $S_c$  can be broken down as:

$$S_c = -\frac{1}{R_f^2 \rho_u} \frac{d}{dt} \left[ \int_0^{R_b} r^2 \rho Y_u dr + \int_{R_b}^{R_u} r^2 \rho Y_u dr + \int_{R_u}^{R_0} r^2 \rho Y_u dr \right] \quad (\text{IV.14})$$

Assuming:

- $R_f \approx R_u \approx R_b$
- On the fresh side  $\rho = \rho_u$ , does not vary in space
- $Y_u = Y_u^u = 1$  in the fresh side
- On the burned side no fresh gas remains
- isentropic compression assumption ( $P \rho_u^{-\gamma_u} = cte$ )

Mitcheson's equation is recovered with an additional term:

$$\begin{aligned}
 S_c &= -\frac{1}{R_f^2 \rho_u} \frac{d}{dt} \left[ \int_{R_b}^{R_u} r^2 \rho Y_u dr + \int_{R_u}^{R_0} r^2 \rho_u Y_u dr \right] \\
 S_c &= \frac{dR_f}{dt} - \frac{R_0^3 - R_f^3}{3R_f^2 \rho_u} \frac{d\rho_u}{dt} - \frac{1}{R_f^2 \rho_u} \frac{d}{dt} \left[ \int_{R_b}^{R_u} r^2 \rho Y_u dr \right] \\
 S_c &= \underbrace{\frac{dR_f}{dt} - \frac{R_0^3 - R_f^3}{3R_f^2} \frac{1}{\gamma_u P} \frac{dP}{dt}}_{\text{Mitcheson}} - \underbrace{\frac{1}{R_f^2 \rho_u} \frac{d}{dt} \left[ \int_{R_b}^{R_u} r^2 \rho Y_u dr \right]}_{\text{Add. term}}
 \end{aligned} \tag{IV.15}$$

$$\boxed{S_c = \underbrace{\frac{dR_f}{dt} - \frac{R_0^3 - R_f^3}{3R_f^2} \frac{1}{\gamma_u P} \frac{dP}{dt}}_{\text{Mitcheson}} - \underbrace{\frac{1}{R_f^2 \rho_u} \frac{d}{dt} \left[ \int_{R_b}^{R_u} r^2 \rho Y_u dr \right]}_{\text{Add. term}}} \tag{IV.16}$$

This expression needs a model to assess the evolution of  $\rho Y_u$  within the flame front.

## 2. Burned gas side

A similar procedure can be applied on the burned gas side. In this case  $Y_b^b = 1$  and  $Y_b^u = 0$ .  $S_c$  breaks down into:

$$S_c = \frac{1}{R_f^2 \rho_u} \frac{d}{dt} \left[ \int_0^{R_b} r^2 \rho Y_b dr + \int_{R_b}^{R_u} r^2 \rho Y_b dr + \int_{R_u}^{R_0} r^2 \rho Y_b dr \right] \tag{IV.17}$$

Assuming:

- $R_f \approx R_u \approx R_b$
- On the burned side  $\rho = \rho_b$ , does not vary in space
- $Y_b = Y_b^b = 1$  on the burned side
- There is no burned gas on the fresh side
- isentropic compression assumption ( $P \rho_b^{-\gamma_b} = cte$ )

The equation IV.9 (infinitely thin flame consumption speed from burned gases) is recovered with an additional term:

$$\boxed{S_c = \underbrace{\frac{\rho_b}{\rho_u} \frac{dR_f}{dt} + \frac{\rho_b}{\rho_u} \frac{R_f}{3\gamma_b P} \frac{dP}{dt}}_{\text{IV.9}} + \underbrace{\frac{1}{R_f^2 \rho_u} \frac{d}{dt} \left[ \int_{R_b}^{R_u} r^2 \rho Y_b dr \right]}_{\text{Add. term}}} \tag{IV.18}$$

This expression needs a model to assess the evolution of  $\rho Y_b$  within the flame front.

Finally, the exploration of consumption speed in a finite flame thickness state implies to determine the evolution of  $\rho Y_b$  or  $\rho Y_u$ , respectively considering the burned and fresh gas side. In the next section, two models are considered.

### IV.2.1 Models for consumption speed

In this part, we propose to use different approaches to estimate this consumption speed based on the estimation of the profile of  $\rho Y_k$  in the flame brush. These models illustrate the importance of investigating finite flame thickness.

#### 1. Bradley's Model [28]

Starting from the definition of consumption speed  $S_c$  (IV.3):

$$S_c = \frac{1}{R_f^2 \rho_u [Y_k^b - Y_k^u]} \frac{d}{dt} \int_0^{R_0} r^2 \rho Y_k dr$$

$\rho Y_k$  being unknown, we assume a linear evolution between fresh and burned gases – Fig. IV.3. The expression of  $\rho Y_k$  can be expressed as:

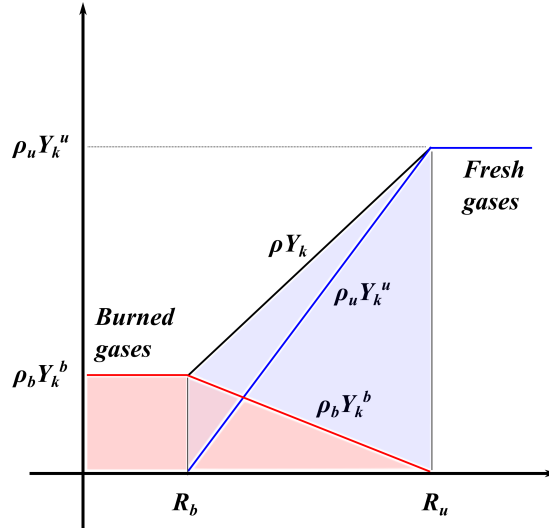


Figure IV.3: Evolution of the quantity  $\rho Y_k$  assuming a linear variation within the flame thickness.

$$\rho Y_k = \rho_u Y_k^u \left( \frac{\rho_b - \rho}{\rho_b - \rho_u} \right) + \rho_b Y_k^b \left( \frac{\rho - \rho_u}{\rho_b - \rho_u} \right) \quad (\text{IV.19})$$

Considering the products' side, the equation IV.19 can be simplified, assuming  $Y_b^u = 0$ ,

$Y_b^b = 1$ :

$$\boxed{S_c = \frac{1}{R_f^2 \rho_u} \frac{d}{dt} \left[ \int_0^{R_u} r^2 \rho_b Y_b dr \right]} \quad (\text{IV.20})$$

Concurrently, it is possible to derive the mass variation of unburned gases expressed as Eq. IV.12 linked to the displacement speed. A reminder of this equation is given below:

$$S_d = \frac{d}{dt} \left[ \int_0^{R_f} 4\pi r^2 \rho dr \right] \quad (\text{IV.21})$$

Using the same model of linear variation of the density thought the flame front:

$$\rho = \rho_u \left( \frac{\rho_b - \rho}{\rho_b - \rho_u} \right) + \rho_b \left( \frac{\rho - \rho_u}{\rho_b - \rho_u} \right) \quad (\text{IV.22})$$

one can obtain:

$$S_d = \frac{1}{R_f^2 \rho_u} \frac{d}{dt} \left[ \int_0^{R_u} r^2 \rho_u \left( \frac{\rho_b - \rho}{\rho_b - \rho_u} \right) + \int_0^{R_u} r^2 \rho_b \left( \frac{\rho - \rho_u}{\rho_b - \rho_u} \right) dr \right] \quad (\text{IV.23})$$

$$S_d = \underbrace{\frac{1}{R_f^2 \rho_u} \frac{d}{dt} \left[ \int_0^{R_u} r^2 \rho_u \left( \frac{\rho_b - \rho}{\rho_b - \rho_u} \right) \right]}_1 + \underbrace{\frac{1}{R_f^2 \rho_u} \frac{d}{dt} \left[ \int_0^{R_u} r^2 \rho_b \left( \frac{\rho - \rho_u}{\rho_b - \rho_u} \right) dr \right]}_2 \quad (\text{IV.24})$$

Term 1 corresponds to the rate of entrainment by the flame front of gases that remain unburned. Term 2 is the rate of appearance of completely burned gases behind the flame front,  $S_c$  from Eq. IV.20. Developing the second term yields:

$$S_c = \frac{\rho_b}{\rho_b - \rho_u} \frac{1}{R_f^2 \rho_u} \frac{d}{dt} \left[ \int_0^{R_u} r^2 \rho dr - \rho_u \int_0^{R_u} r^2 dr \right] \quad (\text{IV.25})$$

Combining and developing this expression with Eq. IV.21 yields:

$$\boxed{S_c = \frac{\rho_b}{\rho_b - \rho_u} (S_d - S_f)} \quad (\text{IV.26})$$

This expression will be referred to as the *Bradley's model*. Assuming a linear variation of the term  $\rho Y_k$  within the flame front, consumption speed is estimated by the measuring both the displacement speed  $S_d$  and the propagation speed  $S_f$ .

## 2. Poinot's Model [71, 26]

This model was introduced by Poinot and Veynante [71]. They implicitly assumed that the value of burned gas density does not vary with  $R$  (from 0 to  $R_b$ ) or with time, and

is equal to the burned gas density at equilibrium  $\rho_b^{eq}$ . Starting from Eq. IV.17 that is expressed below,

$$S_c = \frac{1}{R_f^2 \rho_u} \frac{d}{dt} \left[ \int_0^{R_b} r^2 \rho Y_b dr + \int_{R_b}^{R_u} r^2 \rho Y_b dr + \int_{R_u}^{R_0} r^2 \rho Y_b dr \right] \quad (\text{IV.27})$$

Assuming that within the flame's thickness, burned and fresh gases are present in equal proportions, so that  $\rho Y_b = \frac{1}{2} \rho_b$ , the equation above yields:

$$\begin{aligned} S_c &= \frac{1}{R_f^2 \rho_u} \frac{d}{dt} \left[ \int_0^{R_b} r^2 \rho Y_b dr + \int_{R_b}^{R_u} r^2 \rho Y_b dr \right] \\ S_c &= \frac{\rho_b}{\rho_u} \frac{dR_f}{dt} + \frac{1}{R_u^2 \rho_u} \frac{d}{dt} \left[ \int_{R_b}^{R_u} r^2 \frac{\rho_b}{2} dr \right] \end{aligned} \quad (\text{IV.28})$$

Integrating the second RHS term of Eq. IV.28 between  $R_b$  and  $R_u$  where  $R_u = R_b + \delta$  yields:

$$\begin{aligned} S_c &= \frac{\rho_b}{\rho_u} \frac{dR_f}{dt} + \frac{\rho_b}{3R_u^2 \rho_u} \frac{1}{2} \frac{d}{dt} [R^3]_{R_b}^{R_b+\delta} \\ S_c &= \frac{\rho_b}{\rho_u} \frac{dR_f}{dt} + \frac{\rho_b}{3R_u^2 \rho_u} \frac{1}{2} \frac{d}{dt} [3R_b^2 \delta + 3R_b \delta^2 + \delta^3] \end{aligned} \quad (\text{IV.29})$$

Neglecting  $\delta$ 's orders upper than 1 and assuming a constant flame thickness, expression Eq. IV.29 yields:

$$\boxed{S_c = \frac{\rho_b}{\rho_u} \frac{dR_f}{dt} \left[ 1 + \frac{\delta}{R_b} \right]} \quad (\text{IV.30})$$

This model will later be referred to as *Poinsot 2011* model from *Theoretical and Numerical Combustion, third edition 2011*, [71]. Another model can be found in the first edition book (2001), [26]. The development starts from the generalized consumption speed definition IV.3 and assumes that  $\rho Y_k = \frac{1}{2} \frac{\rho_b + \rho_u}{2}$ . The density is assumed to be an average between burned and fresh gases and the mass fraction  $Y_k$  is supposed to be constant and equal to  $\frac{1}{2}$ . The expression is given below and will be referred later as *Poinsot 2001* model.

$$\boxed{S_c = \frac{\rho_b}{\rho_u} \frac{dR_f}{dt} \left[ 1 + \frac{\delta}{2R_b} \left( 1 + \frac{\rho_u}{\rho_b} \right) \right]} \quad (\text{IV.31})$$

This model assumes a constant flame thickness during flame propagation. This is probably true for fuel/air mixtures with Lewis numbers close to unity, but it can change significantly for non-unity Lewis numbers [74].

The graph below summarizes all the expressions of consumption speed, and contains the informations and assumptions involved, Tab. IV.4:

# Consumption Speed

$$S_c = \frac{1}{R_f^2 \rho_u [Y_k^b - Y_k^u]} \frac{d}{dt} \int_{-\infty}^{+\infty} r^2 \rho Y_k dr$$

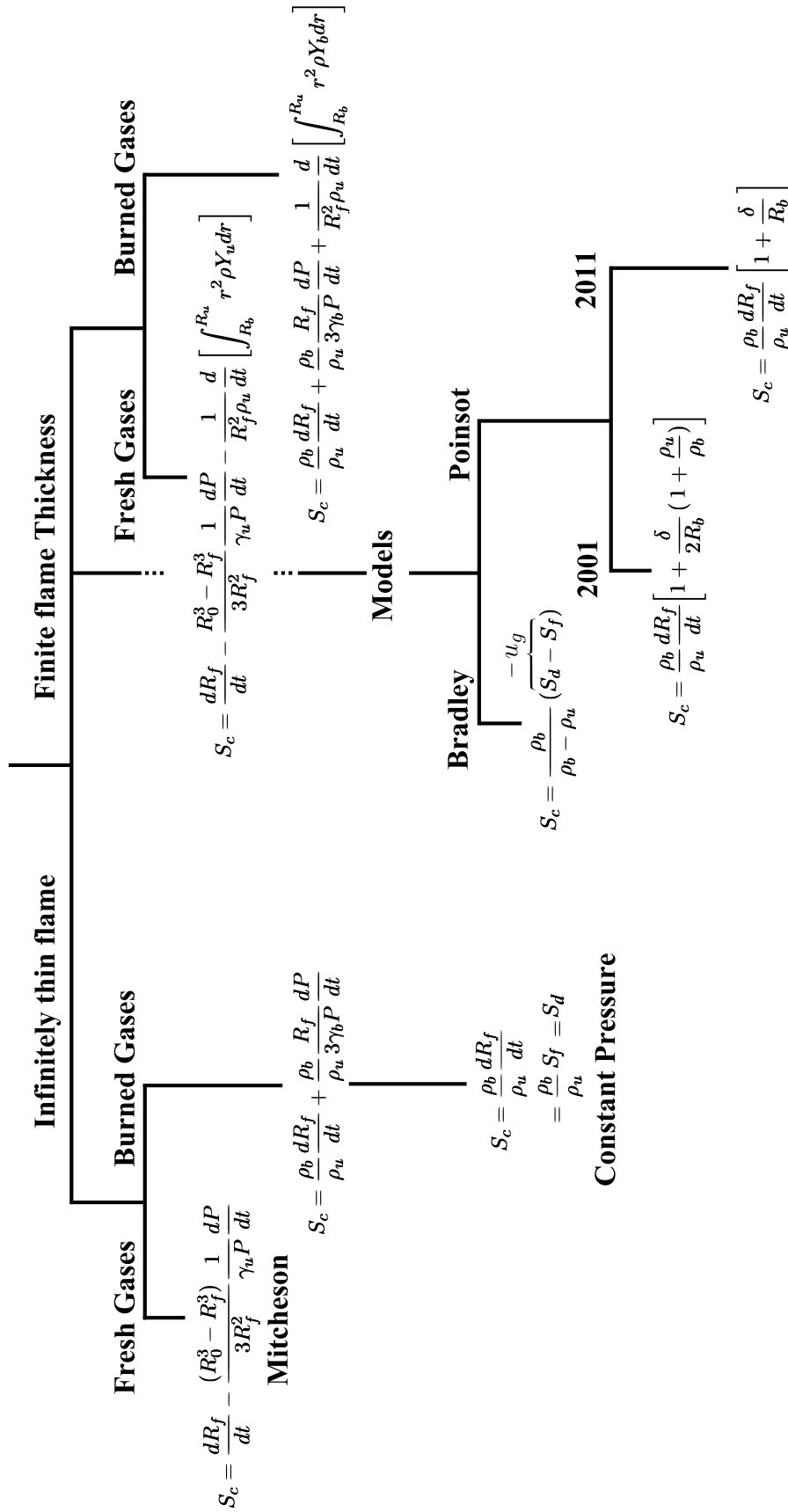


Figure IV.4: Consumption speed formulations.



Finally, the calculation of the consumption speed  $S_c$  can be estimated under several assumptions through a combination of:

- Displacement speed estimated at the fresh gas isothermal  $T = T_u$ . In this case, displacement speed  $S_{d,T=T_u}$  is the burning velocity  $u_n$ .

$$S_{d,T=T_u} = u_n = S_f - u_{g,T=T_u} \quad (\text{IV.32})$$

$$u_n = S_f - u_g$$

- Propagation speed

$$S_f = \frac{dR_f}{dt} \approx \frac{dR_u}{dt} \approx \frac{dR_b}{dt} \quad (\text{IV.33})$$

### IV.3 Concluding Remarks

In this chapter, a theoretical review details expressions and models for burning velocity in the case of a spherically expanding flame. For both infinitely thin flame and finite flame thickness approaches, the expressions of consumption speed associated with fresh or burned gas sides are developed. It is worth noting that for the finite flame thickness, the expression of the density through the flame is necessary. Two models have been presented. Bradley's model assumes a linear variation of the density (from unburned at  $\rho_u$  to burned side at  $\rho_b$ ) through the flame front. Poinot's model uses an average and constant value in the flame front.



## Chapter V

# Conclusion of the Theoretical Part

Determining *laminar burning velocity* is a considerable challenge. Because of the variety of approaches, different definitions of *laminar burning velocity* must be established. Here is a summary of these definitions in the case of spherically expanding flames.

### Laminar burning velocity:

- In the laboratory's reference frame

Propagation speed is measured using the time-derivative evolution of the flame's radius:

$$S_f = \frac{dR_f}{dt} \approx \frac{dR_u}{dt} \approx \frac{dR_b}{dt}.$$

Flame propagation reflects the velocity at which the burned gases expand and laminar burning velocity is extracted through the mass conservation equation available only at zero stretch.

$$u_s^0 = \frac{\rho_b^{eq}}{\rho_u} \lim_{k \rightarrow 0} S_f \quad (\text{V.1})$$

- In the flame's reference frame

The observer is positioned on the flame front. It is possible to evaluate the velocity at which fresh gases go through the isothermal  $T = T_u$ :  $u_g$ . It delimitates the position at which the flame starts disturbing the fresh flow. By combining velocities, we can write, for the isothermal at  $T = T_u$ :

$$u_n = S_f - u_g u_n^0 = \lim_{k \rightarrow 0} u_n \quad (\text{V.2})$$

- At a chemical scale

The rate at which reactants are consumed (or products appear) is investigated – consumption speed  $S_c$ . These expressions are fully described in Chapter IV. Next, we will focus on four expressions of burning velocity:

1. Mitcheson's Formulation

$$S_c = \frac{dR_f}{dt} - \frac{R_0^3 - R_f^3}{3R_f^2} \frac{1}{\gamma_u P} \frac{dP}{dt} \quad (\text{V.3})$$

2. Poinso's Model 2001

$$S_c = \frac{\rho_b^{eq}}{\rho_u} \frac{dR_b}{dt} \left[ 1 + \frac{\delta_l}{2R_b} \left( 1 + \frac{\rho_u}{\rho_b^{eq}} \right) \right] \quad (\text{V.4})$$

3. Poinso's Model 2011

$$S_c = \left( 1 + \frac{\delta_l}{R_b} \right) \frac{\rho_b^{eq}}{\rho_u} \frac{dR_b}{dt} \quad (\text{V.5})$$

4. Bradley's Model

$$S_c = \frac{\rho_b^{eq}}{\rho_b^{eq} - \rho_u} (u_n - S_f) \quad (\text{V.6})$$

The assumptions underlying these expressions – except for V.2 – are more or less restrictive. We can easily classify these formulations from the most to the least restrictive, as follows (Fig. V.1): It clearly appears that the displacement speed formulation is free of assumption. However, the fresh gases profile is needed.

Next, we will focus on the way to determine these different velocities experimentally. The experimental setup will be described and the new post-processing tools developed for fresh gas velocity measurement,  $u_g$ , will be presented.

We will first validate the experimental facility and post-processing tools on methane, isooctane and ethanol using the two most accurate formulations.

Then, we will extract consumption speed formulations experimentally, focusing on pressure signal determination and derivation. Bradley's and Poinso's models will also be discussed.

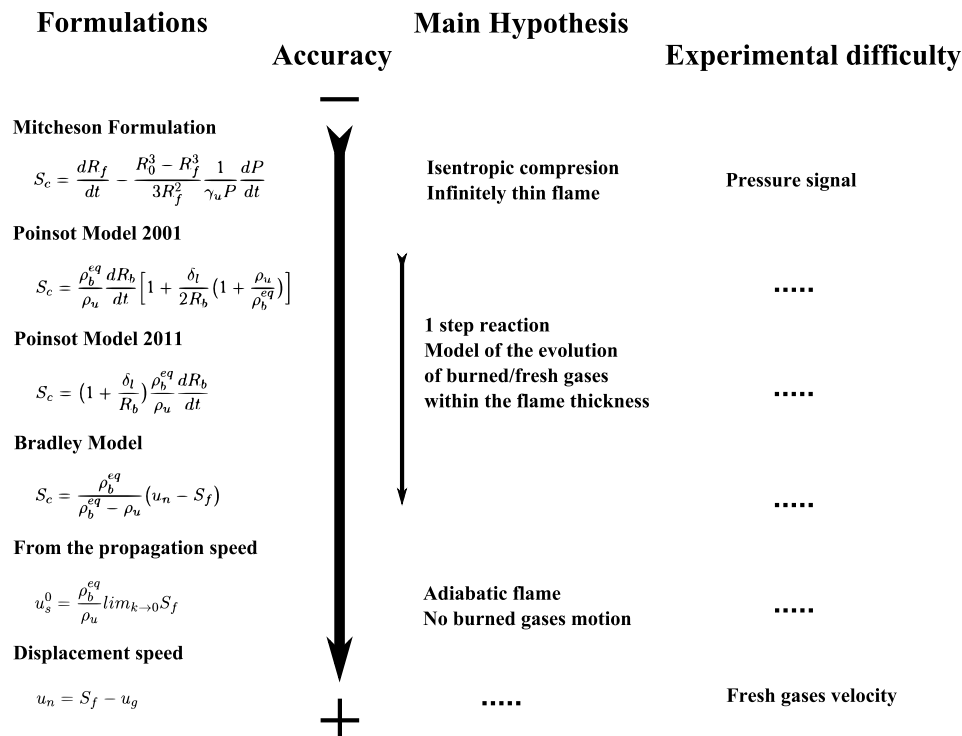


Figure V.1: Overview of the burning velocities formulations.

Thirdly, flame's response to stretch will be investigated by comparing velocity formulations for fuels of various Lewis numbers.

Finally, the case of blended ethanol/isooctane will be studied. The pressure dependence of these blended fuels will be investigated using the displacement speed approach.



## Part II

# Experimental setup and results





## Chapter VI

# Experimental design and post-processing

The work presented in this chapter corresponds to the article *Measurement of laminar burning velocity and Markstein length relative to fresh gases using a new-post processing procedure: Application to laminar spherical flames for methane, ethanol and isooctane/air mixtures*, published in Combustion and Flame [21].

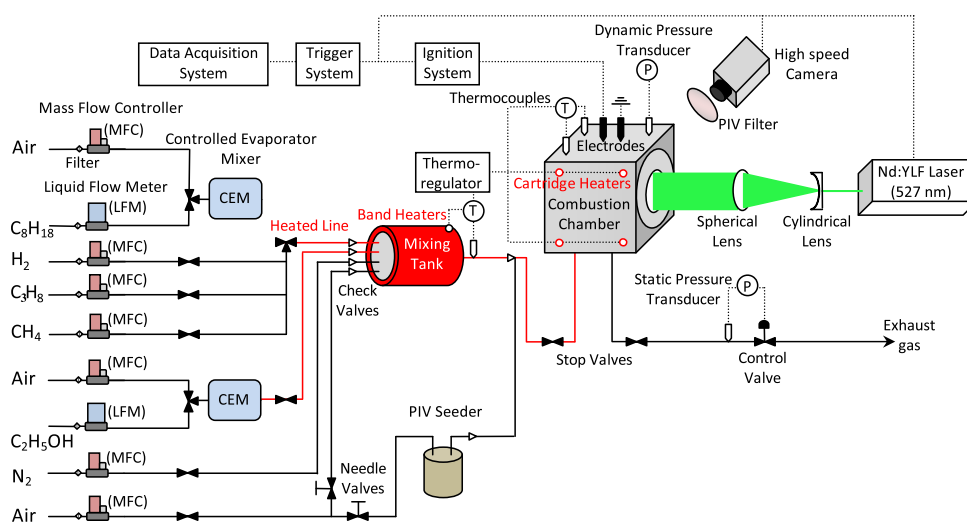
The aim of this part is to provide experimental measurements of the flame speed ( $\frac{dR}{dt}$ ) and the displacement speed, extracted at the fresh gases isothermal  $T = T_u$  ( $u_n = \frac{dR}{dt} - u_{g,T=T_u}$ ) from the spherical flame configuration. To achieve this objective, a new combustion chamber has been designed and fully equipped with sensors, controllers and tomographic optical diagnostic chain. New post-processing tools have also been developed in order to achieve the measurement of the fresh gases velocity profile  $u_g$  ahead of the flame front. This chapter is divided into two parts and follows the previous description.

## VI.1 Experimental Design

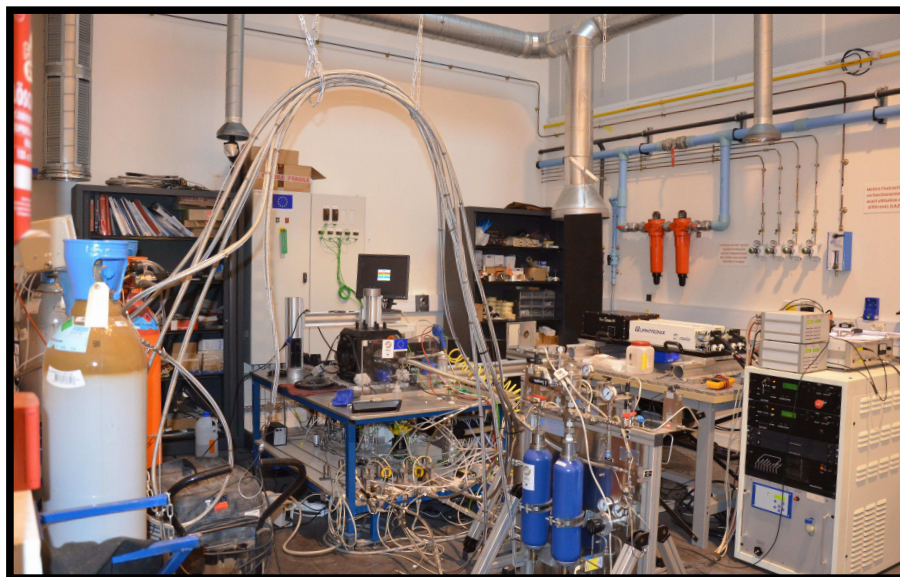
### VI.1.1 High pressure and temperature facility

The experimental facility enables us to reach thermodynamic conditions close to those encountered in internal combustion engines; the maximum operating pressure temperature are limited to respectively 2 MPa and 573 K. The radius of the inner chamber is 85 mm ( $\approx$  2.6 liters). Two types of fuels – gaseous or liquid – can be used in this experimental device. Fuels that are gaseous under ambient conditions ( $CH_4$ ,  $C_3H_8$  and  $H_2$ ) are charged directly from bottles through mass controllers. Liquid fuels are first vaporized in a heated chamber by using a *Controlled Evaporator Mixer (CEM)* (Bronkhorst) and then charged through heated lines into the vessel. During the experiments, the liquid fuel vaporization system showed no coking inside the vaporization chamber, no re-condensation and no flow-rate oscillation. To obtain a homogeneous mixture, all gases are premixed in a tank before injection into the combustion chamber and the equivalence ratio of the mixture is measured and regulated by Coriolis or thermal mass flow controllers connected to a computer. An electrical heating system, which is monitored by a proportional integral derivative (PID) controller, regulates temperatures in the mixing tank and the combustion chamber. The temperature is controlled inside the chamber by two thermocouples that ensure uniformity of the temperature field. Compressed fuel/air mixture is supplied continuously from the bottom of the combustion chamber. The pressure level, which is monitored in the vessel with a piezoelectric pressure sensor, is kept constant by adjusting the control valve. Once both the composition of the fuel mixture and the thermodynamic conditions are achieved and unchanging, two stop valves are used to close the combustion chamber. Ignition takes place one minute later to avoid any flow perturbation during the flame propagation. The combustible mixture is spark-ignited at the center of this chamber by two stainless steel electrodes linked to a capacitive discharge ignition system using minimum spark energies to avoid ignition disturbances. The electrode diameter is 0.5 mm and the gap between electrodes is kept constant to 1.5 mm. During the combustion process, the evolution of the chamber pressure is acquired by a dynamic pressure transducer (Kistler). Once combustion is complete, the chamber

is ventilated and purged with nitrogen to remove condensed water vapor or combustion products in order to keep a constant temperature from one try to another. Fig. VI.1 illustrates the configuration scheme of the experimental setup. Moreover, Fig. VI.2 provides some pictures of the corresponding elements: Chamber, Evaporator system and feeding system.

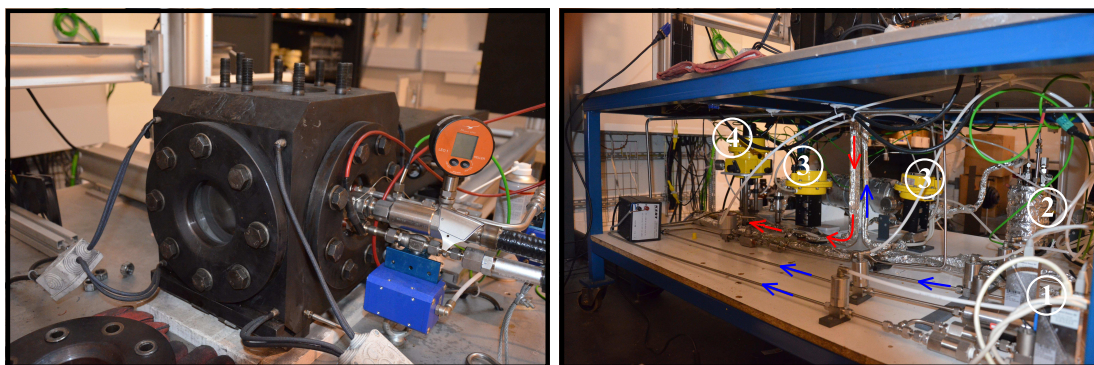


(a) General Scheme



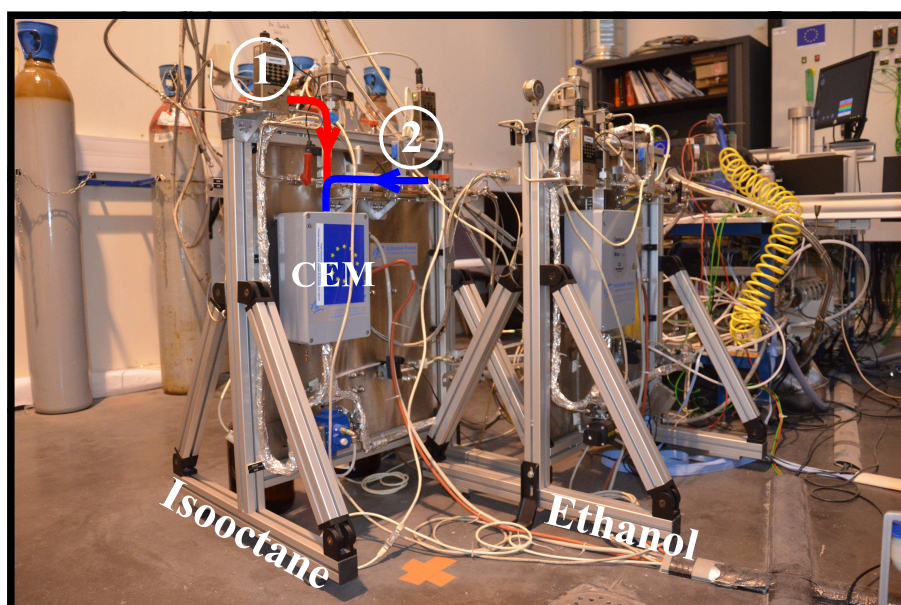
(b) General View

Figure VI.1: Experimental apparatus.



(a) Combustion Chamber

(b) Feeding System, 1: Mass Flow controllers, 2: Seeding system, 3: Insulation valves, 4: Pressurization valve



(c) Evaporator System, 1: Fuel Mass Flow controller, 2: Air dilution Supply, 3: Evaporating cell

Figure VI.2: Experimental design pictures.

### VI.1.2 Optical diagnostics

The chamber is equipped with three transparent windows for optical diagnostics. Flame speed and fresh gas velocity are obtained from high-speed laser tomography recordings. A double cavity Nd:YLF laser (Darwin Dual, Quantronix), delivering pulses of 6 mJ at 527 nm and at 5 kHz, is used to illuminate seeding particles. The laser sheet is created by associating one cylindrical lens of - 13 mm focal length and one spherical lens of 254 mm focal length (Fig. VI.3. A high-speed



camera (Photron Fastcam SA1.1) records an 8-bit image couple of  $1024 \times 1024$  *pixels*<sup>2</sup> at a frequency of 5 kHz. The camera, which is mounted with a 105 mm macro-Nikon lens (f/2.8), has a field of view of  $50.2 \times 50.2$  mm<sup>2</sup>, which leads to a magnification ratio of 0.049 mm/pixels. An interferential pass-band filter ( $527 \pm 10$  nm) is used to remove the flame chemiluminescence. To capture the tomography images, the flow is seeded with silicone oil droplets (Rhodorsil),

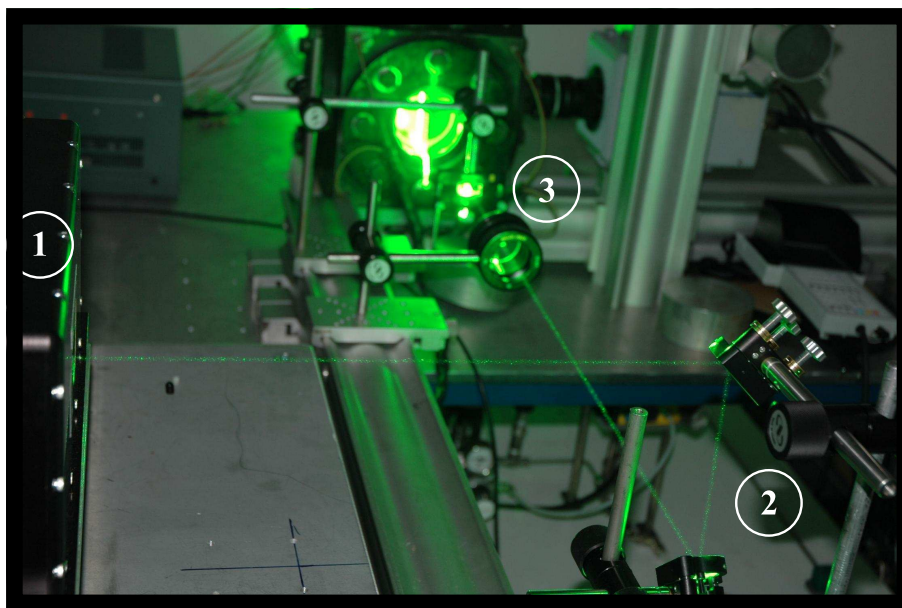


Figure VI.3: Optical Setup, 1: Laser source, 2: Periscope, 3: Sheet generator (cylindrical/spherical lenses).

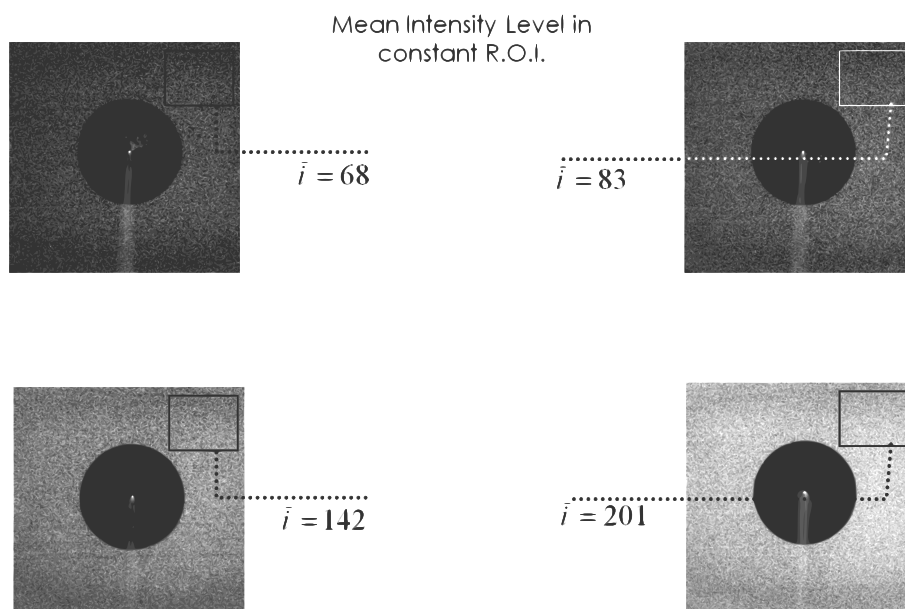
which vaporize at an isotherm of about 580 K. This boiling point temperature is high enough for the seeding droplets to persist into the preheat zone and can be used to capture the maximum velocity point upstream of the flame. Seeding particles do not survive in the post flame zone; nevertheless this type of silicone fluid does not have any observable effect on the flame. Several tests with different seeding particle concentrations (in terms on 8bits signal intensity) have shown that the effect of particle concentration on the measured flame speed is quite insignificant on both unstretched flame speeds and Markstein lengths. The differences are in fact close to the reproducibility errors from one to another experiment (Tab. VI.1). This finding is illustrated in Fig. VI.4, where it is shown that the flame propagation does not depend on the particle concentration. As a result, a concentration of particles allowing a good contrast is retained

(intensity  $\approx 140$ ).

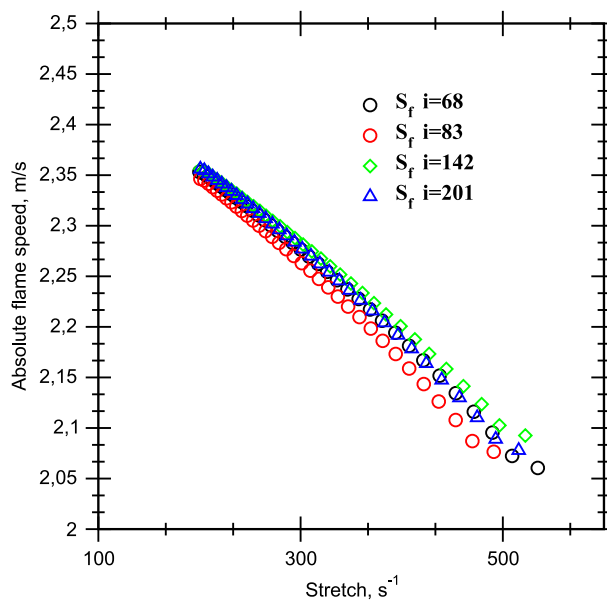
Examples from an experiment are shown in Fig. VI.5. The sequence shows a methane/air flame at an initial temperature of 353 K at the stoichiometry. In this experiment, the camera controls the synchronization of the system. Fig. VI.7 represents the synchronization procedure.

Intensity	$S_f^0/S_{f,mean}^0$	$L_b/L_{b,mean}$	non-linear method
68	1.002		1.01
83	1		1.02
142	1.003		0.98
201	0.995		0.99

Table VI.1: Extracted values of unstretched propagation speed  $S_f^0$  and burned gas Markstein length  $L_b$  for different seeding densities.



(a) Experimental procedure for seeding effect



(b) Results on the absolute flame speed  $S_f$

Figure VI.4: Seeding Effect.

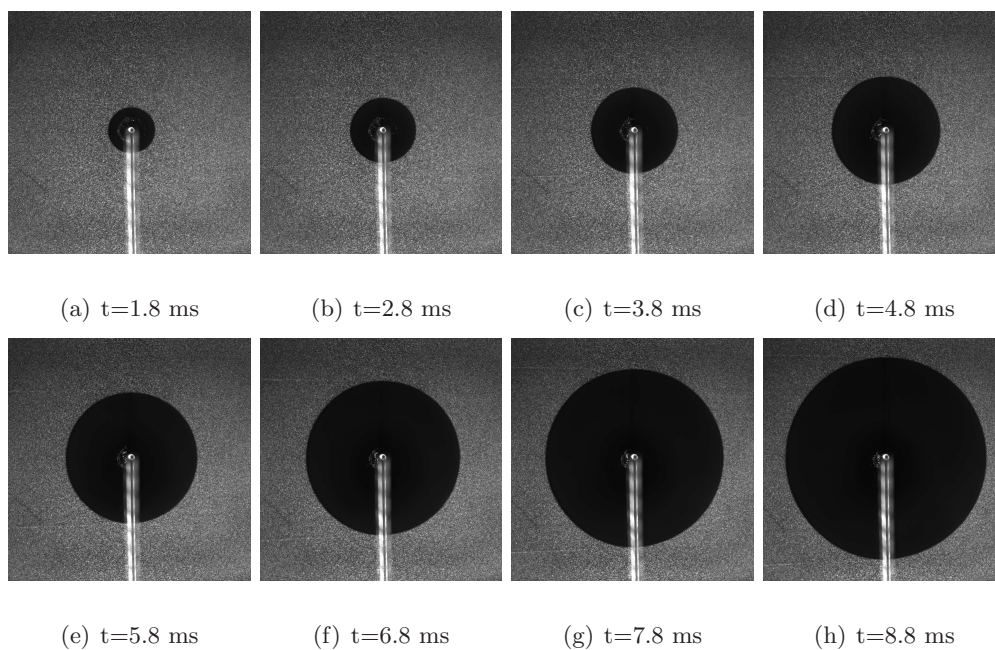


Figure VI.5: Visualization of a propagation sequence of a stoichiometric methane/air flame at  $P=0.1$  MPa,  $T=298$  K.

Figure VI.6: Animation of a propagative stoichiometric methane/air flame at  $P=0.1$  MPa,  $T=298$  K, *In pdf version, please press play button in the control bar above.*



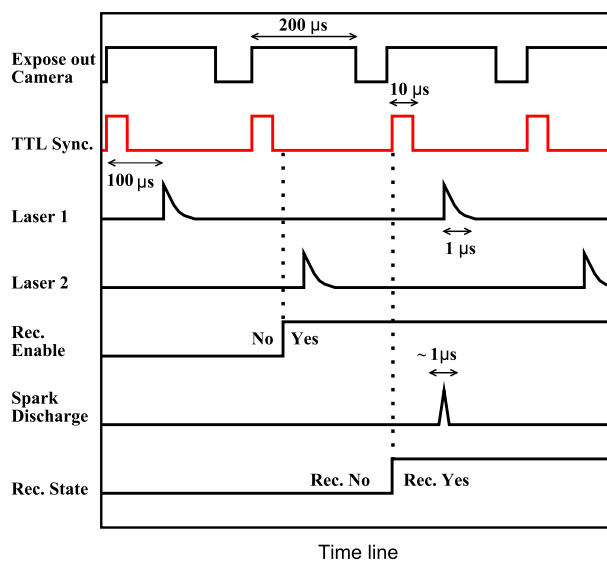


Figure VI.7: Synchronization diagram.

## VI.2 Post processing algorithm

It has been seen in the previous part that for determining the burning velocities using the Eq. V.2, two quantities must be known: the flame propagation speed and the fresh gas velocity at the entrance of the flame front. The major difficulty of this technique resides in measuring the fresh gas velocity at the entrance of the preheat zone of the flame front. An accurate measurement of local fresh gas velocity must be obtained in a zone with a typical length of 1 mm (Fig. VI.8). Therefore, the reliability of this measurement depends on the flame front detection (which must be achieved with sub-pixel accuracy) and on the capacity of the technique to determine the fresh gas velocity. To accomplish this, a new tool for tomographic image post-processing has been developed, which will be presented in the following section.

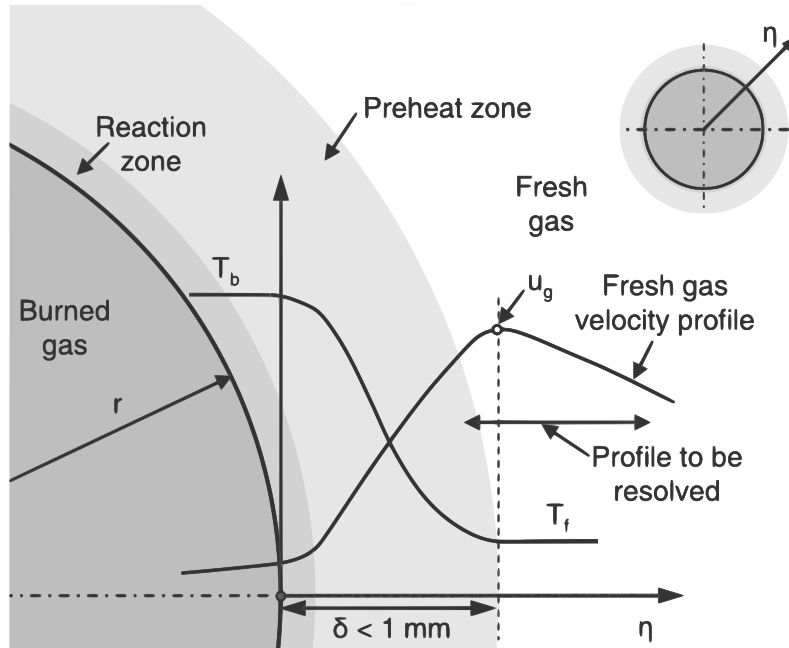


Figure VI.8: Representation of the fresh gas velocity profile near the flame front, from [75].

### VI.2.1 Absolute flame speed estimation

The laser tomography technique provides a visualization of the flame front propagation. The fresh gas mixture is seeded with silicon oil particles, which evaporate at the entrance of the flame front ( $T_{evaporation} = 580$  K). The flame surface is obtained by differentiation of the dark

and bright areas on the flame images, representing burned and unburned states, respectively. To determine the flame speed, the contours of tomographic images, which are captured at several stages of flame development, are extracted using post-processing functions. On each spherical flame image, a single contiguous region representing burned gases is isolated with sub pixel resolution and its contour is then accurately detected using an algorithm based on the method of Suzuki and Abe [76]. The detected raw flame boundaries are smoothed by a low pass filter to remove noise from the digitization steps and a least square algorithm [77] calculates the circle best fit to the raw contour and the corresponding flame radius. The flame speed is then calculated from the temporal evolution of the flame front, referred to as  $S_f = \frac{dR_f}{dt}$  where  $R$  is the flame radius. Flame speed generally uses numerical differentiation of flame radius for calculation. Flame radius used to be fitted with polynomial expression. However, this method leads to a well-known problem because polynomial fits directly impose the derivative function. In order to reduce the influence of non-physical parameter, integrating III.6 for the flame speed, yields, as demonstrated in [78]:

$$t = A \left[ E_1(\ln \epsilon^2) - \frac{1}{\epsilon^2 \ln \epsilon} \right] + C \quad (\text{VI.1})$$

where  $A = \frac{2L_b}{S_f^0}$ ,  $R_f = -\frac{2L_b}{\epsilon \ln \epsilon}$ ,  $E_1(x) = \int_x^\infty \frac{e^{-z}}{z} dz$  and  $\epsilon \in [1/e, 1]$  for  $L_b > 0$  and  $\epsilon \in [1, \infty]$  for  $L_b < 0$ .

As said in [78], Eq. VI.1 can be used for constrained non-linear least-square regression to determine constants  $A$ ,  $L_b$  and  $C$ , and then the unstretched flame speed  $S_f = 2L_b/A$ . However, Halter *et al.* [59] pointed out that the convergence of this equation is highly dependent on the initial conditions. They propose to first minimize the sum:

$$\sum_{i=1}^n \left[ \left( \frac{S_f}{S_f^0} \right)^2 \ln \left( \frac{S_f}{S_f^0} \right)^2 + \frac{2L_b \kappa}{S_f^0} \right] \quad (\text{VI.2})$$

where  $n$  is the number of raw radius data, and  $S_f$  is evaluated with classical derivation process, and then to use the obtained output as the input of the method proposed by Kelley [78]. They have estimated errors to be less than 2% between the methods. However, classical linear extrapolation can be used III.7, here applied to the propagation speed:

$$S_f = S_f^0 - L_b \kappa \quad (\text{VI.3})$$

Figure VI.9: Animation of flame speed extraction from tomographic images. *In pdf version, please press play button in the control bar above.*

## VI.2.2 Fresh gas velocity measurement

The determination of fresh gas velocity near the preheat zone of the flame front is solved by taking into account the local topology of the flame front. The tomographic images are analyzed with an algorithm using an adaptive interrogation window scheme. Using this technique, the fresh gas velocity is measured locally at the entrance of the flame front. The aim of this present work is to complete the approach of Balusamy *et al.* [75], by proposing a new algorithm that

can take into consideration the overall topology of the flame front, assuming that the flame is homogeneous in the specific case of a laminar spherical expansion. This approach therefore enables us to determine a global value of fresh gas velocity.

This method is applied to flame front contours, which were extracted and filtered with the detection procedure described previously. For two successive tomographic images, the algorithm defines a region of interest (ROI), which fits the flame front contour as depicted in Fig. VI.10. This figure synthesizes the processing algorithm explained below.

In these experiments, the ROI is defined by the angle  $\theta$ , which can be adjusted to fit the spherical flame in its entirety or not, and by its width, which is fixed at 5 mm ( $\approx 100$  pixels between the two white dashed lines in Fig. VI.10). An interrogation window with a typical width of 4 pixels ( $\approx 0.2$  mm) is located within this ROI defined by its length ( $r, \theta$ ): white solid lines in Fig. VI.10. The ROI is transformed into a Cartesian coordinate system using a bilinear interpolation scheme. Unwrapped flames fronts can be seen in section VI.2.2.1. The width of the interrogation window has been minimized to reach the physical size of the particle image, which is close to 4 pixels (length called  $H$  in Fig. VI.10). A wider interrogation window will decrease the spatial resolution of  $u_g$  and thinner interrogation will introduce more erroneous values of  $u_g$ . The length of the interrogation window can be adjusted to achieve the best correlation between both successive tomographic images. Once both interrogation windows are well defined, a matching method based on a two-dimensional normalized cross correlation is used between windows of the two successive ROI. Two steps are necessary to determine the fresh gas velocity value at the entrance of the flame front based on the two successive tomographic images.

- The first stage consists in finding the best correlation between both interrogation windows. This is achieved by shifting the second interrogation window, one pixel at a time, in the direction normal to the flame front. With a fixed position of the first interrogation window, the evolution of the correlation peak intensity can be plotted against the shift of the second interrogation window. This correlogram is constructed with a maximum displacement of 80 pixels ( $\approx 4$  mm) along the normal to the flame front. The intensity of the correlation peak increases up to an optimum displacement (which is calculated using

sub pixel interpolation by a Gaussian five-points fit) and then decreases. This optimum displacement, which is designated by  $\Delta r_k^{opti}$  in Fig. VI.10, corresponds to a maximum correlation. We will use this value to calculate the fresh gas velocity ahead of the flame front.

- To characterize the velocity profile ahead of the flame, the second stage of post processing consists of moving the first interrogation window pixel by pixel in the direction normal to the flame front. For each position (expressed by  $\Delta r_j$ ) of this window, the first step of the template matching procedure is restarted. This procedure thereby associates each position ( $\Delta r_j$ ) of the first interrogation window with an optimum displacement ( $\Delta r_k^{opti}$ ) of the second interrogation window, corresponding to the best correlation for both particle images. The fresh gas velocity along the normal to the flame front,  $u_g^j$ , is then calculated using both these parameters in the relationship Eq. VI.4:

$$u_g^j = \frac{r_{i+1} - r_i}{\Delta t} + \frac{\Delta r_k^{opti} - \Delta r_j}{\Delta t} = S_f + \frac{\Delta r_k^{opti} - \Delta r_j}{\Delta t} \quad (\text{VI.4})$$

where  $r_i$  is the flame radius of flame  $i$ ,  $\Delta t$  corresponds to the time between two successive images,  $S_f$  is the flame speed,  $\Delta r_k^{opti}$  is the optimum displacement of the second interrogation window and  $\Delta r_j$  is the displacement of the first interrogation window.

This relationship allows us to describe the movement of particles (*i.e.* fresh gases) pushed by the flame front expansion. Using this procedure, the fresh gas velocity profile along the normal to the flame front can be recorded from a distance of 150  $\mu\text{m}$  ( $\approx 3$  pixels) up to 4 mm ( $\approx 80$  pixels). An example of an instantaneous fresh gas velocity profile calculated from methane/air flame images is presented in Fig. VI.10. In the case of spherically expanding flames, heat diffusion in the preheat zone influences the fresh gas velocity,  $u_g$ , which has a maximal value at the entrance of the flame front (expressed by  $u_g$ ) and then decreases ahead of the flame front. This decrease occurs due to temperature and gas density variations through the flame front (Groot and De Goey [79]). In Fig. VI.10, the maximum fresh gas velocity,  $u_g$ , is obtained by fitting the velocity profile by a 10th order polynomial fit. For a particle image couple, post processed with the new algorithm, the

maximum of the fresh gas velocity profile ( $u_g$ ) is located around 7–8 pixels ( $\approx 350\text{-}400 \mu\text{m}$ ) ahead of the evaporation isotherm of the particles. For each image pair, the maximal value of the fresh gas velocity ( $u_g$ ) at the entrance of the flame front is calculated and laminar burning velocity is extracted using Eq. V.2:  $u_n = S_f - u_g$ . Laminar burning velocity is then plotted as a function of the flame stretch rate; the unstretched burning velocity and the Markstein length relative to fresh gases are extrapolated from linear or non-linear formulations, Eq. III.7 and Eq. III.6 respectively.

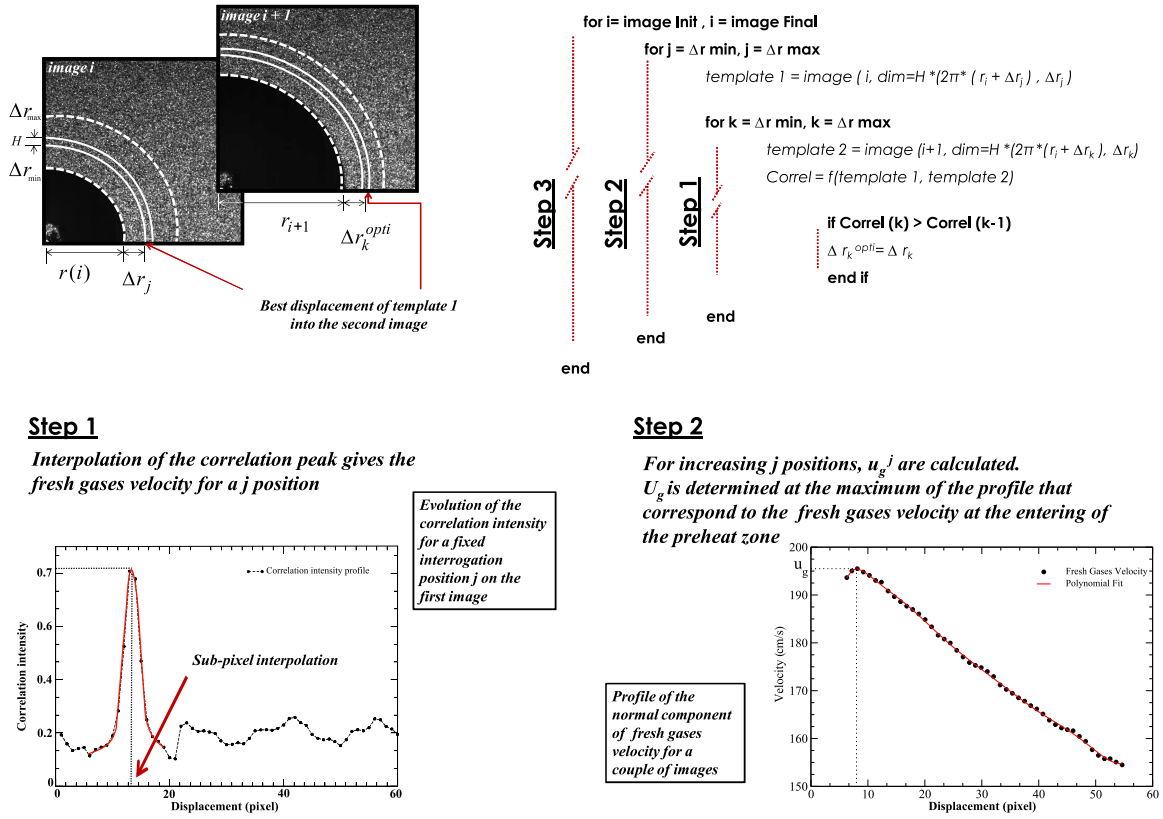


Figure VI.10: Synthesis of the algorithm for fresh gas velocity profile determination.

### VI.2.2.1 Test phase

Tests are carried out to validate the algorithm described above. In order to demonstrate or estimate that errors induced by the post-processing tool are non significant, various test cases are investigated.

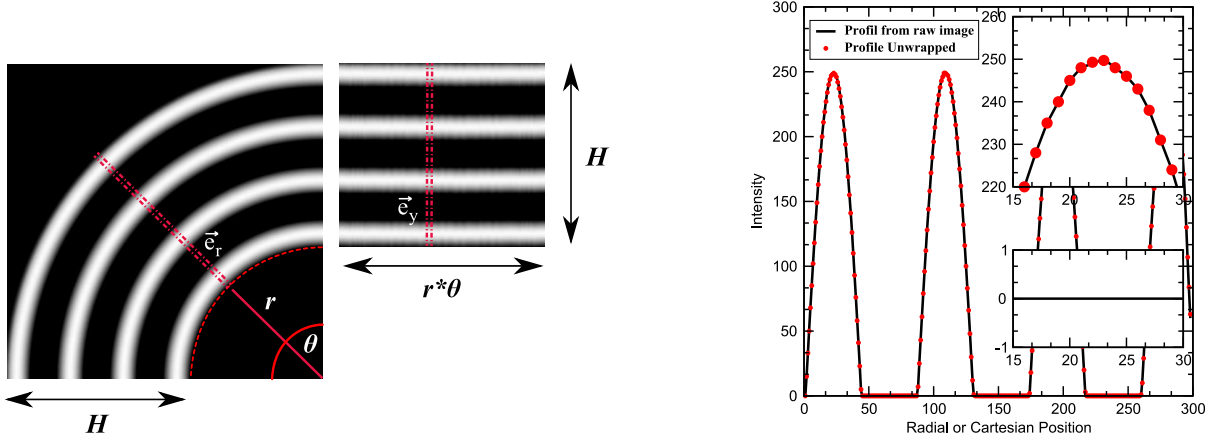
1. **Test 1:** A cylindrical  $(r, \theta)$  mesh made of concentric circles, which intensity is a sinus

Figure VI.11: Animation of fresh gas velocity extraction from tomographic images using direct cylindrical correlation. *In pdf version, please press play button in the control bar above.*

function of the radius, is unwrapped to estimate errors caused by cylindrical to Cartesian deformation. Fig. VI.12(a) (*left*) shows a quarter of the synthetic image. The image center is imposed at point (512,512). Concentric white circles start from radius  $r > R_0$  and follow an intensity (I) function as:  $I = \sin(d/10)$  if  $\sin(x) > 0$ , 0 instead; where d is the distance of (X,Y) position to the center. The corresponding unwrapped image is shown on Fig. VI.12(a) (*right*). The sinus function can be recovered by extracting two profiles on each image. On the first image (Fig. VI.12(a) (*left*)) the profile is extracted along  $\vec{e}_r$  direction and respectively along  $\vec{e}_y$  on the second image (Fig. VI.12(a) (*right*)). Profiles



are plotted in Fig. VI.12(b) It can be seen that no axial ( $\vec{e}_y$ ) displacement is imposed by



(a) Synthetic Cylindrical image and Cartesian unwrapped images

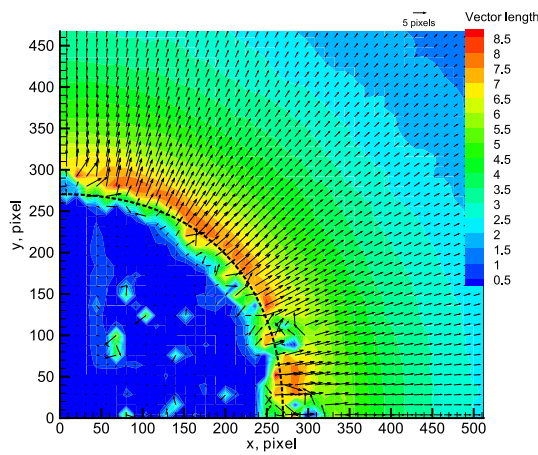
(b) Synthetic cylindrical and unwrapped profiles. Difference between the two profiles

Figure VI.12: Synthetic images and corresponding profiles.

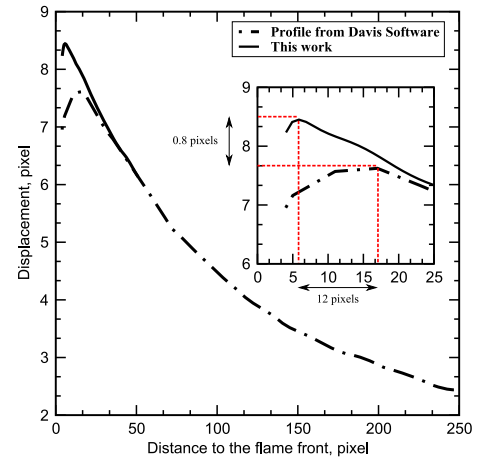
the calculation algorithm. The profiles are well superposed and peaks of intensity are also very faithfully returned. In this case, we observe no influence of the processing unwrapping tool on the determination of particle displacement.

- Test 2:** The developed post-processing tool is compared to classical PIV method for  $u_g$  profiled far from the flame front. Fig. VI.13(a) shows the velocity field extracted from LaVision Software (Davis). The calculation is classical cross-correlation with multipass decrease algorithm: two passes  $32 * 32 \rightarrow 16 * 16$  (50% overlap). Close to the flame front, false vectors appear and impede the extraction of a satisfying radial velocity profile. As a result, classical cartesian correlation windows that overlap burned zones – no tomographic signal – and fresh gases – particules Mie diffusion – introduce false displacement calculation. This problem is well known amongst members of the combustion community whose work focuses on resolving the velocity field nearby the flame front; see [80] *et al.* for further informations. In Fig. VI.13(b), comparison between the both velocity profiles is shown (Davis - Present work). In the standard PIV method, the profile is averaged on a quarter of the image along  $\vec{e}_r$ . Close to the flame front, the classical method gives a maximum velocity profile of about 12 *pixels* ( $\approx 1/2$  calculation cell) further from the

flame front and  $0.8 \text{ pixels}$  less (on intensity) than the one calculated in this study. It is important to note that the difference in displacement intensity ( $0.8 \text{ pixel}$ ) generates a velocity loss of about  $18 \text{ cm/s}$  compared to our study. These differences on the maximum position of the velocity profile were expected and corroborates previous results ([80]). Nevertheless, the accurate method (present work) and the classical one match at a distance to the flame front close to a calculation cell ( $\approx 32 \text{ pixel}$ ). This result probes the consistence of the algorithm developed in this work. We are now able to determine accurately velocity profiles both close to, and far from, the flame front.



(a) Displacement field, in pixel, calculated by Davis standard PIV algorithm



(b) Displacement profile from standard algorithm and this work

Figure VI.13: Comparison between standard PIV algorithm and accurate profile from this work.

### VI.3 Concluding Remarks

In this part, experimental methods to measure both flame speed and displacement speed (at  $T = T_u$ ) were investigated. To do so, we developed a specific experimental combustion chamber coupled with a new post-processing tool. These developments made it possible to extract and estimate three burning velocities from different approaches (V.1, V.2 and V.6). Their extrapolation to zero stretch follows the linear – III.7 – or non-linear – III.6 – relation. An example is given below and will be discussed later.

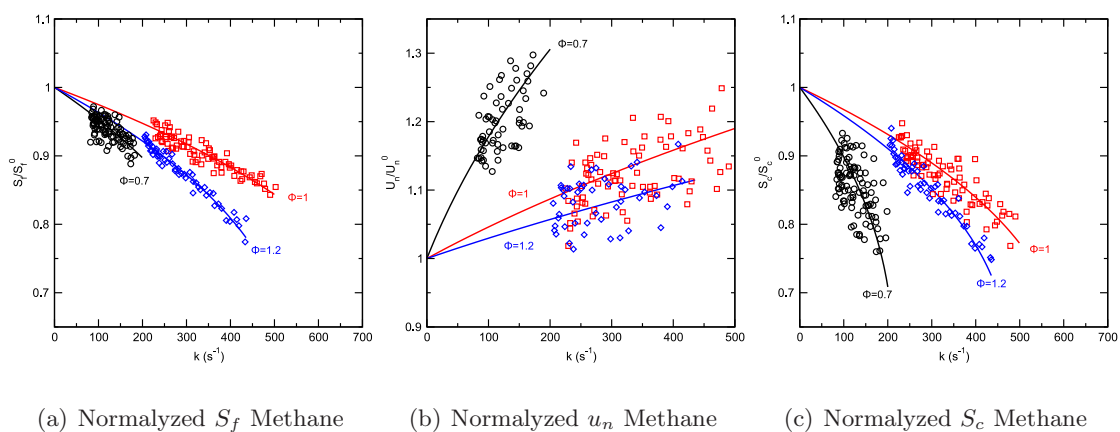


Figure VI.14: Comparison of  $S_f$ ,  $u_n$  and  $S_c$  for a methane/air flame at given equivalence ratios,  $P=0.1$  MPa,  $T=300$  K.



## Chapter VII

# Measurement of the Unstretched Laminar Burning Velocity from the Flame and Displacement Speeds

In this chapter, we report the experimental validation of the technique for three fuels: methane, isoctane and ethanol. This work aims to find the best way to obtain an accurate evaluation of laminar burning velocity by determining the biases involved in the formulations. Biases mostly result from assumptions or hypotheses that are not fully verified. Note that this chapter only reports results for laminar burning velocities. Data concerning Markstein lengths are exposed in [21].

### VII.1 Methane/Air flames

#### VII.1.1 Laminar flame speed measurements and comparison with literature

Laminar flame speed measurements of methane/air flames are carried out for various equivalence ratios at atmospheric pressures and room temperatures (298 K). For each test, around 80 images are taken, covering the duration of flame propagation, free from ignition energy and wall effects. Unstretched flame speed is linearly and nonlinearly extrapolated. The non-linear extraction of

the unstretched flame speed, which is used in this work, is derived from the methodology of Law *et al.* [78] based on a minimization of the expression Eq. VI.2. In order to validate the accuracy of our experimental measurements, a comparison with results from the literature is carried out and is presented in Fig. VII.1. Unstretched laminar burning velocity values are deduced from laminar flame speed using Eq. V.1. This figure compares our experimental values for the unstretched laminar burning velocity with other recent data [29, 30, 40, 31, 32, 33, 34, 35, 36, 37, 38] (which are acquired by employing a combustion vessel and are determined by linear extrapolation to a zero strain rate) and numerical results using GRI-Mech 3.0 [27] and GRI-Mech 2.11 [81]. For an equivalence ratio range of 0.6 - 1.3, experimental data obtained in the present work are in good agreement with those of other studies, especially with results of Tahtouh *et al.* [38]. A good agreement with numerical results is also found, particularly using the GRI-Mech 3.0 mechanism. This correspondence suggests that the algorithm used for the flame front extraction and the flame speed calculation are accurate. Fig. VII.2 illustrates the influence of linear and nonlinear extrapolation of the unstretched flame speed on the unstretched burning velocity. Both methods provide similar results in the case of lean and stoichiometric methane/air mixtures, but for rich mixtures some differences appear. In fact, according to the results of Tahtouh *et al.* [60] and Halter *et al.* [59], the nonlinear method is more suitable to extract the unstretched flame speed in the case of rich methane/air mixtures. To illustrate the influence of linear and nonlinear extrapolation on the unstretched flame speed, the evolution of flame speed as a function of flame stretch is presented in Fig. VII.3 and Fig. VII.4 for two different equivalence ratios, 1 and 1.2, respectively. As shown in these figures, the linear approximation is no longer valid for equivalence ratios higher than 1 and overestimates the unstretched flame speed and thus the unstretched burning velocity. The assumption  $S_f/S_f^0$ , which allows the formulation Eq. VI.3, is not satisfied and therefore the nonlinear extrapolation must be used.

### VII.1.2 Fresh gas velocity measurements

The main advantage of the new post-processing procedure is its ability to determine a global value of the fresh gas velocity,  $u_g$ , at the entrance of the flame front. This procedure is now

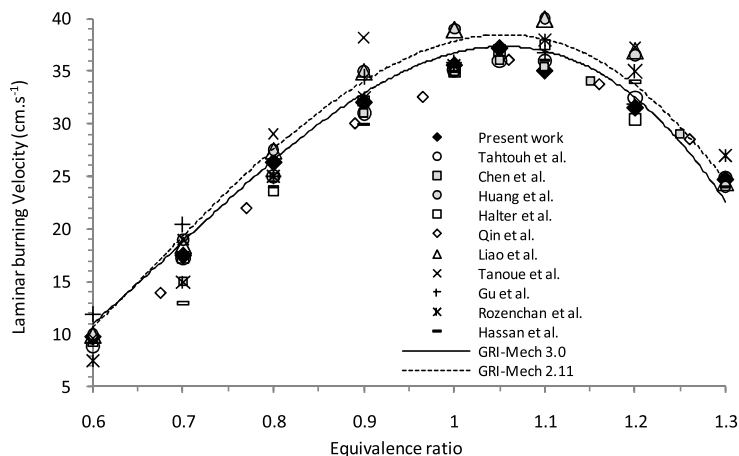


Figure VII.1: Unstretched laminar burning velocity  $u_s^0 = (\rho_b/\rho_u)S_f^0$  (linearly extracted) plotted against equivalence ratio. ( $CH_4$ /air mixture,  $P = 0.1$  MPa,  $T = 298$  K). Comparison with experimental data of previous work and calculations with GRI-MECH 3.0 and GRI-MECH 2.11. Tahtouh *et al.* [38], Chen *et al.* [82], Huang *et al.* [40], Halter *et al.* [31], Qin *et al.* [29], Liao *et al.* [32], Tanoue *et al.* [33], Gu *et al.* [35], Rozenchan *et al.* [34], GRI-Mech 3.0 [27], GRI-Mech 2.11 [81]

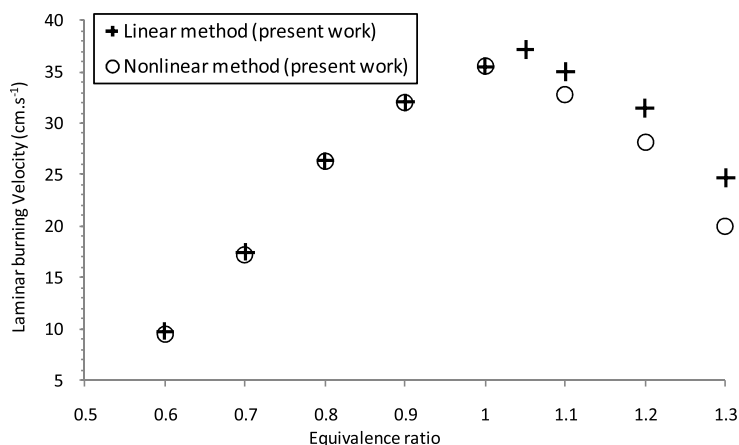


Figure VII.2: Relationship between unstretched laminar burning velocity  $u_s^0 = (\rho_b/\rho_u)S_f^0$  and equivalence ratio ( $CH_4$ /air mixture,  $P = 0.1$  MPa,  $T = 298$  K). Comparison of linear and nonlinear methodologies.

applied to methane/air flame images for various equivalence ratios at 0.1 MPa and 298 K. Variations of the fresh gas velocity and flame speed as a function of the stretch rate are shown in Fig. VII.5 and VII.6 respectively. In order to show the reproducibility of each experiment,

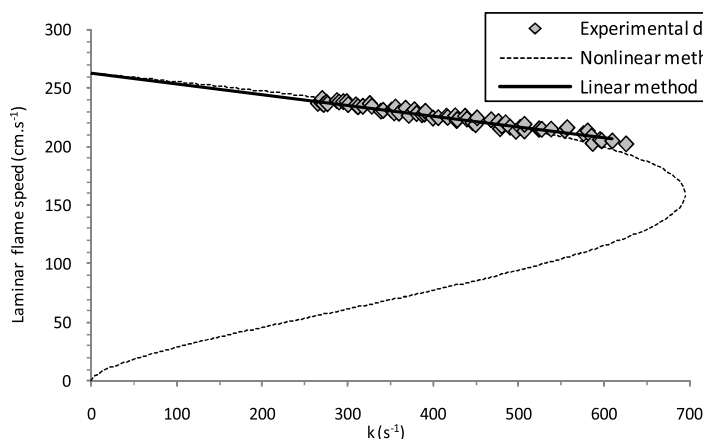


Figure VII.3: Evolution of flame speed as a function of flame stretch. Comparison of linear and nonlinear extrapolations of experimental data ( $CH_4$ /air mixture,  $\Phi=1$ ,  $P = 0.1$  MPa,  $T = 298$  K).

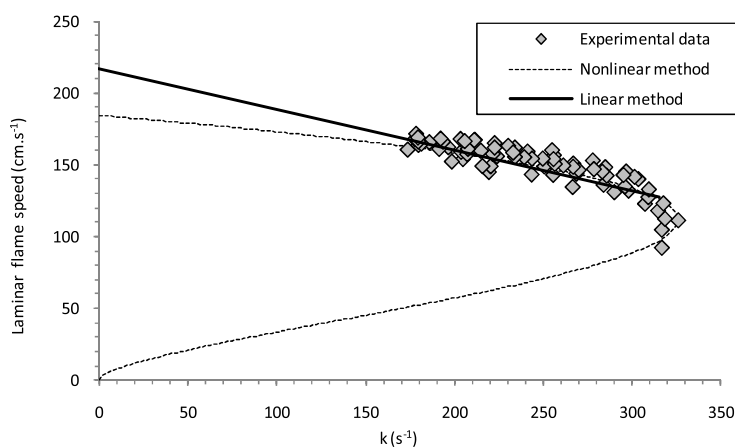


Figure VII.4: Evolution of flame speed as a function of flame stretch. Comparison of linear and nonlinear extrapolations of experimental data ( $CH_4$ /air mixture,  $\Phi= 1.2$ ,  $P = 0.1$  MPa,  $T = 298$  K).

data of five consecutive measurements are gathered in these figures. For all investigated mixtures, decreasing the stretch rate accelerates fresh gases and flame front. As in the relationship between flame speed and stretch rate, linear and nonlinear variations of the fresh gas velocity against flame stretch can be expected. Moreover, the equivalence ratio has the same influence on the evolution of fresh gas velocity and flame speed against stretch. Burning velocity is then directly calculated using the difference between values of fresh gas velocity and flame speed (cf. Eq. V.2).



In Fig. VII.7, the laminar burning velocity and the flame speed divided by the ratio of the densities of unburned to adiabatically burned gas are plotted as a function of flame stretch for a stoichiometric methane/air mixture at 0.1 MPa and 298 K. In this graph, the two expressions ( $u_n = S_f - u_g$  and  $\frac{\rho_b}{\rho_u} S_f$ ) present two very different evolutions versus the stretch, but in the case of methane/air flames they give nearly the same laminar burning velocity as when they are extrapolated to a zero stretch rate:  $u_n^0 = 35.5 \pm 0.5$  cm/s. As detailed in the computational study of Bradley *et al.* [28], the relation ( $\frac{\rho_b}{\rho_u} S_f$ ) assumes zero flame thickness and it does not describe the sensitivity of the burning rate to the flame stretch. This relation is only valid to determine the unstretched laminar burning velocity when the flame radius tends to infinity as Eq. V.1 and reported below.

$$u_n^0 \approx u_s^0 = \lim_{k \rightarrow 0} \frac{\rho_b}{\rho_u} S_f = \frac{\rho_b}{\rho_u} S_f^0 \quad (\text{VII.1})$$

The direct determination of burning velocity based on flame speed and fresh gas velocity measurements enables us to characterize the relationship between the burning rate and the flame stretch and to accurately determine unstretched laminar burning velocity without the use of fuel properties:

$$u_n^0 = \lim_{k \rightarrow 0} (S_f - u_g) \quad (\text{VII.2})$$

This observation between linear and non-linear extrapolation is illustrated in Fig. VII.8 and Fig. VII.9, in which linear and nonlinear extrapolations of the unstretched burning velocity are plotted and compared for the case of stoichiometric and rich methane/air mixtures. In Fig. VII.8, for an equivalence ratio of 1, linear and nonlinear values of unstretched burning velocity are similar. In Fig. VII.9, for an equivalence ratio of 1.2, some substantial differences appear at a zero stretch rate between linear and nonlinear formulations of burning velocity and overestimation by 12% is observed in the case of the linear extrapolation. Therefore, the nonlinear determination must be systematically applied in order to obtain more accurate values of the unstretched burning velocity. In the following sections of this study, describing our experimental results for isooctane and ethanol/air mixtures, all data will be exclusively nonlinearly extrapolated. To conclude, Fig. VII.10 compares non-linear values of unstretched laminar burning velocity that

were extracted using both processing approaches for an equivalence ratio range of 0.7 - 1.2. In the case of a methane/air mixture, both approaches provide similar results, which suggests that the new post-processing procedure is accurate in extracting fresh gas velocity at the entrance of the flame front as well as in attesting the validity of assumptions used to calculate burned gas density.

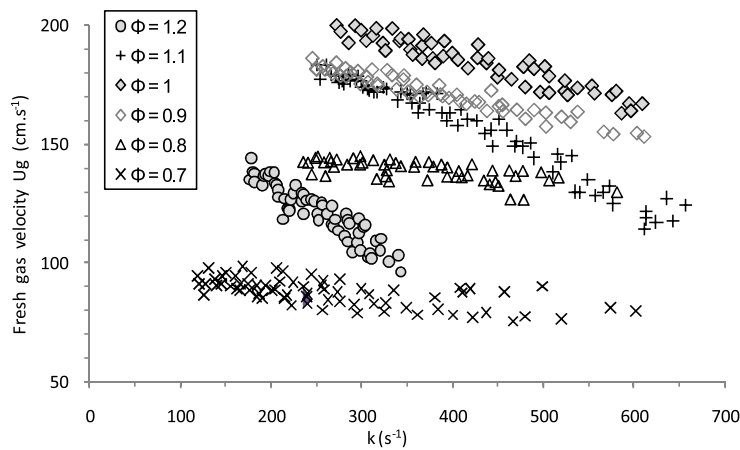


Figure VII.5: Variation of fresh gas velocity,  $u_g$ , as a function of flame stretch. ( $CH_4$ /air/mixture, P = 0.1 MPa, T = 298 K.)

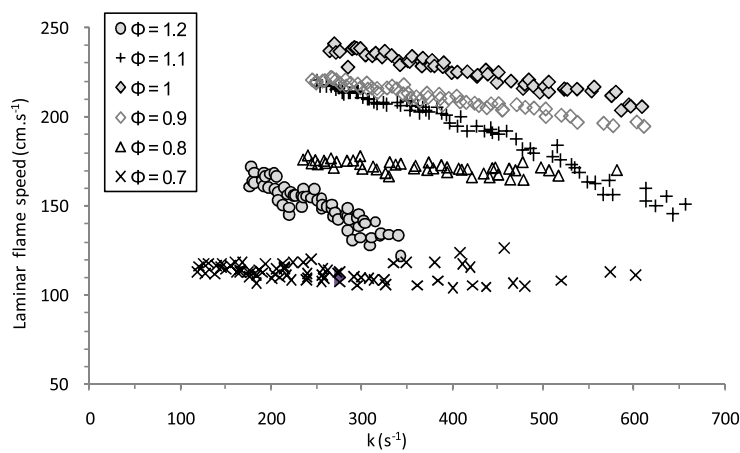


Figure VII.6: Variation of laminar flame speed,  $S_f$ , as a function of flame stretch. ( $CH_4$ /air mixture, P = 0.1 MPa, T = 298 K.)

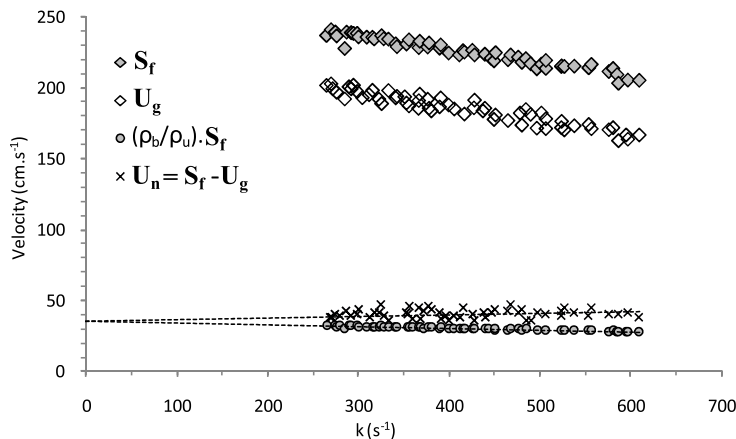


Figure VII.7: Variation of flame speed, fresh gas velocity and burning velocity as a function of flame stretch. Comparison between the two procedures of burning velocity calculation ( $CH_4$ /air mixture,  $\phi = 1$ ,  $P = 0.1$  MPa,  $T = 298$  K.)

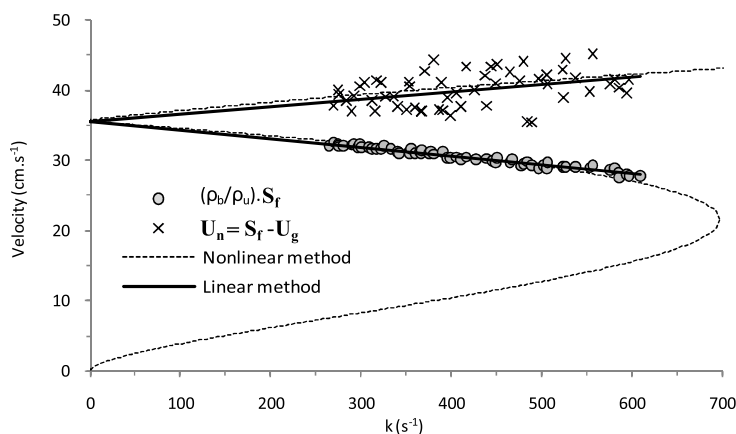


Figure VII.8: Linear and non-linear relationships between laminar burning velocity and flame stretch. Comparison between the two procedures of burning velocity calculation ( $CH_4$ /air mixture,  $\phi = 1$ ,  $P = 0.1$  MPa,  $T = 298$  K).

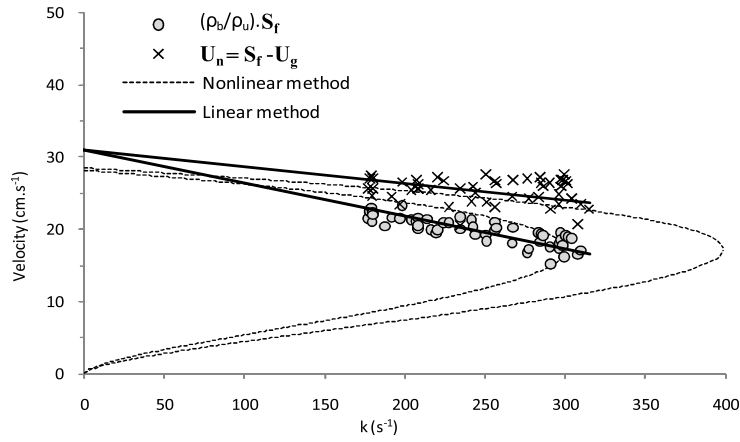


Figure VII.9: Linear and non-linear relationships between laminar burning velocity and flame stretch. Comparison between the two procedures of burning velocity calculation ( $CH_4$ /air mixture,  $\phi = 1.2$ ,  $P = 0.1$  MPa,  $T = 298$  K).

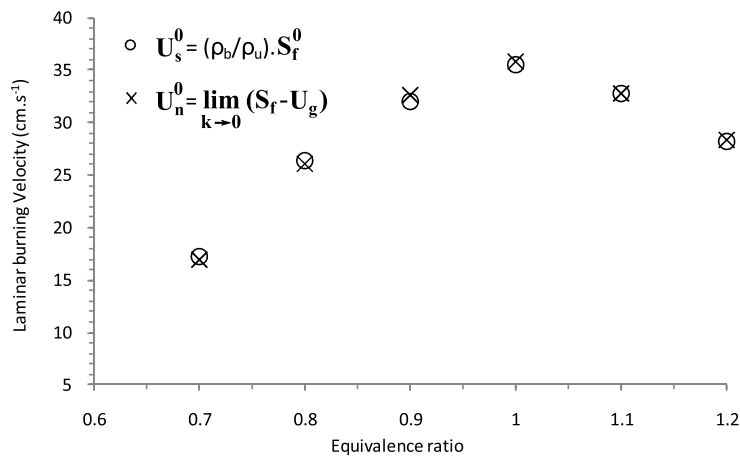


Figure VII.10: Unstretched laminar burning velocity (non-linearly extracted) plotted against equivalence ratio. Comparison between the two approaches of unstretched burning velocity calculation ( $CH_4$ /air mixture,  $P = 0.1$  MPa,  $T = 298$  K).

## VII.2 Isooctane/Air flames

First, in the case of isooctane/air mixtures, non-linear values of the unstretched laminar burning velocity ( $u_s^0$ ) (extracted using Eq. V.1) are plotted against the equivalence ratio in VII.11 for the following experimental conditions: 373 K, 0.1 MPa. The isooctane burning velocity exhibits a slight shift toward the fuel-rich region similar to the behavior of methane/air flames, where the maximal burning velocity peaks at 1.05. This trend is the same as those observed in previous studies [59, 83], whose values of burning velocity were also nonlinearly extracted. A comparison between the two approaches to the unstretched burning velocity calculation is also presented in this Figure. The equivalence ratio's influence on the unstretched burning velocity is the same for both approaches but the values of the unstretched burning velocity obtained directly using Eq. VII.2 are 5 - 12% higher than those calculated using Eq. V.1. Therefore, in the case of isooctane/air mixtures, the formulation Eq. V.1 underestimates the unstretched laminar burning velocity and involves inaccurate results because  $u_s^0$  differs from  $u_n^0$ . Recently, this difference has also been pointed out by Balusamy *et al.* [75] for propane/air mixtures at various equivalence ratios, in which case the underestimation of  $u_s^0$  is due to confinement effects of the wall, which tend to reduce flame speed for the larger flame radius. In our study, this explanation does not apply to methane/air flames, in which there is no difference between  $u_s^0$  and  $u_n^0$ . We therefore conclude that the principal reason for this difference in the case of isooctane/air flames lies in the burned gas density calculation that is used to determine the value of  $u_s^0$ . We will present some explanations of this difference in the next section for ethanol/air flames where similar results are observed.

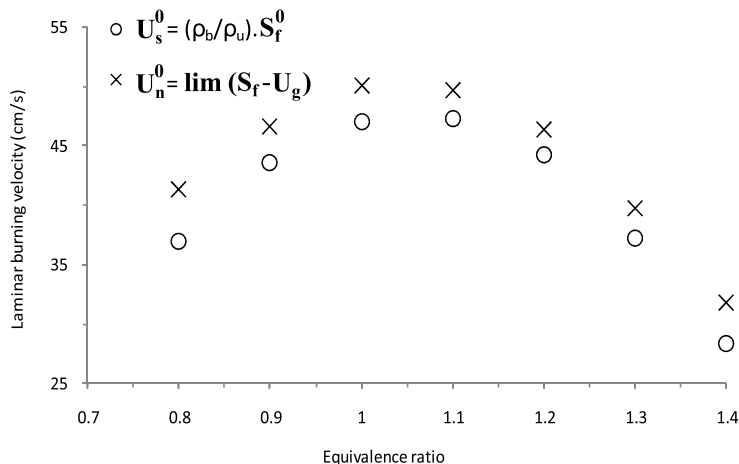


Figure VII.11: Unstretched laminar burning velocity (non-linearly extracted) plotted against equivalence ratio. Comparison between the two approaches of unstretched burning velocity calculation ( $C_8H_{18}$ /air mixture,  $P = 0.1$  MPa,  $T = 373$  K).

### VII.3 Ethanol/Air flames

In Fig. VII.12, non-linear values of unstretched laminar burning velocity ( $u_s^0$ ) are plotted against the equivalence ratio and compared to data obtained by Broustail *et al.* [84]. Because of the temperature difference between the two experiments, unstretched laminar burning velocities of [84] are higher than the data of our study, but they present the same trend against the equivalence ratio and the maximum velocity is close to  $\phi = 1.1$ . The two approaches to unstretched burning velocity calculations are compared in Fig. VII.13, and they have different magnitudes, particularly at equivalence ratios lower than 1. In this pressure range, values of  $u_s^0$  are 13 - 19% lower than values of  $u_n^0$ . This difference decreases by 2.5 - 6% for richer mixtures. As in the previous case of isooctane/air mixtures, the formulation Eq. V.1 underestimates the unstretched laminar burning velocity for ethanol/air flames. The main reason for this difference comes from the burned gas density estimation (generally computed for burned gases at chemical equilibrium for an adiabatic combustion) in Eq. V.1. So, if differences are observable between these two methods, it means either that the experimental flame is subjected to radiative effects (emission and absorption) or that the burned gases have not reached a chemical equilibrium state, for the propagation times investigated in the experiments. The first effect concerns radiative emission

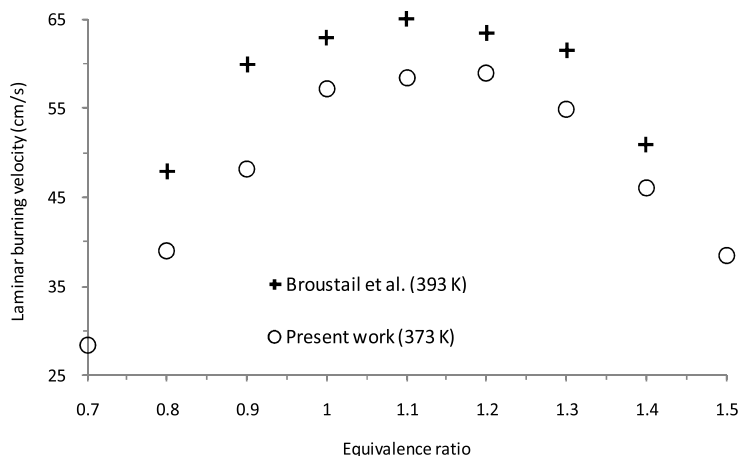


Figure VII.12: Unstretched laminar burning velocity,  $u_s^0 = \rho_b/\rho_u S_f$ , (non-linearly extracted) plotted against equivalence ratio. Comparison with previous work. Broustail *et al.* [84] ( $C_2H_5OH$ /air mixture,  $P = 0.1$  MPa).

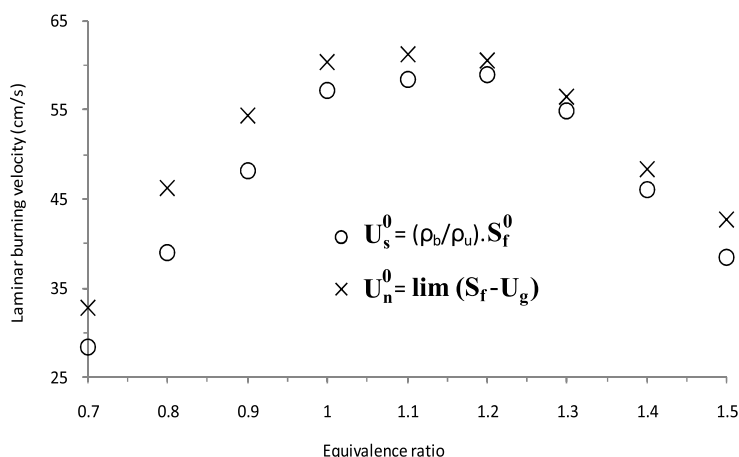


Figure VII.13: Unstretched laminar burning velocity (non-linearly extracted) plotted against equivalence ratio. Comparison between the two approaches of unstretched burning velocity calculation. ( $C_2H_5OH$ /air mixture,  $P = 0.1$  MPa).

and absorption, which are not taken into account in the adiabatic and equilibrium temperature. In the literature [85], this effect was numerically studied when the mixture was diluted by vapor or by  $CO_2$ . It was found that reabsorption of emitted radiation led to substantially higher burning velocities, particularly when  $CO_2$ , a strong absorber, was present in the unburned gas. For our experimental conditions, the IR spectra of isooctane and ethanol do not present any

absorption in the wavelengths of  $CO_2$  and  $H_2O$  emissions. In this way, radiative effects would not be the dominant effect of this difference. The second point could be linked to the equilibrium state of the burned gases in the experiments. Due to the finite size of the flame kernels (maximum radius 2 cm), the time or distance to reach the equilibrium state may not be obtained in the experimental configuration. To evaluate this effect, we use a kinetic modeling using the COSILAB package. The premixed flame is modeled by a *freely propagating flame* code, with GRI 3.0 kinetic mechanism for methane and a Konnov (release 0.5) mechanism for ethanol. For atmospheric conditions, the temperature profiles normalized by equilibrium temperature across the flame front are reported in Fig. VII.14. For methane/air flames, the distance to reach equilibrium is less than 1 cm, which corresponds to a typical flame radius at a small propagation time. This also has been observed by Bradley [28], who computed the temporal evolution of the flame temperature of freely propagating flames. We can observe that the temperature profiles according to time show the reaction to take some time (few ms) to be completed and to reach chemical equilibrium. At the end of propagation (i.e., for large flame radius), the temperature profiles in the burned gases are globally flat and equal to the equilibrium temperature. Consequently, for the measurements (methane/air flames), both methods globally give the same results. For ethanol and isooctane ( $P = 0.1$  MPa), the differences are larger. In Fig. VII.14, it clearly appears that the distance to reach the equilibrium state in the burned gases is higher than for the methane/air flames. An equilibrium solver for the density ratio could produce some error for these conditions, because it would artificially decrease the density ratio and therefore decrease the unstretched burning velocity. The pressure effect on the laminar burning velocity is then studied for a stoichiometric ethanol/air mixture at 373 K in Fig. VII.15. The pressure influence is characteristic of hydrocarbon/air mixtures and increasing the pressure from 0.1 to 0.5 MPa decreases the burning velocity by 33%. For this pressure range, no cellular structure appears during the flame front propagation. It is also worth noting that for high pressure conditions, the difference between the two methods decreases and becomes negligible at 0.4 MPa (Fig. VII.15). This can be explained by the Fig. VII.14 and VII.16, where it clearly appears that the equilibrium state of the burned gases is obtained faster when the pressure increases.



The method proposed in this paper does not require any assumption of adiabaticity or full equilibrium state of the burned gases to experimentally determine the unstretched laminar burning velocity.

In order to be more precise in explaining the difference between the two methods, we must can

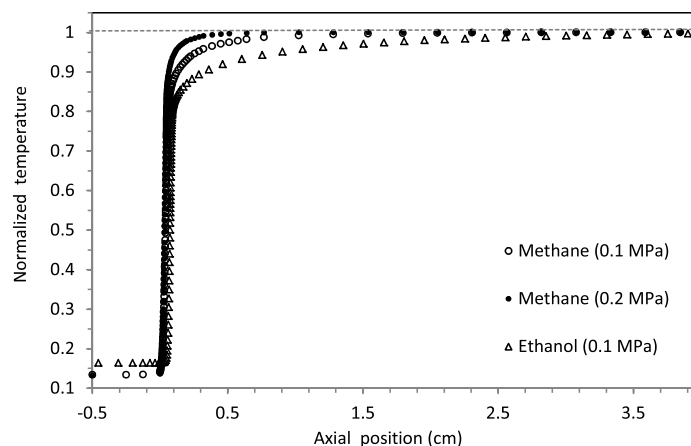


Figure VII.14: Temperature profiles for stoichiometric mixtures of methane and ethanol. (For each case, the temperature is normalized by the equilibrium temperature of burned gases).

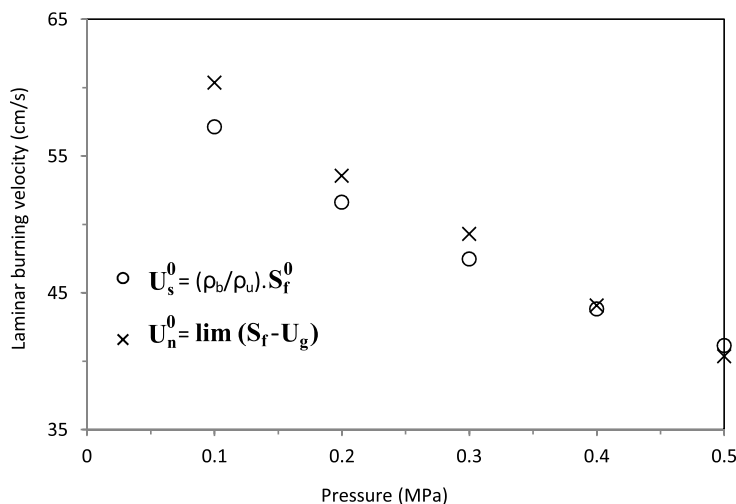


Figure VII.15: Unstretched laminar burning velocity (nonlinearly extracted) plotted against pressure. Comparison between the two approaches of unstretched burning velocity calculation ( $C_2H_5OH$ /air mixture,  $\phi = 1$ ,  $T = 373$  K).

represent the assumptions involved in the  $\rho$  ratio method (Eq. V.1) thanks to the Fig. VII.18.

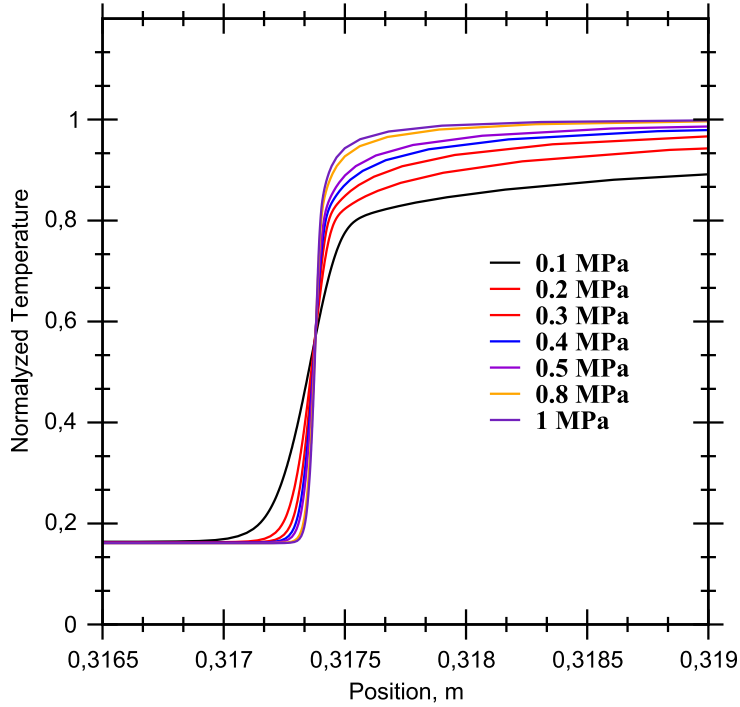


Figure VII.16: Temperature profiles for stoichiometric mixture of ethanol. For each case, the temperature is normalized by the equilibrium temperature of burned gases.

This scheme compares the cases of an idealistic flame (red lines) with which it is really observed (blue lines) or obtained from computation. In this graph, we report the temperature and the velocity of gases at the given position through the domain. In the experimental configuration, the radius measured,  $R_1$  is given at a specific isothermal,  $\approx 600\text{ K}$ , corresponding to the vaporization isothermal of particles.

- **Idealistic Model**

The model implies that whatever the isothermal considered, the absolute velocity remains constant [28].

It also assumes that the burned gases have no motion.

Under these considerations:

$$\begin{aligned}
 R_1 &\approx R_b \approx R_{eq} \\
 \frac{dR_1}{dt} &\approx \frac{dR_b}{dt} \\
 u &= 0 \quad \text{at} \quad R = R_b
 \end{aligned}
 \tag{VII.3}$$

In addition, when applying the linear relation to zero stretch:

$$\begin{aligned}
 \frac{dR_b}{dt} &= S_f(R_b) \\
 S_f(R_b) &= S_f^0(R_b) - L_b \kappa(R_b) \\
 \kappa(R_b) &\approx \kappa(R_1) \approx \kappa(R_{eq}) \\
 \frac{2}{R_b} \frac{dR_b}{dt} &\approx \frac{2}{R_1} \frac{dR_1}{dt} \approx \frac{2}{R_{eq}} \frac{dR_{eq}}{dt} \\
 u_n^0 &= \frac{\rho_b^{eq}}{\rho_u} S_f^0(R_b) \approx \frac{\rho_b^{eq}}{\rho_u} S_f^0(R_1) \approx \frac{\rho_b^{eq}}{\rho_u} S_f^0(R_{eq})
 \end{aligned} \tag{VII.4}$$

- **Real Flame**

Burned gases are not immobile, as proved in the computation of Groot *et al.* [79] (see Fig. VII.17). Burned gases tend to zero velocity far from the inner flame position ( $R_b=10\text{mm}$ ) that is  $\approx 2\text{ mm}$ .

The burned temperature reaches the equilibrium far from the flame's inner radius  $R_b$

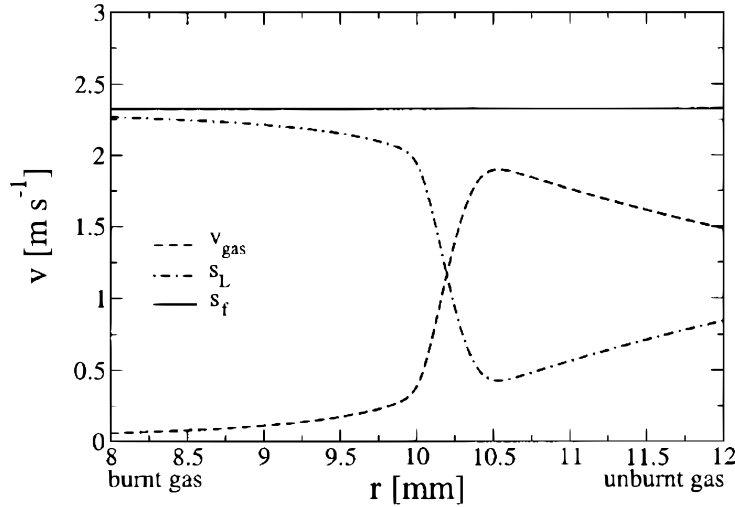


Figure VII.17: Gas velocity:  $v_{gaz}$ , burning velocity:  $S_l$ , and flame propagation:  $S_f$ , from [79].

These observations, equilibrium state and burned gases motion are in fact the two components of the mass conservation through the flame that is generalized as  $\rho S_d = \text{constant}$ , where  $S_d$  is the displacement speed:  $S_f - u$  of any isolevel, with  $u$  the gas velocity at the desired position.

Considering the model we clearly observe that the classical relation is satisfied:

$$\rho S_d^0 = \rho_u \lim_{\kappa \rightarrow 0} [S_f(R_u)] - u_g]_{T=T_u} = \rho_b S_f^0(R_b) = \rho_b^{eq} S_f^0(R_{eq}) \tag{VII.5}$$

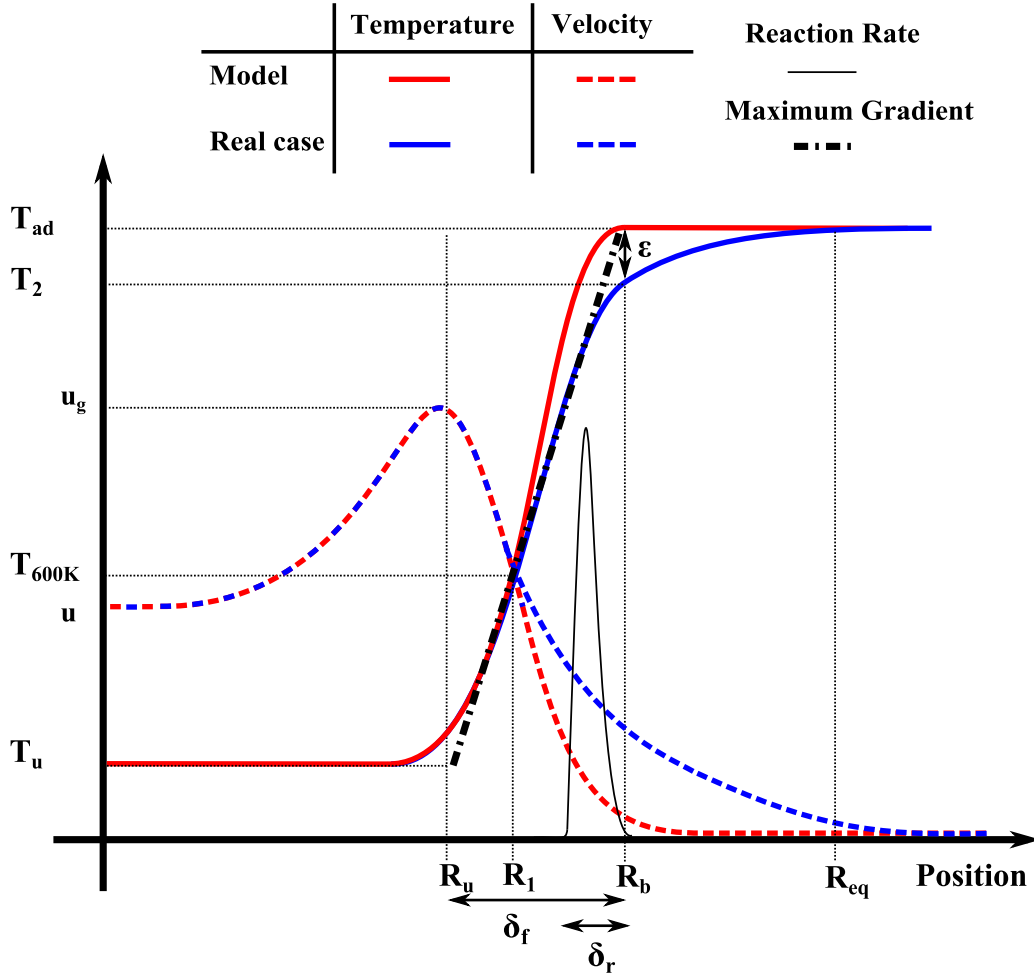


Figure VII.18: Comparison of 1D idealistic case and real flame.

However, in the real case, the mass conservation equation gives:

$$\begin{aligned}
 \rho S_d^0 &= \rho_u \lim_{\kappa \rightarrow 0} [S_f(R_1) - u_g]_{T=T_u} \\
 &= \rho_b^{eq} (S_f^0(R_{eq}) - u) = \rho_b^{eq} (S_f^0(R_{eq})) \\
 &= \rho_b (S_f^0(R_b) - u) \neq \rho_b^{eq} (S_f^0(R_b))
 \end{aligned}
 \tag{VII.6}$$

Moreover, we can assume that, because the flame spends time (or space  $\approx 3 \text{ cm}$  in ethanol's case) to reach the adiabatic value, the assumptions of a constant flame propagation speed whatever the isothermal considered can be erroneous. In fact, as observed by Bradley *et al.* [28], this assumption is satisfied but only within the flame thickness. Furthermore, the estimation of the stretch factor  $\kappa = \frac{2}{R} \frac{dR}{dt}$  used to extrapolate to zero stretch, can be highly affected by the considered isothermal because even if the propagation speed remains constant, the position,  $R$ , where

$\kappa$  is calculated can influence its value. In the graph below, Fig. VII.19, we report the evaluation to zero stretch of the propagation speed considering that the propagation speed remains constant whatever the isothermal but calculated with stretch factors at different isothermal radii. De Goey *et al.* [79] also reported this phenomenon and proposed to take the inner flame radius to extract informations such as the Markstein length.

Finally, it is possible to propose a parameter that describes the difference between the  $\rho$  ratio

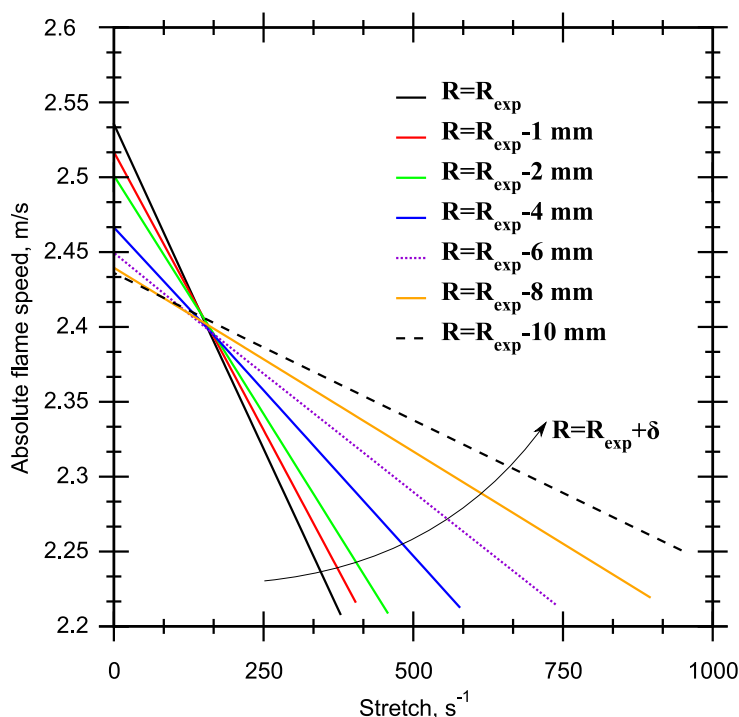


Figure VII.19: Estimation of the propagation speed to zero stretch for different isolevels considering a constant propagation velocity.  $\kappa = \frac{2}{R} \frac{dR}{dt}$ .

method and the kinematic one. This parameter is illustrated by  $\epsilon$ , that yields, in its normalized form,  $\epsilon = 1 - \frac{T_b}{T_{ad}}$ . It reveals the gap between the adiabatic state and the one at the position of the inner flame radius. As shown in ethanol or methane, increasing the pressure leads to reaching adiabatic condition faster than at lower pressure. The flame is quicker in tending to the idealistic case. In order to determine  $\epsilon$ , we propose to examine the temperature ratio  $T_b/T_{ad}$ , at the inner flame radius. This inner flame radius is calculated via the flame thickness estimation,

Eq. II.2:

$$\delta_f = \frac{T_{ad} - T_u}{\max|\frac{\partial T}{\partial x}|}$$

Fig. VII.20 illustrates the evolution of  $\epsilon$  increasing pressure from 0.1 MPa to 1MPa. Matching the results of laminar velocity obtained in ethanol case under pressure (VII.15) and the  $\epsilon$  evolution, a critical value of  $\epsilon_c$ , is found to be close to 0.17-0.16. This critical value, obtained at 0.5 MPa, is not so far from the one at 0.1 MPa, but it is important to note that a few percents in the misestimation of temperature changes density in the same order.

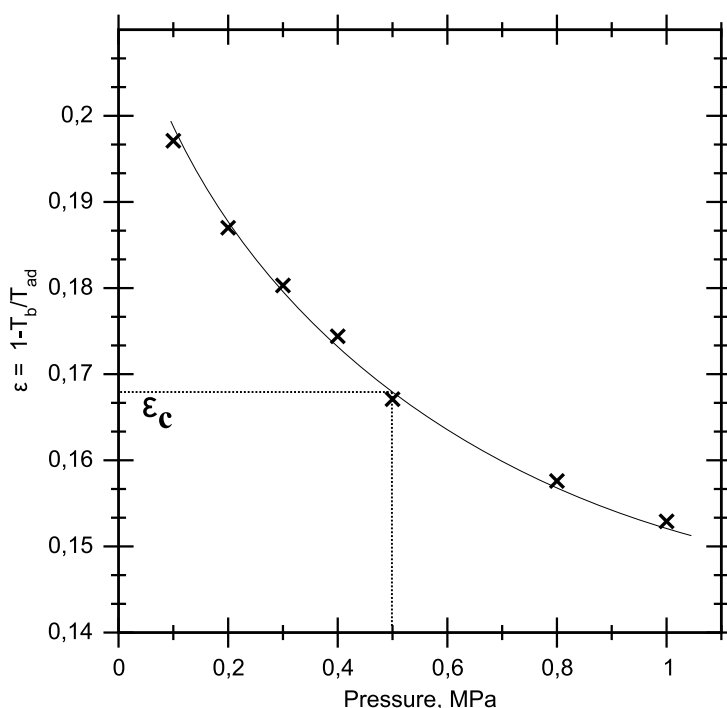


Figure VII.20: Estimation of  $\epsilon$  parameter under several conditions of pressure for 1D ethanol flames.  $\epsilon = 1 - \frac{T_b}{T_{ad}}$ .

## VII.4 Conclusion

A new tool for extracting the laminar burning velocity has been detailed and validated in the case of spherically outwardly expanding flames. This post-processing procedure directly determines the laminar burning velocity from the flame speed and the global fresh gas velocity near the preheat zone of the flame front. In this work, methane, isooctane and ethanol/air flames

have been studied under various experimental conditions in terms of equivalence ratios, temperature and pressure.

The influence of linear and nonlinear extrapolation on the unstretched burning velocity has been tested and, as previously presented in the literature, linear extrapolation results in overestimating unstretched burning velocity. Next, the unstretched laminar burning velocity has been nonlinearly extracted using the two processing approaches (based on the propagation flame speed and the displacement speed) and results have been compared. In the case of methane/air mixtures, the two methods give nearly the same results, but some differences appear for isooctane and ethanol/air mixtures. The main reason for the difference between the two methods comes from the burned gas density estimation (computed for burned gases at chemical equilibrium for adiabatic combustion). In the case of the isooctane and ethanol/air mixture, the burned gases have not reached a chemical equilibrium state for the propagation times investigated in the experiments. Indeed, due to the finite size of the flame kernels (maximum radius 2 cm), the time or the distance to reach the equilibrium state cannot be obtained in the experimental configuration for these mixtures. An equilibrium solver for the density ratio could produce some errors for these conditions because it would artificially decrease the density ratio and thus the unstretched burning velocity. This result indicates that, depending on the fuel considered, assumptions involved in the standard method (based on propagation flame speed) may, or may not, be satisfied. Questions can be suggested.

- Can we suppose a constant flame propagation speed whatever the isothermal considered, when the flame spends time (or space  $\approx 3$  cm) to reach the adiabatic value? Is  $S_f$ , when calculated at the isothermal of particle vaporization –  $\approx 600$  K –, identical to  $S_f$  collected 3 cm away, at burned gas equilibrium?

A critical parameter,  $\epsilon$ , illustrates the minimum distance to the adiabatic temperature for which both methods converge to the same value.





## Chapter VIII

# On the experimental determination of consumption speed

In the previous section, we have developed the experimental extraction method for laminar burning velocity by measuring displacement speed. In addition, we have noted that for either methane, isooctane or ethanol, different formulation sources – direct kinematic method ( $u_n$ ) or flame speed method ( $S_f$ ) – could lead to different values of laminar velocity. This chapter focuses on the third speed definition, namely consumption speed. As exposed in Chapter V, three definitions of this consumption speed can be found:

- Mitcheson's formulation

$$S_c = \frac{dR_f}{dt} - \frac{R_0^3 - R_f^3}{3R_f^2} \frac{1}{\gamma_u P} \frac{dP}{dt}$$

- Poinsot's Model

$$S_c = \frac{\rho_b^{eq}}{\rho_u} \frac{dR_b}{dt} \left[ 1 + \frac{\delta_l}{2R_b} \left( 1 + \frac{\rho_u}{\rho_b} \right) \right].$$

In the latest edition of *Poinsot-Veynante*, we find a similar expression:

$$S_c = \left( 1 + \frac{\delta_l}{R_b} \right) \frac{\rho_b^{eq}}{\rho_u} \frac{dR_b}{dt}$$

- Bradley's Model

$$S_c = \frac{\rho_b^{eq}}{\rho_b^{eq} - \rho_u} (u_n - S_f)$$

This chapter is divided into three parts. In the first part, we will focus on Mitcheson's formulation, detailing the treatment procedures and the results. In the second one, we will address the differences between Bradley's and Poinso's models. In the third part, we will compare the consumption speed from Bradley's model with the burning velocities obtained via displacement and flame speeds.

### VIII.1 Consumption Speed from Mitcheson's formulation

Analyzing Mitcheson's formulation of consumption speed leads to determining the pressure  $P$  and its time derivative  $dP/dt$ . To achieve the pressure chamber rise during the combustion process, a dynamic pressure transducer – Kistler 7001 – is used. Its sensitivity is of about 80 pC/bar and its natural frequency is close to 70 kHz. Attention is paid to insulating the transducer from noise caused by the spark ignition system or electromagnetic radiance from electrical equipment. The transducer has to be used without any duct or damping to ensure a pass band at 30% of its natural frequency. If not, the pressure measured is erroneous and must be corrected. The field of view has been extended to  $70 \times 70 \text{ mm}^2$ . The resolution drops, making it impossible to measure the fresh gas velocity profile. However, this formulation requires determining the flame front for the radius information. Typical pressure rise and its corresponding time derivative are given in the Fig. VIII.1. These graphs represent the total recording of the combustion process up to 0.1 s. However, we will only focus on the first 10% of the pressure signal. Because the pressure signal is noisy, a median filter, applied six or fifteen times on the raw pressure signal, is used to minimize the perturbation during the derivation process for the evaluation of  $dP/dt$  calculated with a centered scheme. However, the result of the filtered signal submitted to derivation remains noisy with the six time median filter. We

will therefore use the 15 time filter.

In the formulation V.3, the spherical bomb radius is needed. In order to take into account the

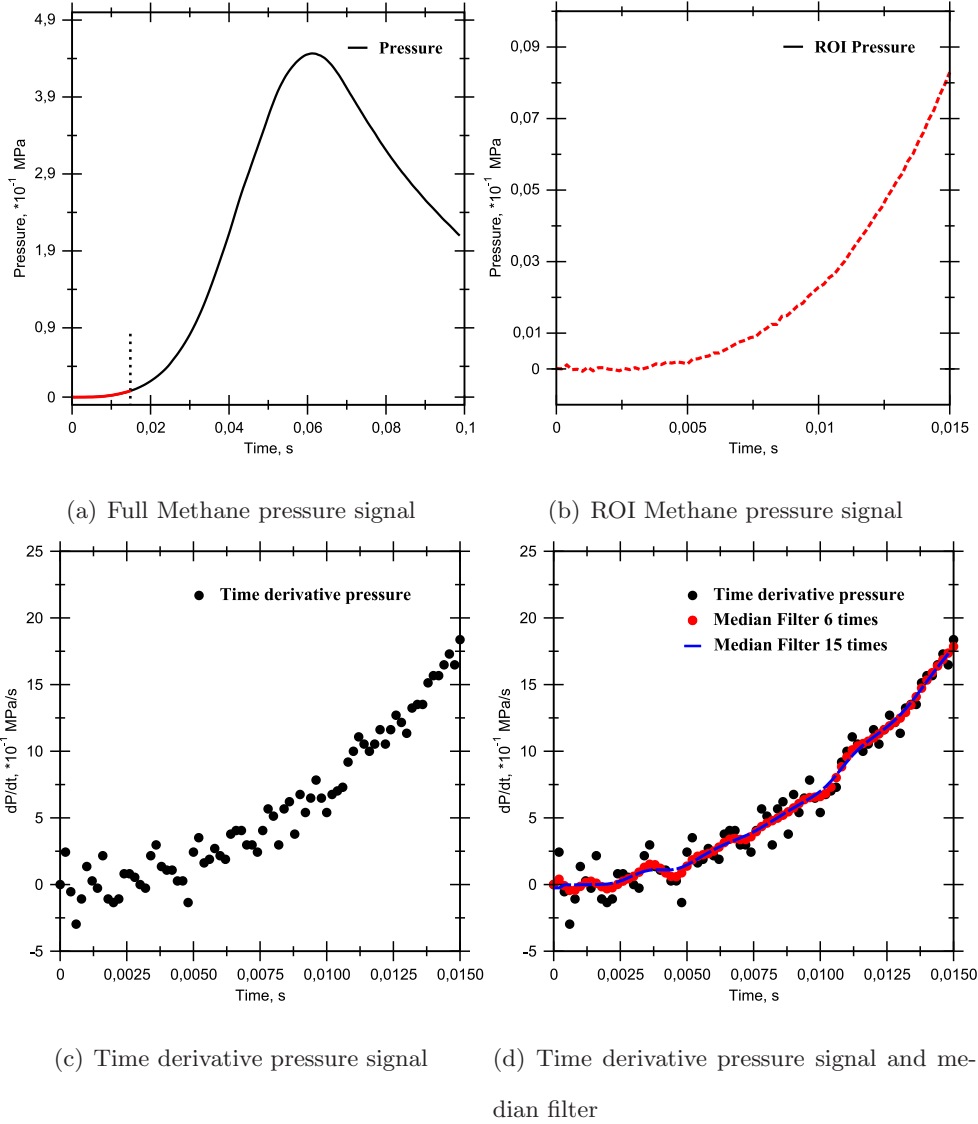


Figure VIII.1: Methane pressure and time derivative pressure signal,  $\phi = 1$  P=0.1 MPa, T=300 K.

real design of the chamber that is not perfectly spherical due to the presence of optical accesses, an equivalent bomb radius has been determined filling the chamber with water. An equivalent spherical radius of about 8.25 cm was found. A first computation of the consumption speed is presented in the graph below. It represents the evolution with stretch of the flame speed ( $S_f$ ), the pressure correction term ( $\frac{R_0^3 - R_f^3}{3R_f^2} \frac{1}{\gamma_u P} \frac{dP}{dt}$ ) and the corresponding difference between these two values.  $\gamma_u$  is found to be equal to 1.389 for a methane/air flame at  $\phi = 1$ ,  $T = 300 K$ . We observe

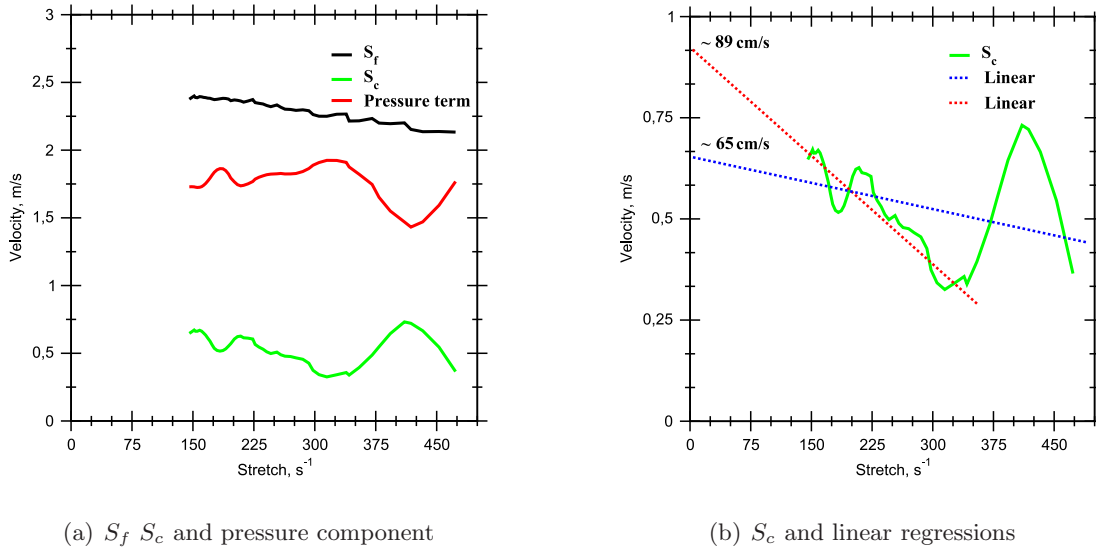


Figure VIII.2:  $S_f$ ,  $S_c$  and pressure component, methane  $\phi = 1$  P=0.1 MPa, T=300 K.

that consumption speed is not well estimated using this procedure. The evolution with stretch is very unstable. Two linear regressions have been tested. The first one considers the entire velocity, the second one is limited to smaller stretch values. The results of  $S_c$  to zero stretch gives in the corresponding cases 65 cm/s and 89 cm/s. These values are clearly erroneous, for they are too far from the pointing value of about 35.5 cm/s. Looking at the equation, we notice some issues in the calculation of  $S_c$ .

- The value of the spherical bomb radius  $R_0$
- The pressure signal and its corresponding filter or fit

The first issue can be solved by determining an empirical bomb radius,  $R_0^e$ , allowing an extrapolation at an appreciable value of the unstretched consumption speed, close to 35 or 36 cm/s. This empirical radius,  $R_0^e$ , is found to be close to 8.89 cm. The extrapolation at limited stretch has been used in order to avoid important perturbations at higher values of stretch. The value shifts down from 89 to 36 cm/s. Once this radius is determined, it is possible to appreciate the unstretched consumption speed at another given equivalence ratio. Fig. VIII.3 presents the consumption speed evolution of a methane/air flame at P=0.1 MPa,  $\phi = 0.8$  and  $T = 300$  K. We observe that, even though the empirical radius has been tuned to obtain an appreciable consumption speed for a stoichiometric mixture, this is not the case for this lean ( $\phi = 0.8$ )

condition:  $S_c \approx 40 \text{ cm/s}$ . Furthermore, from the equivalent bomb radius –  $R_0 = 8.25 \text{ cm}$  – to the empirical one –  $R_0^e = 8.89 \text{ cm}$  –, an increase of 7% of the radius causes velocity to decrease by 60%. The expression seems to be extremely sensitive to the radius parameter.

The second issue lies in fitting the time-derivative pressure term  $dP/dt$ . Results obtained at

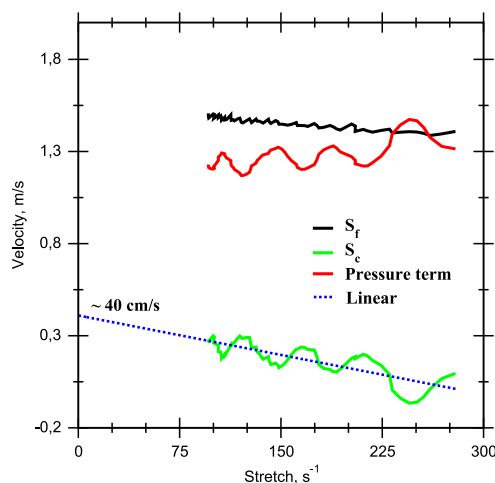


Figure VIII.3:  $S_c$  lean condition, methane  $\phi = 0.8$  P=0.1 MPa, T=300 K

$\phi = 0.8$  and  $\phi = 1$  using a median filter are reported above. Diffusive filters or polynomial fits could also be used. A diffusive filter has been used that gives quite similar results to a median filter, see Fig. VIII.4(a). Concerning polynomial fits, Fig. VIII.4(b) shows an example of  $S_c$  calculated applying a third and a fourth-order polynomial fit on the pressure signal. As a result, the pressure term and corresponding consumption speed completely depend on the polynomial order. The main problem with polynomial fits is that the derivation function is imposed.

This section clearly shows that calculating consumption speed using Mitcheson’s formulation is a complex process. The bomb radius  $R_0$  is a critical parameter. The formulation is highly sensitive to this parameter. However, the pressure signal can not be used without filtering or fitting the raw data due to irreducible noise during the recording process. Pressure variation is small – less than 0.1 bar in the most favorable case ( $\phi = 1$ ) –, and the corresponding time-derivative values are very noise-sensitive. It clearly appears that this formulation cannot be used for consumption speed determination.

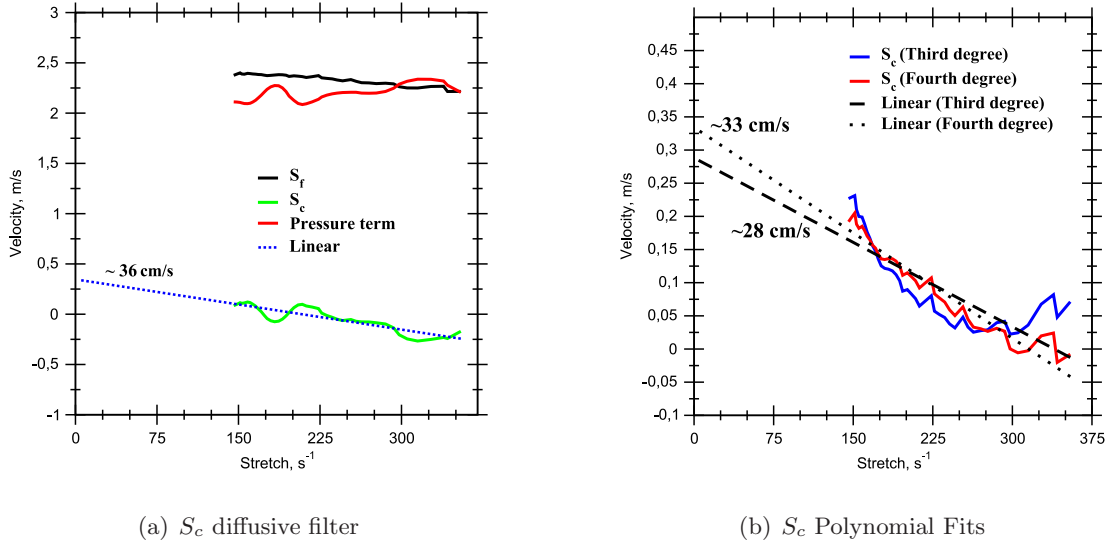


Figure VIII.4: Evolution of the consumption speed,  $S_c$ , calculated using a diffusive filter and Polynomial Fits (third and fourth degree) for a  $CH_4$ /air flame at  $P = 0.1$  MPa,  $T = 298$  K

## VIII.2 Bradley's and Poinso's Models

This section presents the two consumption speed formulations proposed by Bradley and Poinso. As described in chapter IV, Bradley's model considers a finite flame thickness with a linear variation of the density along the flame brush. Poinso's model uses a constant density through the flame. Using Poinso's models ( Eq. V.4 and Eq. V.5), flame thickness and its evolution with equivalence ratios must be determined. These values are obtained thanks to a 1D computational flame. The thickness is estimated by thermal definition Eq. II.2:  $\delta_f = \frac{T_{ad} - T_u}{\max|\frac{\partial T}{\partial x}|}$ . As mentioned in the theoretical part regarding the one-dimensional flame, this flame thickness definition yields more realistic values than the one obtained with the diffusional definition Eq. II.1. The evolution of flame thickness with equivalence ratio for a range varying from 0.7 to 1.2 is presented below (Fig. VIII.5).

The corresponding evaluations of Eq. V.4 or V.5 are reported in graph VIII.6(a) as a function of the equivalence ratio. Extrapolation to zero stretch yields quite identical results. However, it is interesting to look at Markstein length for both formulations. Graph VIII.6(b) shows that sensitivity to stretch are totally different in both Poinso's models. A sensitivity analysis shows that the magnitude of the term corresponding to flame thickness is of the order of  $10^{-2}$ .

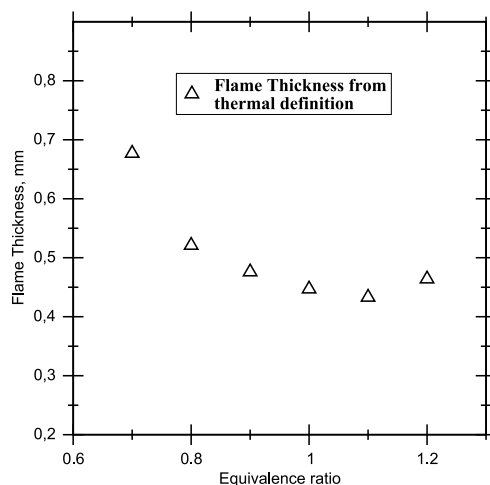
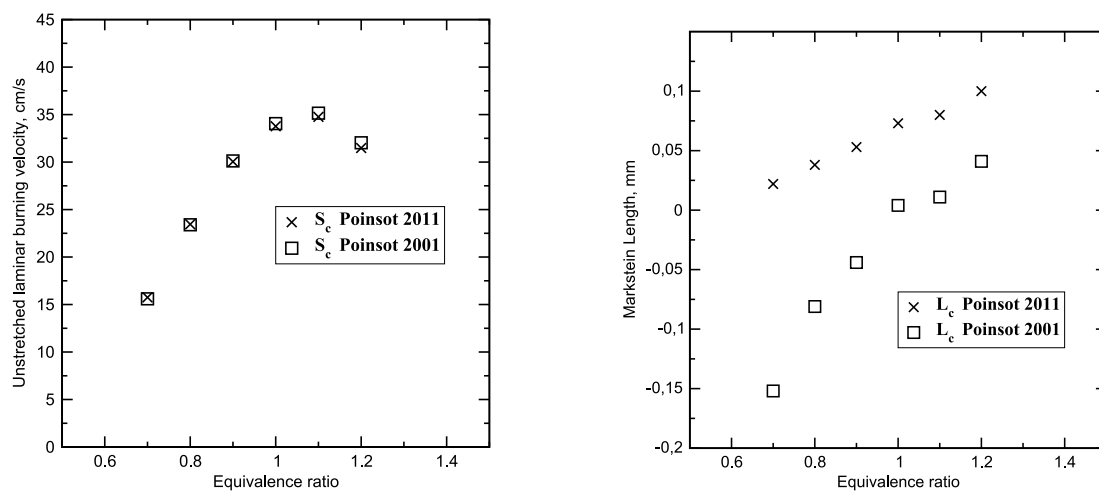


Figure VIII.5: Evolution of the flame thickness with equivalence ratio for a  $CH_4$ /air flame at  $P = 0.1$  MPa,  $T = 298$  K.

This shows that even though this term is not preponderant, both Poinso's models are heavily influenced in their sensitivity to stretch. The comparison of the evolution as a function of



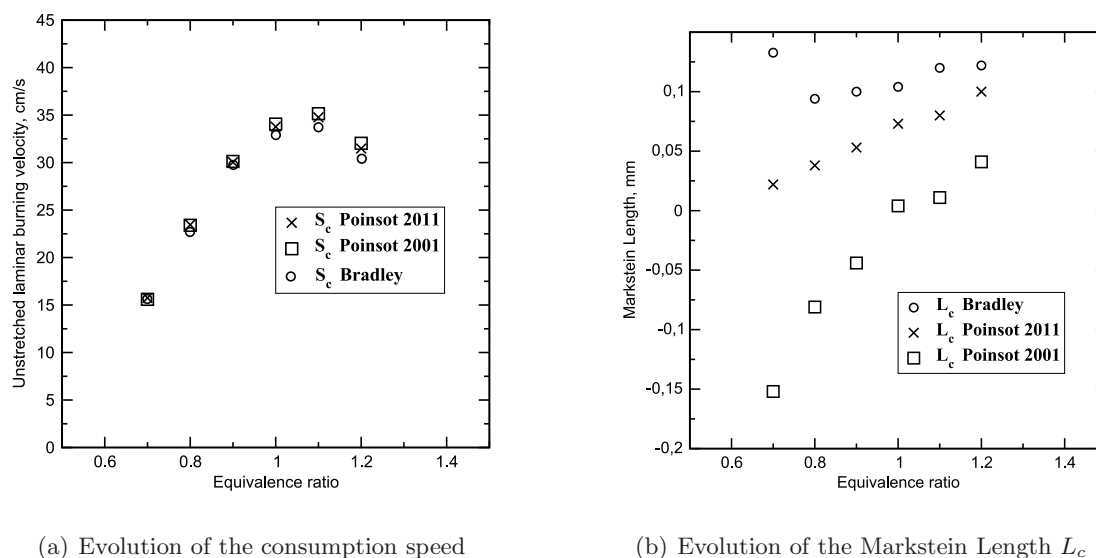
(a) Evolution of the consumption speed  $S_c$

(b) Evolution of the Markstein length  $L_c$

Figure VIII.6: Evolution of the consumption speed,  $S_c$ , and Markstein length,  $L_c$ , estimated with the two Poinso's models V.4 and V.5 for a  $CH_4$ /air flame at  $P = 0.1$  MPa,  $T = 298$  K.

equivalence ratio of the consumption speeds obtained with the models of Bradley Eq. V.6 and Poinso Eq. V.4 or Eq. V.5 are presented in graph Fig. VIII.7(a) for equivalence ratios from 0.7 to 1.2. We observe that the three models yield very similar consumption speed values and that differences are lower than the order of uncertainty ( $1.5$  cm/s). However, analyzing their

sensitivity to stretch, Fig. VIII.7(b), we note that the three models do not yield the same trends. Furthermore, Poinso's model V.4 yields negative values of  $L_c$ . This shows that the dependence of the estimated stretched consumption speed completely depends on the model. The density along the flame brush is a crucial point and must be determined by a full 3D computation including detailed chemistry.



(a) Evolution of the consumption speed

(b) Evolution of the Markstein Length  $L_c$ 

Figure VIII.7: Evolution of the consumption speed,  $S_c$ , and Markstein length,  $L_c$ , estimated with Poinso's model V.5 and Bradley's model V.6 for a  $CH_4$ /air flame at  $P = 0.1$  MPa,  $T = 298$  K.

### VIII.3 Conclusion

This chapter has developed the experimental ways to determine consumption speed. Three models have been tested, based on different approaches of density evolution through the flame front: Mitcheson's formulation, based on the disappearance of fresh gases with isentropic compression and infinitely thin flame; Poinso's models that propose a constant density value through the flame front; and Bradley's model, that assumes a linear variation of density through the flame front. These formulations can be summarized as follows:

- Looking at Mitcheson's formulation, we demonstrated that consumption speed is com-



pletely dependent on and extremely sensitive to both the  $R^0$  parameter – the inner chamber radius – and the fitting functions of the pressure signal. Finally, Mitcheson’s formulation is very difficult to implement experimentally.

- Concerning Poinso’s and Bradley’s models, even though unstretched velocities are well estimated, their sensitivity to stretch –  $L_c$  – completely depends on the model and opposite values can be observed.

Estimating that the linear evolution as described in Bradley’s model is more accurate (though still wrong) than the average imposed in Poinso’s model, Bradley’s model is chosen for further investigations.

In the next part, we will focus on comparing Bradley’s model Eq. V.6 to direct kinematic method ( $u_n$ ) and flame speed formulation ( $\frac{\rho_b^{eq}}{\rho_u} S_f$ ) and investigate their dependence on Lewis number.



## Chapter IX

# Flame response to stretch

In the theoretical part, Markstein length's dependence on velocity definition was examined (III.2.2). This analysis showed that Lewis numbers have an important influence on Markstein length's sign, which we propose to investigate in this chapter. First, we will examine the effect of Lewis number on unstretched velocities  $S_f^0$ ,  $u_n^0$  and  $S_c^0$ . Then, we will study and compare Markstein lengths  $L_b$ ,  $L_u$  and  $L_c$  with literature. We selected three representative fuels whose properties will enable us to clearly identify the effects of preferential diffusivity. Methane is chosen because of its near-unity Lewis number; hydrogen and propane are chosen because their Lewis numbers are respectively lower and greater than unity. We will subsequently expose that flame temperature is affected by both stretch and Lewis number. Lewis number is calculated applying the procedure described in Appendix A. As mentioned above, we will use Bradley's model Eq. V.6 to estimate consumption speed.

### IX.1 Velocity

- Methane

Graph IX.1 shows the evolution of three burning velocities  $-\frac{\rho_b}{\rho_u} S_f$ ,  $u_n = S_f - u_g$  and  $S_c$ . Looking at our chosen velocities' behavior towards stretch, we observe that even though they yield equivalent or similar unstretched values, their behavior is nonetheless completely different as shown in graph IX.2. In this graph, the normalized evolution of the three

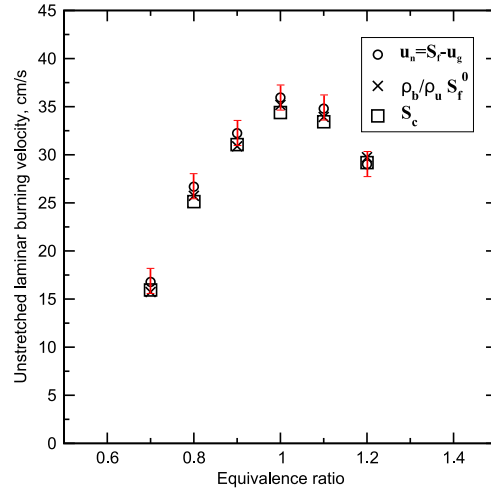
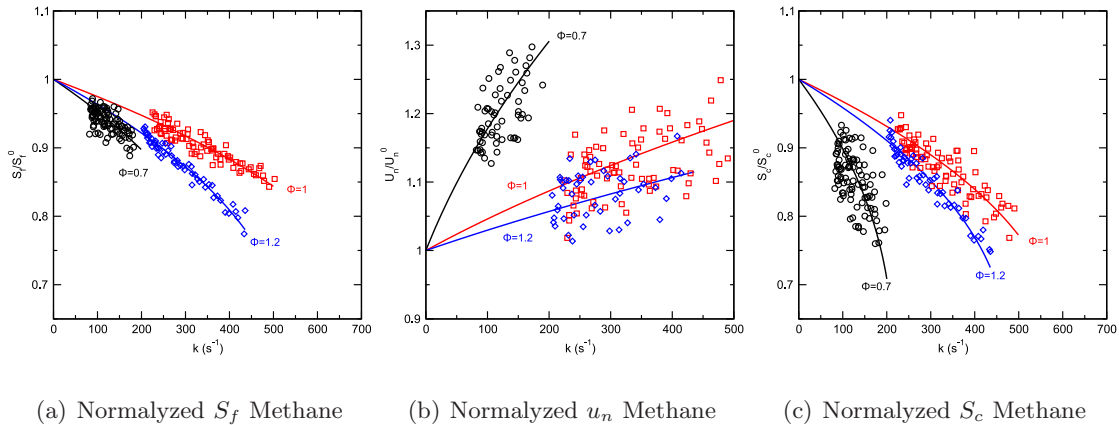


Figure IX.1: Comparison of  $S_f$ ,  $u_n$  and  $S_c$  for methane/air flames,  $P=0.1$  MPa,  $T=300$  K

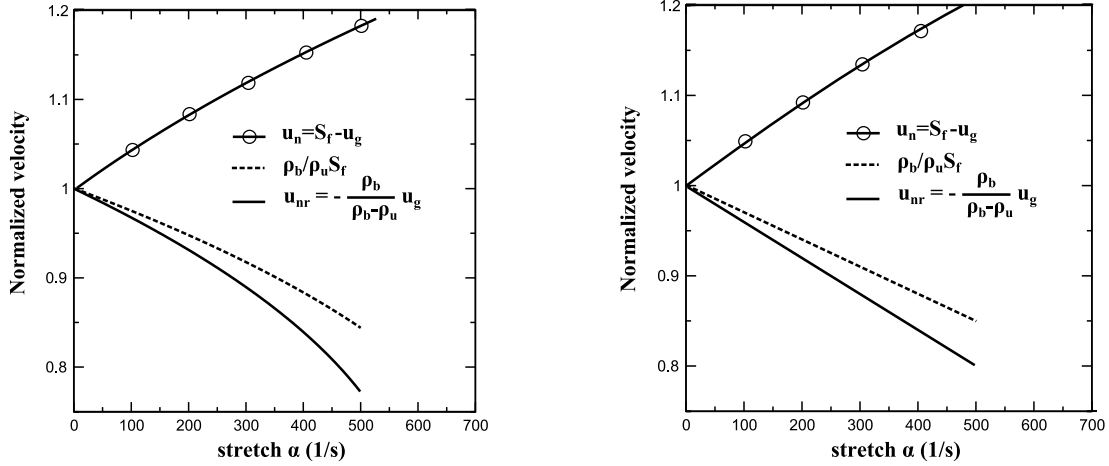
velocities –  $\frac{\rho_b}{\rho_u} S_f$ ,  $u_n = S_f - u_g$  and  $S_c$  – for three chosen equivalence ratios – 0.7, 1, 1.2 is reported. Even though these results cannot be compared to experimental data, except



(a) Normalized  $S_f$  Methane      (b) Normalized  $u_n$  Methane      (c) Normalized  $S_c$  Methane

Figure IX.2: Comparison of  $S_f$ ,  $u_n$  and  $S_c$  for a methane/air flame at given equivalence ratios,  $P=0.1$  MPa,  $T=300$  K.

for  $S_f$ , we can rely on Bradley's work [28]. In his computations, Bradley obtained the evolution of these velocities against stretch. Data from Bradley's experiments have been adapted – normalized and resized to our stretch range – to allow relevant comparison with our work. Graph IX.3 illustrates this comparison. A remarkable agreement is observed between our experimental data and Bradley's. Such agreement could be expected for  $S_f$ , its determination no longer being a big issue, neither experimentally nor numerically. However, such results for  $u_n$  and Bradley's model Eq. V.6 are of deep interest for they

(a)  $S_f$ ,  $u_n$  and  $S_c$  from this study(b)  $S_f$ ,  $u_n$  and  $S_c$  from Bradley computation

[28]

Figure IX.3: Comparison of  $S_f$ ,  $u_n$  and  $S_c$  for a stoichiometric methane/air flame,  $P=0.1$  MPa,  $T=300$  K.

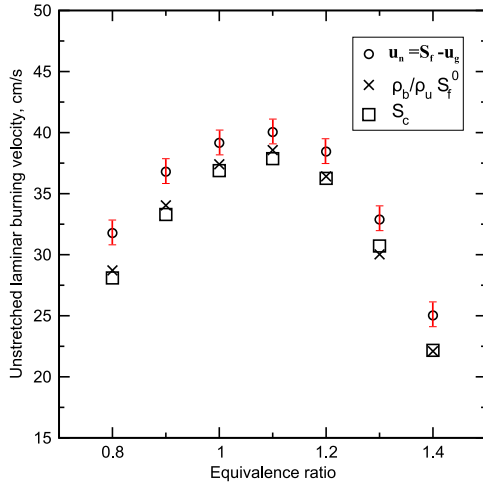
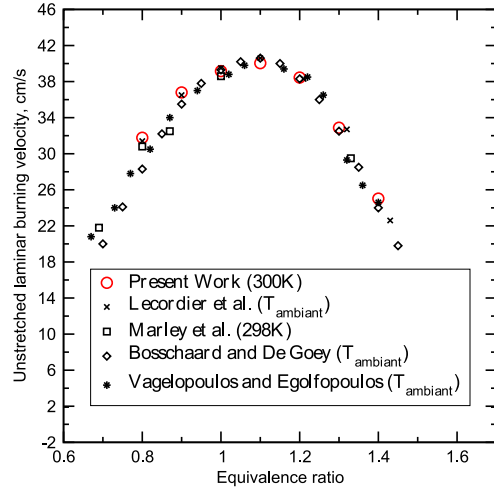
cannot be determined without estimating their  $u_g$  value. We can therefore conclude that  $u_g$  is determined accurately, both numerically and experimentally.

- Propane and Hydrogen

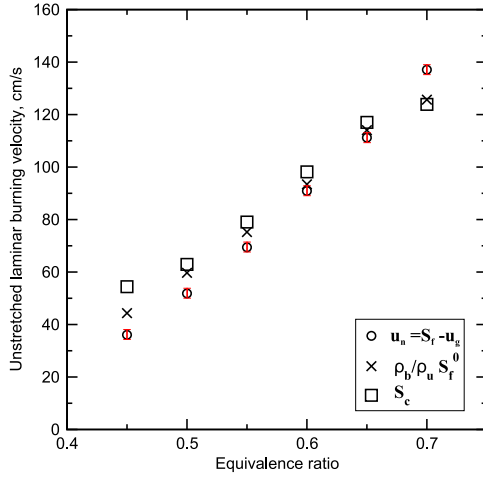
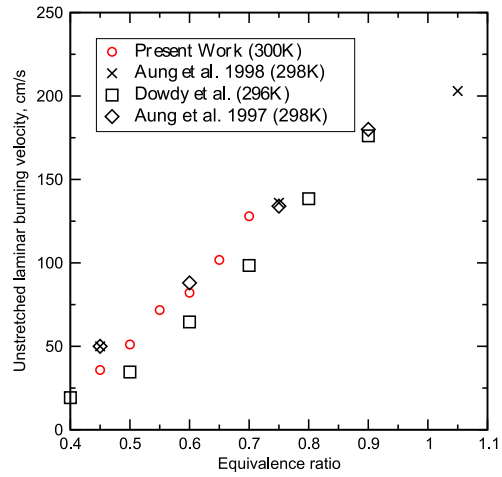
Graph IX.4 shows the evolution of laminar burning velocities obtained by  $\frac{\rho_b}{\rho_u} S_f$ ,  $u_n = S_f - u_g$  and  $S_c$ , for both propane and hydrogen. Our data – displacement speed only – are compared with literature in graph IX.4. Analyzing these results, we observe that classical formulation  $\frac{\rho_b}{\rho_u} S_f^0$  and Bradley's model's  $S_c^0$  yield very similar values for both propane and hydrogen. However, differences can be noted when displacement speed is considered, as was mentioned in Lecordier's study [75] for propane (see Fig. IX.5). Lecordier *et al.*, attributed these differences to the confinement effect, which tends to reduce flame speed and gas velocity in large flame radius. Nevertheless, in methane (Fig. IX.1), such differences do not exist.

Taking  $u_n$  as a reference, we draw the following conclusions:

- Methane: the three velocities are similar
- Propane:  $\frac{\rho_b}{\rho_u} S_f^0$  and  $S_c^0$  yield lower values

(a)  $\frac{\rho_b}{\rho_u} S_f^0$ ,  $u_n$ ,  $S_c^0$  Propane

(b) Propane data compared with literature

(c)  $\frac{\rho_b}{\rho_u} S_f^0$ ,  $u_n$ ,  $S_c^0$  Hydrogen

(d) Hydrogen data compared with literature

Figure IX.4: Comparison of  $\frac{\rho_b}{\rho_u} S_f^0$ ,  $u_n$ ,  $S_c^0$  for propane and hydrogen/air flames and comparison with literature for  $u_n$ ,  $P=0.1$  MPa,  $T=300$  K. References for propane: Lecordier *et al.* [75], Marley *et al.* [86], Bosschaard and De Goeij [87], Vagelopoulos and Egolfopoulos [41]. References for hydrogen: Aung *et al.* 1997 [88], Dowdy *et al.* [89], Aung *et al.* 1998 [90]

– Hydrogen:  $\frac{\rho_b}{\rho_u} S_f^0$  and  $S_c^0$  yield higher values

As a result, these differences cannot only be explained by the confinement effect theory. We know that  $\frac{\rho_b}{\rho_u} S_f^0$  and  $S_c^0$  cannot be determined without burned gas density – always idealistically assumed to be at equilibrium. However, in real flames, the equilibrium state is not satisfied because the flame's temperature is affected by stretch (see Clavin and

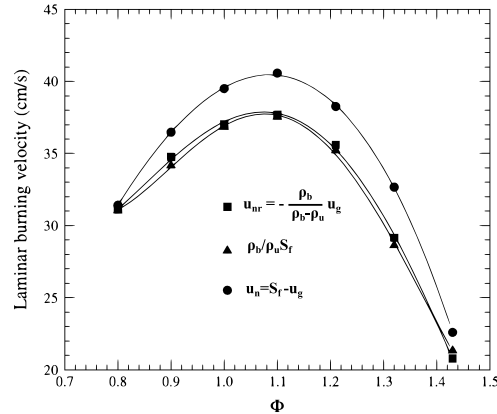


Figure IX.5:  $\frac{\rho_b}{\rho_u} S_f^0$ ,  $u_n^0$ ,  $S_c^0$  for propane/air flames from [75],  $P=0.1$  MPa,  $T=300$  K

Williams [62], Matalon [91], Law [92]).

Assuming that:

- $\rho_b$  does not vary in space
- flames are subjected to small stretch

the burned gas flame temperature can be expressed as follows:

$$\frac{T_b - T_{ad}}{T_{ad}} = \left( \frac{1}{Le} - 1 \right) \frac{D}{(S_L^0)^2} \kappa. \quad (\text{IX.1})$$

where  $D$  is the thermal diffusivity of the mixture.

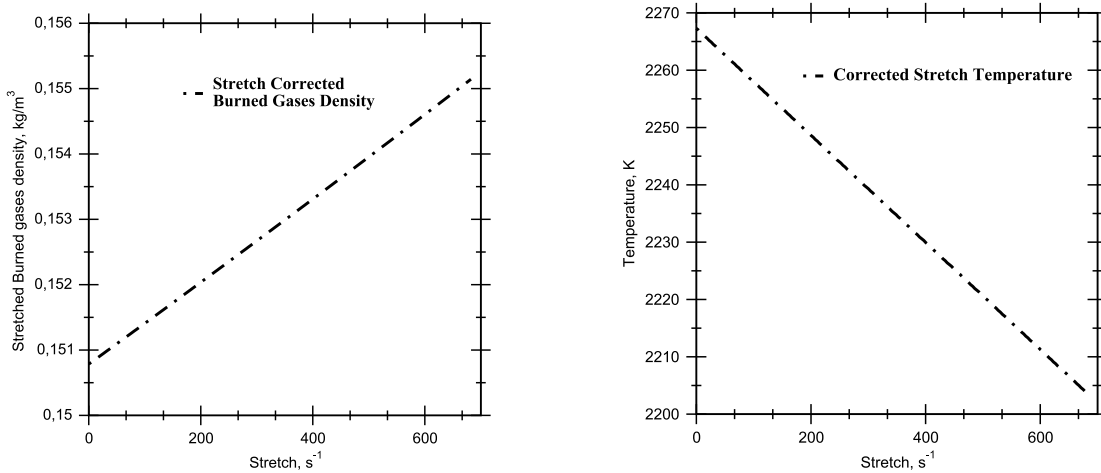
We clearly observe that stretch and non-unity Lewis numbers deviate flame temperatures from the adiabatic value. The aforementioned deviation in flame temperature directly modifies burned gas density. The flame's temperature varies and can reach super or sub-adiabatic values. For Lewis numbers  $> 1$  – hydrogen –  $\frac{1}{Le} - 1$  is greater than unity and burned gas temperature reaches a super-adiabatic value  $T_b > T_{ad}$ . In propane, we observe the opposite trend. A sub-adiabatic temperature is reached  $T_b < T_{ad}$ . In both cases, burned gas density differs from the equilibrium density  $\rho_b^{eq}$ . In hydrogen,  $\rho_b$  is affected by the super-adiabatic flame temperature and takes lower values. In propane,  $\rho_b$  must be overestimated due to a sub-adiabatic flame temperature. This phenomenon is summarized in Table IX.1. This analysis highlights a misestimation in laminar burning velocities determined by  $\frac{\rho_b}{\rho_u} S_f^0$ , and Bradley's  $S_c^0$ . Although, when stretch is null, the adiabatic

Fuel	Lewis Number	Temperature	$\rho_b$
Hydrogen	$Le < 1$	$T_b > T_{ad}$	$\rho_b < \rho_b^{eq}$
Propane	$Le > 1$	$T_b < T_{ad}$	$\rho_b > \rho_b^{eq}$

Table IX.1: Misestimation of the burned gas density due to stretch and Lewis number effects

temperature is recovered so that burned gases are at the equilibrium, it is absolutely not true during the expansion phase. This phenomenon must be taken into account along with the one observed in Chapter VII. We showed that it takes gases some time to reach the equilibrium, which can induce misestimations. The adiabatic isothermal reference differs from the one used for measurements ( $T=600$  K). This gap is clearly amplified when burned gas density is not at the equilibrium during the expansion phase because of the effect of curvature on temperature. An estimation of  $\rho_b$ , calculated and corrected by the effect of stretch on flame temperature is proposed for propane. Graph IX.6 shows the evolution of  $\rho_b$  against stretch. For high-stretch rates, a miss estimation of about 2.8% is observed.

We can therefore analyze the impact of stretch velocity formulations  $-\frac{\rho_b}{\rho_u} S_f$  and Bradley's

(a)  $\rho_b$  stretch corrected

(b) Temperature stretch corrected

Figure IX.6: Stretch effect on temperature and burned gases density

$S_c$ . Graph IX.7 shows their evolution against stretch. Misestimating burned gas density leads to erroneous Markstein lengths.

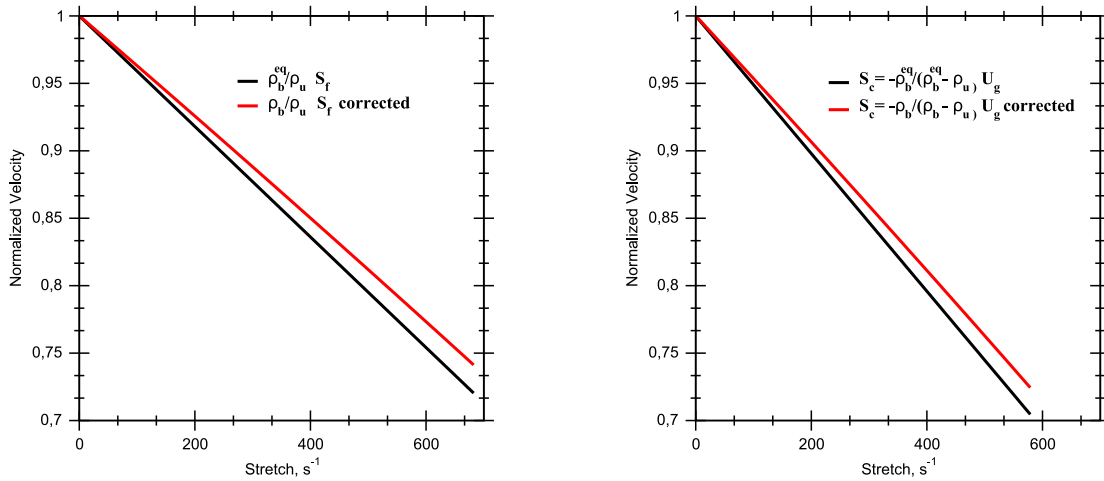
We can conclude that the only experimental way to determine laminar burning velocity is



the displacement speed formulation. Other situations illustrate this finding.

- Gas compression due to pressure rise. Applying the perfect gas law, an increase of pressure, even small, changes both fresh and burned gases densities.
- Radiative effects. Fresh gases are preheated by re-absorption of emitted radiation (highly diluted  $CO_2$  fuels).

These two phenomena – pressure and radiation – can be integrated by the displacement speed method that enables measurements in real conditions. However, in order to establish a comparison with previous studies, these expressions  $-\frac{\rho_b}{\rho_u} S_f$  and Bradley's  $S_c$  – are kept in their original form.



(a)  $\frac{\rho_b}{\rho_u} S_f$ , corrected or not by stretch effects

(b)  $S_c$  from Bradley's model, corrected or not by stretch effects

Figure IX.7: Impacts of stretch on the velocities estimation of  $\frac{\rho_b}{\rho_u} S_f$  and  $S_c$  from Bradley model

## IX.2 Markstein lengths

In this section, we will analyze the effect of Lewis number Markstein lengths. We will expose Markstein lengths associated with burned gases –  $L_b$  –, fresh gases –  $L_u$  – and consumption speed –  $L_c$ .

- Burned gas Markstein length

Graph IX.8 shows a comparison of  $L_b$  with literature. We observe a good agreement with previous measurements for the three gases.

Next graph IX.9 shows the evolution of  $L_b$  for the three gases – hydrogen, methane and

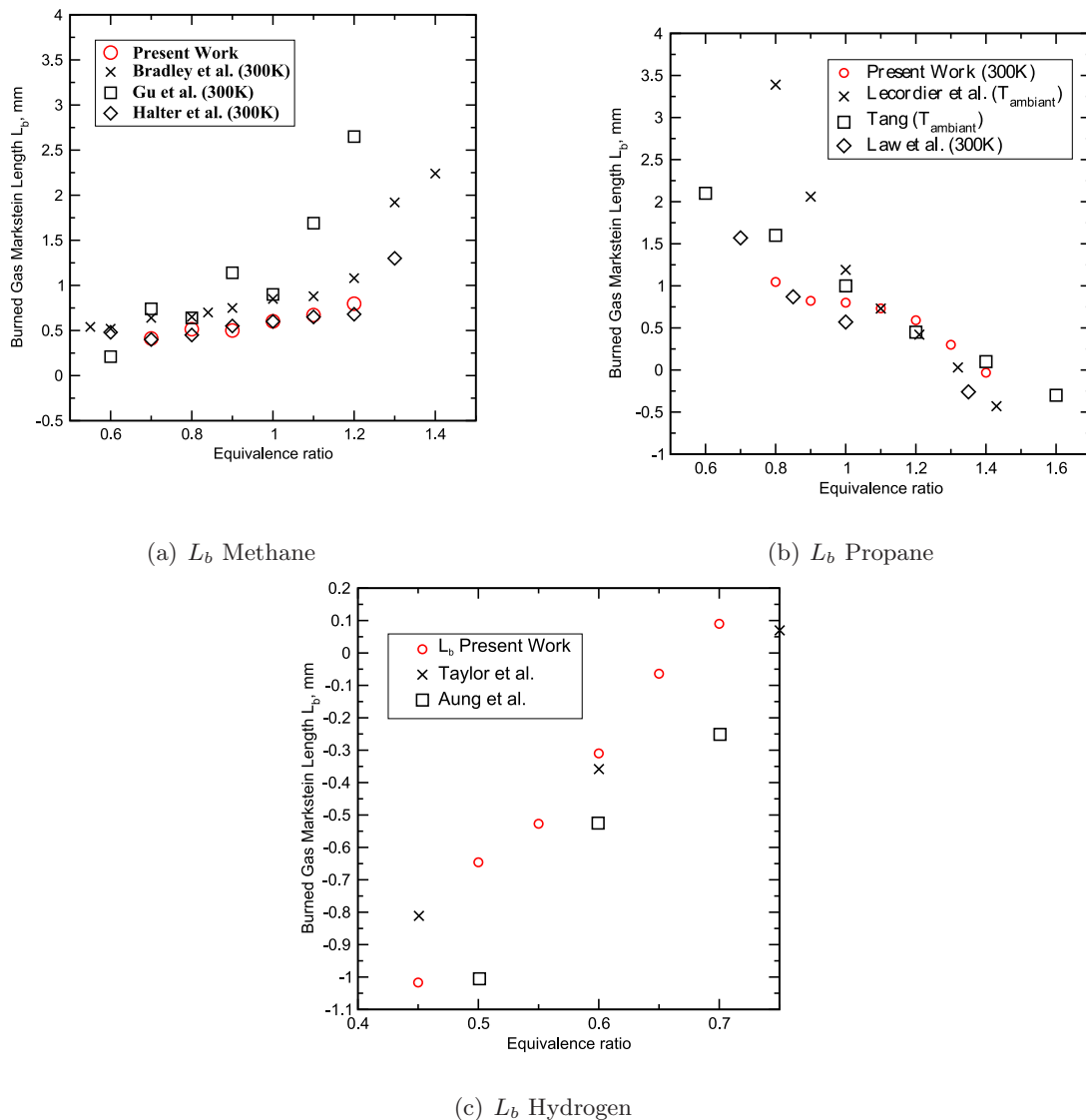


Figure IX.8: Methane, Propane and Hydrogen Markstein length,  $L_b$ , mm. Literature References: Methane: Bradley *et al.* [28], Gu *et al.* [35], Halter *et al.* [59]. Propane: Lecordier *et al.* [75], Tang *et al.* [93], Law *et al.* [94]. Hydrogen: Taylor *et al.* [95], Aung *et al.* [88].

propane – plotted against their Lewis numbers. We draw two major conclusions.

- For both propane and methane,  $L_b$  are positive whereas they are negative for hydrogen. We find a critical  $Le_c$  between [0.8-1] that ensures a positive ( $Le > Le_c$ ) or negative  $Le < Le_c$  value of  $L_b$ . This result corresponds to the analytical formulation presented in III.14, which demonstrates the existence of a critical Lewis number and its dependence on the sign of  $\beta(Le - 1)$ .
- For hydrogen, methane and propane, we observe that increasing Lewis number causes  $L_b$  to increase. For hydrogen, increased Lewis number tends to minimize the effect of stretch on the flame's speed. On the contrary, for propane and methane, increased Lewis numbers induce a higher sensitivity to stretch.

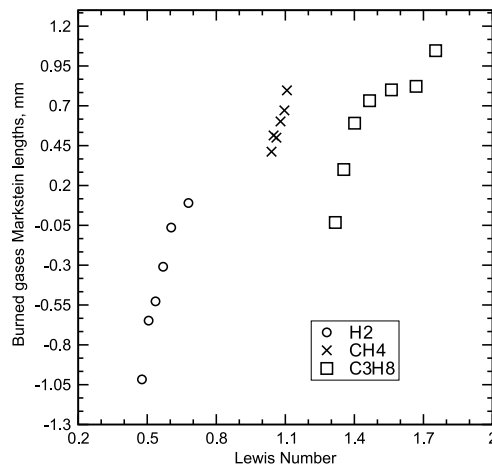


Figure IX.9: Evolution of  $L_b$  for the three gases against Lewis number

- **Fresh gas Markstein length**

Graph IX.11 shows the evolution of  $L_u$  against Lewis number for hydrogen, methane and propane. We only observe negative values of  $L_u$ . In his study ([28]), Bradley had already reported negative values of  $L_u$  whatever the equivalence ratio. As illustrated by Bradley's graph IX.10, positive slopes of  $u_n$  against stretch  $-\kappa$  correspond to negative values of  $L_u$  (Linear extrapolation III.10).

However,  $L_u$  is found to be negative (and not positive, as was expected in the asymptotic developments) even for Lewis numbers inferior to a critical value (case of hydrogen), which contradicts Clavin's theory [63] (III.11). Such a contradiction results from the reference

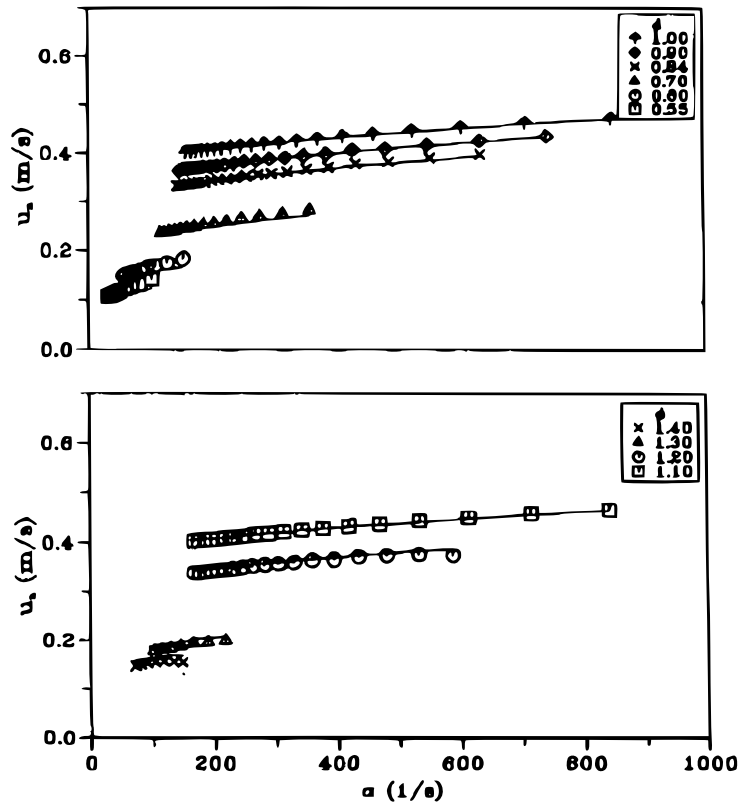


Figure IX.10: Evolution of the displacement speed  $u_n$  with stretch for methane case. From [28].

isothermal that was used for data extraction. As reported in Davis *et al.* or Baillot *et al.*, [70, 66], a fresh gas isothermal – entrance of the preheat zone – yields negative values of  $L_u$ . In theoretical approach,  $L_u$  is determined at the reaction layer, which yields positive values of  $L_u$  (see graph IX.12. Note that this figure has been obtained simulating counterflow flames.

- **Consumption speed Markstein lengths**

Next graph IX.13 shows the evolution of  $L_c$  against Lewis numbers for our three gases.

The following can be observed:

- $L_c$  varies in a very short range whatever the Lewis number considered. This shows that consumption speed's sensitivity to stretch is, for a given gas, quite constant, as is verified for methane.
- Consumption speed's sensitivity to stretch is almost 2 to 5 times inferior to that of

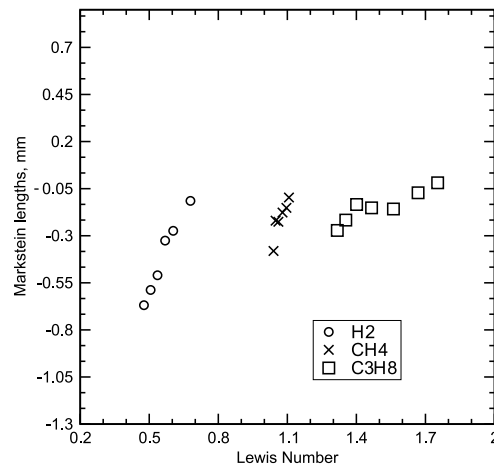


Figure IX.11: Evolution of  $L_u$  for the three gases against Lewis number.

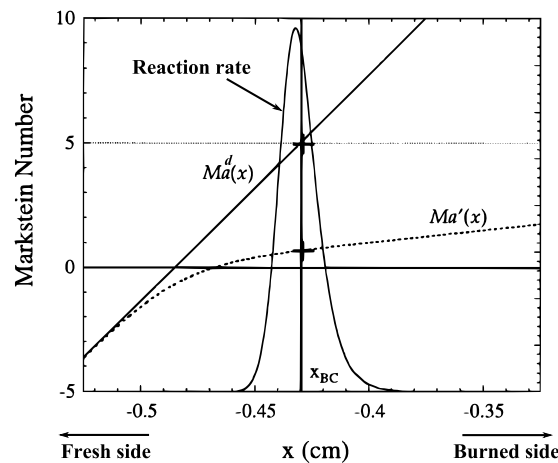


Figure IX.12: Variation of Markstein numbers,  $Ma' = \rho_b/\rho_u Ma^d$  and  $Ma^d$ , across the flame front

displacement speed  $u_n$  or flame speed  $S_f$ .

- Graph IX.14 shows, for methane, a comparison between Bradley's  $L_c$  values [28] and those obtained in this experimental study. Note that both approaches rely on  $u_g$ . We observe a remarkable match – including on both the rich and lean side – and  $L_c$  is found to be minimal close to stoichiometry. These results corroborate the direct measurement method developed in this study. This method allows an accurate prediction of both the unstretched pointed value and the gradient, whatever the equivalence ratio. We conclude that fresh gas velocity is accurately estimated, both

experimentally and numerically.

- Contrary to the theory (III.17),  $L_c$  does not change sign for unity critical Lewis numbers. However, consumption speed formulation is based on a model exposed in Chapter IV. Previously (VIII), we compared two models (Poinso's and Bradley's) that yield totally different  $L_c$  values in terms of sign and evolution. As a result, a comparison with the theory is not possible for  $L_c$  completely depends on the model considered.

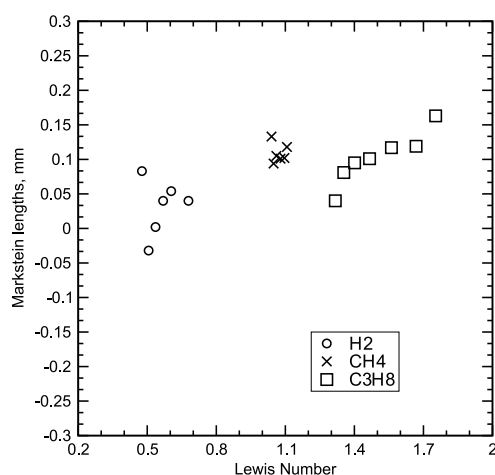


Figure IX.13: Evolution of  $L_c$  for the three gases against Lewis number

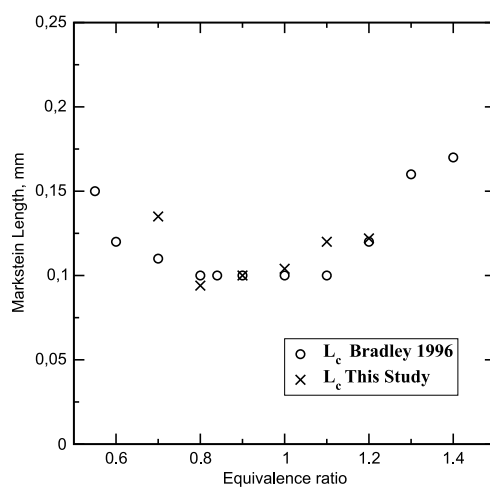


Figure IX.14: Evolution of  $L_c$  from Bradley computations [28] compared to this study in respect with equivalence ratio.  $CH_4$ /Air Flame  $P=0.1$  MPa,  $T=298$  K

### IX.3 Conclusion

We carried out an analysis and determined the dependence of three burning velocity formulations

$$-u_n = S_f - u_g, \frac{\rho_b}{\rho_u} S_f \text{ and } S_c = -\frac{\rho_b^{eq}}{\rho_b^{eq} - \rho_u} (u_g) - \text{ on the Lewis number.}$$

We found, for methane –  $Le \approx 1$  – a very good agreement between Bradley’s computations ([28]) and those obtained experimentally for both unstretched velocity and  $L_c$ . Bearing in mind that both approaches rely on  $u_g$ , we conclude that, both experimentally and numerically, the evolution of fresh gas velocity against stretch is accurately reproduced.

For off-unity Lewis numbers, the problem of burned gas density is pointed out. For propane –  $Le > 1$  – or hydrogen –  $Le < 1$  – the three velocity formulations do not yield similar values. One possible issue lies in the effect of stretch on flame temperature. For off-unity Lewis numbers, flames can reach respectively sub or super-adiabatic temperatures. Burned gas density diverges from the adiabatic value. We must therefore be very careful when dealing with formulations where burned gas density appears. Their use is clearly restricted to mixtures of near-unity Lewis numbers. Direct measurement method is, in any case, the most adequate solution.





## Chapter X

# Ethanol-Isooctane Blends

The work presented in this chapter corresponds to the article *Pressure effects on laminar burning velocities and Markstein lengths for Isooctane-Ethanol-Air mixtures*, published in Proceedings of the Combustion Institute [22]

Current ecological and political contexts encourage scientists and engineers to find new bio-solutions for sustainable development. Bio-fuels are commonly used in spark ignited (SI) engines (either pure or blended with gasoline) to reduce consumption of fossil energy, pollution and our carbon footprint. Ethanol is one of the major bio-fuels studied for the prevention of engine knocking and the reduction of CO and HC emissions in SI engines [1]. Depending on the expected compression ratios, fuel consumption, and pollutant emissions, ethanol is generally mixed with gasoline at various concentrations. Pollutant emissions are directly linked to laminar flame properties, which are represented by the unstretched laminar burning velocities ( $u_n^0$ ) and Markstein length ( $L$ ), which represents the flame sensitivity to stretch.

In view of these applications, a number of detailed kinetic reaction mechanisms have been developed recently for either pure ethanol [2, 3, 4] or pure isooctane (a gasoline surrogate) [5, 6] or blended fuel [7] and partially validated for a range of experimental data, including flame structure and laminar burning velocity. It is therefore important to include the action of pressure and temperature on the laminar burning velocity of such mixtures for thermodynamical

conditions similar to those encountered in SI engines.

The present work is focused on the analysis of the influence of pressure on the laminar burning velocity and Markstein length (relative to fresh gas) of pure isooctane, pure ethanol, and blended fuels.

Numerous works have shown that the pressure dependence of the laminar burning velocity ( $u_n^0$ ) can be given by:

$$u_n^0(P) = u_n^0(P^0)(P/P^0)^\beta \quad (\text{X.1})$$

where  $P^0$  is the atmospheric pressure. The parameter  $\beta$  is linked to the overall reaction order  $n$  (which is generally lower than 1.5 for hydrocarbon fuels), with  $\beta = n/2 - 1$  [26].

In a constant volume vessel, Gülder [96] studied the pressure dependence of laminar burning velocity of both pure ethanol and isooctane fuels in the range of 0.1 - 0.8 MPa. He found that pressure dependence - related by  $\beta$  exponent - is fairly independent of equivalence ratios and close to -0.2 for an initial temperature of 350 K. Bradley [97] proposed the characterization of pure ethanol-air flame up to 1.4 MPa in a spherical bomb. He obtained that for pure ethanol,  $\beta$  varies with lean equivalence ratio and stabilizes close to -0.3 for stoichiometric and rich mixtures at an initial temperature of 358 K.

More recently, Marshall *et al.* [98] used a constant volume vessel to determine the burning velocity for isooctane, ethanol and other pure fuels based on pressure and Schlieren data. They studied a range of initial pressures (up to 0.4 MPa) and found that  $\beta$  parameter was a function of the equivalence ratio and increased linearly with  $\phi$  for both ethanol and isooctane. For stoichiometric mixtures,  $\beta$  was evaluated at -0.265 and -0.199 for ethanol and isooctane, respectively. The work of Eisazadeh-Far [99], using a shadowgraphy technique with a cylindrical vessel, returned an exponential parameter for ethanol (valid for  $0.8 \leq \phi \leq 1.1$ ) that increased with the equivalence ratio ( $\beta = -0.22$  at  $\phi = 1$ ).

The literature review highlights that fuel composition and above all equivalence ratio affect the value of  $\beta$  (*i.e.* the overall reaction order) and a large scatter of data is generally observed. One of the major reasons can be attributed to the diversity of the experimental configurations

and to the extraction procedures to zero stretch rate for spherical flames. It is therefore important to note that spherical apparatus is the most used configuration to analyze pressure effect on laminar burning velocity. It allows us to reach high pressures with less difficulties than other experimental configurations such as the heat flux method [100] or impinging jets [101].

For the laminar burning velocity, we choose the displacement speed formulation, instead of the  $\rho$  ratio method Eq. V.1, for the reasons explained in the previous chapter.

$$u_n = S_f - u_g \quad u_n^0 = \lim_{\kappa \rightarrow 0} (S_f - u_g) \quad (\text{X.2})$$

The aim of our study therefore remains threefold:

- Extend the new technique to extract  $u_n^0$  and Markstein length relative to the fresh gas  $L_u$  for pure ethanol, isooctane and blended fuels at high pressure,
- Analyze the pressure dependence of the laminar burning velocity of such mixtures,
- Propose an empirical correlation to express  $u_n^0 = f(\phi, \epsilon, P)$  with corresponding error assessments, where  $\epsilon = n_{eth}/(n_{eth} + n_{iso})$  is the ethanol mole fraction in fuel blend,  $n_{eth}$  and  $n_{iso}$  the mole number of ethanol and isooctane.

Table X.1 summarizes the ranges of equivalence ratios, pressure and mixtures that have been explored in this study. For each experimental condition, experiments were performed five times and all values of laminar burning velocity and Markstein length presented in this paper are averaged on this series of five experiments. It can be seen in Table X.1 that for some equivalence ratio ( $\phi = 1.1$  or  $1.3$ ), the effect of pressure is not complete due to cellular flame front. Throughout the experiments, uncertainties are estimated at approximately  $\Delta T/T = 0.5\%$  and  $\Delta P/P = 0.5\%$ . The accuracy of the mass flow controller gives an uncertainty on the equivalence ratio of  $\Delta\phi = 0.01$ .

The principal difficulty of this technique to measure  $u_n^0$  (Eq. X.2) lies with the accuracy of the fresh gas velocity measurement near the preheat zone of the flame front, which has a thickness of less than a millimeter. A specific post-processing algorithm of high-speed tomographic images has been achieved to simultaneously measure the flame speed and of the fresh gas velocity at

Equivalence ratio	Pressure MPa	Mixture Type
0.7	0.1	E100-E85
0.8	0.1-1	E100-E85-E50-E20-E0
0.9	0.1	E100-E85-E50-E20-E0
0.9	0.1-1	E100-E0
1	0.1-1	E100-E85-E50-E20-E0
1.1	0.1	E100-E85-E50-E20-E0
1.1	0.2-0.5	E100-E50-E0
1.1	0.6-0.7	E50
1.2	0.1	E100-E85-E50-E20-E0
1.3	0.1	E100-E85-E50-E20-E0
1.3	0.2-0.5	E100-E0
1.4	0.1	E100-E85-E50-E20-E0
1.5	0.1	E100-E85-E50-E20

Table X.1: Experimental conditions explored in this study of laminar burning velocity and Markstein length for specific pressure and mixture types. Mixture Type E100 ( $\epsilon = 1$ ): Pure Ethanol, E85: 85% Eth. in Vol. ( $\epsilon = 0.85$ ), E50: 50% Eth. in Vol. ( $\epsilon = 0.5$ ), E20: 20% Eth. in Vol. ( $\epsilon = 0.2$ ), and E0: pure Isooctane ( $\epsilon = 0$ ).  $T_0 = 373$  K

the entrance of the flame front. The algorithm used to extract these values has been recently detailed and validated in [102]; it is briefly described below. In the case of spherical expanding flames,  $S_f$  is obtained through the temporal evolution of the flame radius ( $dr/dt$ ). The fresh gas velocity profiles up to the isotherm of droplet evaporations ( $T = 580$ K) are determined from two successive tomographic images by using new image post-processing based on two-dimensional cross-correlation algorithm on thin interrogation area. Using this procedure, the fresh gas velocity profile along the normal to the flame front can be recorded from a distance of  $150 \mu\text{m}$  (3 pixels) up to 4 mm (80 pixels). The maximum fresh gas velocity corresponding at

the fresh gas velocity at the entrance of the flame front,  $u_g$ , is obtained by fitting the velocity profile by a polynomial fit. This operation is then repeated for all the propagation time of the flame kernel and a nonlinear extrapolation at zero stretch according to (Eq. X.3) allows us to estimate the unstretched laminar burning velocity  $u_n^0$  and the Markstein length relative to the fresh gas  $L_u$  which characterize the flame response in terms of burning velocity  $u_n$  to the flame stretch.

$$\left(\frac{u_n}{u_n^0}\right)^2 \ln \left(\frac{u_n}{u_n^0}\right)^2 = -2 \frac{L_u \kappa}{u_n^0} \quad (\text{X.3})$$

## X.1 Numerical method

The Cantera software package including full transport properties is used to model 1D adiabatic premixed flames for pure fuels. The transport properties are evaluated by using the mixture averaged diffusion model. Adaptive mesh algorithm has been improved and allows adaptive mesh refinement and de-refinement during the computation. The total final number of grid points is typically 160 for a physical domain of few meters to ensure a chemical equilibrium state in the burned gases.

Ethanol/air flames are modeled using the Marinov mechanism [2] from the Lawrence Livermore National Laboratory (LLNL) and the Saxena and Williams mechanism [4]. The version of Marinov mechanism consists of 351 reversible reactions among 56 species and the version of Saxena mechanism consists of 288 elementary steps among 57 chemical species. Isooctane/air flames are modeled using the Jerzembeck mechanism [5] involving 669 reactions and 99 species. In the present work, the modeling is used mostly to compare the new set of experimental results with those predicted by the calculations for pure fuels. From the laminar burning velocities calculating using these mechanisms, the power exponent  $\beta$  is also derived according to the equivalence ratio.

## X.2 Correlation description

One of the objectives of this work is to provide a general expression for a correlation of laminar burning velocity, validated for a large range of experimental conditions: equivalence ratio,  $\phi$ , pressure,  $P$ , and ethanol mole fraction,  $\epsilon$ , in fuel mixtures. We construct the correlation according to the following steps. First, the effect of equivalence ratio is taken into account in Eq. X.4 for pure fuels, by using an extended formulation of Metghalchi and Keck [103].

$$u_n^0(\phi) = u_{n,\phi=1}^0 + u_{n,1}^0(\phi - 1) + u_{n,2}^0(\phi - 1)^2 + u_{n,3}^0(\phi - 1)^3 + u_{n,4}^0(\phi - 1)^4 \quad (\text{X.4})$$

where  $u_{n,\phi=1}^0$  is the laminar burning velocity at  $\phi = 1$  and  $u_{n,i}^0$  the parameters to be determined for initial temperature  $T^0$  of 373 K and pressure  $P^0$  of 0.1 MPa. Eq. X.4 can be summarized by the functions  $f$  and  $g$  when applied to pure iso-octane  $u_n^0(\phi)_{iso} = f(\phi)$  and pure ethanol  $u_n^0(\phi)_{eth} = g(\phi)$ .

The next step consists in determining the pressure dependence of the laminar burning velocity. The classical exponential decrease is chosen and presented for pure isooctane and ethanol:

$$u_n^0(\phi, P)_{iso} = f(\phi)[P/P_0]^{\beta_{iso}(\phi)} \quad (\text{X.5})$$

$$u_n^0(\phi, P)_{eth} = g(\phi)[P/P_0]^{\beta_{eth}(\phi)} \quad (\text{X.6})$$

The dependency of  $\beta$  parameters on fuel (isooctane, ethanol or blended mixtures) and equivalence ratio is not straightforward and must be evaluated according to the experimental data provided along this work.

The influence of ethanol mole fraction in the fuel blend can then be taken into account. In a recent work [101], Ji and Egolfopoulos have proposed a correlation for burning velocity for binary liquid fuel mixtures. Indeed, a phenomenological analysis suggests that the laminar flame speeds of binary fuel mixtures can be estimated with satisfactory accuracy, by knowing the laminar flame speeds and the adiabatic flame temperatures of the neat fuel components. Assuming that the adiabatic temperature of each pure fuels is identical, the correlation can be expressed by (Eq. X.7):

$$u_n^0(\phi, P, \epsilon) = \exp\left[(1 - \epsilon)\ln(u_n^0(\phi, P)_{iso}) + \epsilon\ln(u_n^0(\phi, P)_{eth})\right] \quad (\text{X.7})$$

### X.3 Results and discussion

#### X.3.1 Results for atmospheric fuel/air flames

Laminar burning velocities for ethanol and isooctane/air flames obtained with the new method discussed in Eq. X.2 are presented in Fig. X.1 and Fig. X.2. Presented data are compared with those obtained in literature for various geometrical configurations: from expanding flame with non-linear extrapolation to zero stretch [84, 59], from expanding flame with linear extrapolation to zero stretch [97], from symmetric twin flames in opposed jet configuration [101], from heat flux method [100] and from the combustion mechanism at a constant temperature of 373 K. It is worth noting that the results of the literature have not been recorded exactly at the same temperature. In order to have a relevant comparison with our data, these data are corrected by using the following correlation  $u_n^0(T) = u_n^0(T^0)(T/T^0)^\alpha$ , where  $T^0 = 298$  K at  $P = 0.1$  MPa. The parameter  $\alpha$  is obtained from [3] and [98] for ethanol and isooctane/air flames, respectively. Error bars on our experimental results are also reported in the figures. The maximum deviation between all our 5 measurements for the same experimental conditions is less than 1.5 cm/s, which is typically of the order of the symbols size. Globally, a good agreement is found between all the data. A deeper analysis can underline slightly laminar burning velocities than [84, 59] whereas the experimental configuration and the extrapolation method to zero stretch are similar. This behavior has been already observed previously for propane [75] and for ethanol [102]. This could be explained by the equilibrium state of the burned gases which can not be reached for such expanding flames with these recorded propagation times, whereas equilibrium calculations are generally used to compute the burned gas density  $\rho_b$  to use Eq. V.1. The ethanol combustion mechanism of Marinov [2] is in good agreement with our data for lean and stoichiometric ethanol/air flames, whereas a strong disagreement can be found for rich flames. In the following, the comparison with this mechanism will be limited to leaner equivalence ratio

than 1.1. However, for rich flames, a better agreement is found with our experimental data and the combustion mechanism of Saxena and Williams [4] which will be preferentially used in this case. For isooctane/air flames, the combustion mechanism of Jerzembeck [5] shows also a very

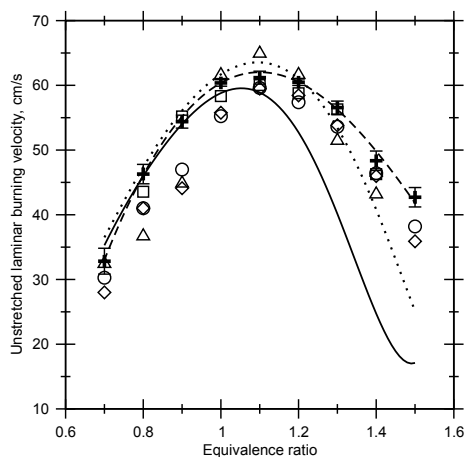


Figure X.1: Laminar burning velocities of ethanol/air flames at atmospheric pressure and temperature of 373 K. Plus: Present Work (Eq:X.2); diamonds: [100]; squares: [84]; circles: [97]; triangles: [104]. Solid line: modeling using the Marinov mechanism at 373 K. Point line: modeling using the Saxena mechanism at 373 K. Dashed line: correlation (Eq. X.4).

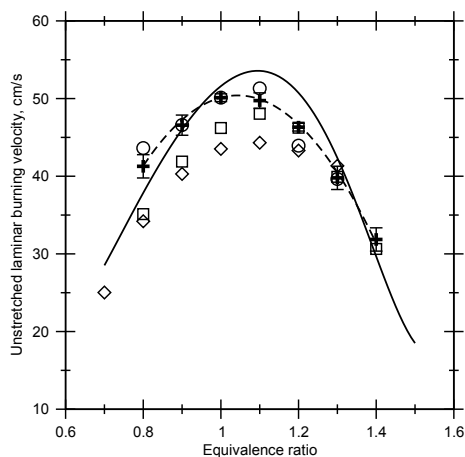


Figure X.2: Laminar burning velocities of isooctane/air flames at atmospheric pressure and temperature of 373 K. Plus: Present Work (Eq:X.2); diamonds: [98]; squares: [84]; circles: [97]. Solid line: modeling using the Jerzembeck mechanism at 373 K. Dashed line: correlation (Eq. X.4).



close performance with our data. Coefficients of Eq. X.4 are determined for each fuel from the experimental results by using a least square fit method. They are listed in Table X.2 and are valid for the ranges of  $\phi \in [0.7; 1.4]$ .

	Ethanol	Isooctane
$u_{n,\phi=1}^0$	60.36	50.12
$u_{n,1}^0$	33.52	12.85
$u_{n,2}^0$	-187.01	-165.74
$u_{n,3}^0$	50.49	2.28
$u_{n,4}^0$	90.89	112.06

$\beta$	$\beta(1)$	$\beta(2)$	$\beta(3)$
	-0.27	-0.145	-1.750

Table X.2: Correlation parameters  $u_{n,i}^0$  from Eq. X.4 and  $\beta(i)$  from Eq. X.8.

The effect of mole fraction,  $\epsilon$ , is reported in Fig. X.3 for  $\epsilon$  varying from 0 to 100%. If the most obvious effect of the increase of  $\epsilon$  is the global increase of the laminar burning velocity of the blended fuel in comparison with the pure isooctane/air flame, its intensity is strongly dependant of the equivalence ratio of the mixture. Indeed for rich flames  $\phi = 1.4$ , the laminar burning velocity varies from 31.9 cm/s for  $\epsilon = 0$  to 48.3 cm/s for  $\epsilon = 1$ , whereas this difference is reduced for lean flames and quasi equal to zero for  $\phi = 0.7$ . The Markstein length relative to the fresh gas  $L_u$  directly determines the sensitivity of the laminar burning velocity  $u_n$  to flame stretch. In Fig. X.4,  $L_u$  of pure and blended fuels are plotted against equivalence ratio. Most of the Markstein lengths are negative (excepted for  $\phi$  lower than 0.8), which means that the burning velocity decreases when the flame stretch decreases. The same evolution of  $L_u$  is observed for equivalence ratios lower than 1.1, irrespective of the mixture composition, whereas significant differences are found for values above 1.1. For rich mixtures,  $L_u$  for pure ethanol differs noticeably from that of isooctane, with a slight decrease of  $L_u$  following the addition of isooctane. This means that a pure isooctane flame is much more sensitive to stretch than an ethanol flame at these equivalence ratios. The flame speed trend is inverted with respect to

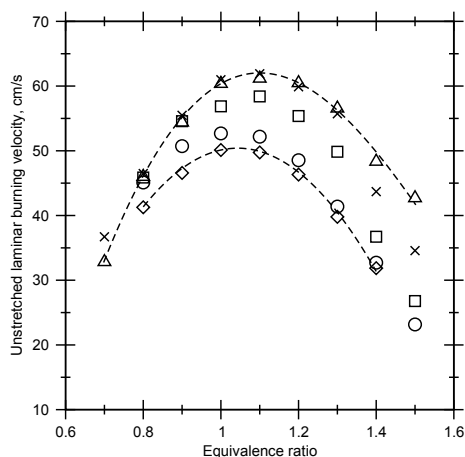


Figure X.3: Laminar burning velocities of ethanol/isooctane/air mixtures at atmospheric pressure and temperature of 373 K for different ethanol mole fraction  $\epsilon$ . Symbols: experiments, dashed lines: correlation for pure fuels. Triangles up: E100; cross: E85; squares: E50; circles: E20; diamonds: E0.

stretch (negative values of  $L_u$ ) for low equivalence ratios of approximately 0.9.

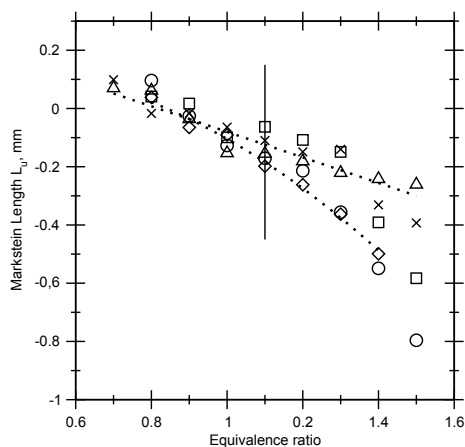


Figure X.4: Variations of Markstein length relative to fresh gas ( $L_u$ ) with equivalence ratio at atmospheric pressure and temperature of 373 K for different ethanol mole fraction  $\epsilon$ . Symbols: experiments, dashed lines: correlation for pure fuels. Triangles up: E100; cross: E85; squares: E50; circles: E20; diamonds: E0.

### X.3.2 Pressure effect

The following section describes the influence of pressure on laminar burning velocities with respect to equivalence ratios and blends. Fig. X.5 shows the relationship between the decrease of laminar burning velocity and pressure in a log-log plot for stoichiometric mixtures. Data are normalized to their corresponding laminar burning velocity at atmospheric pressure. Error bars, obtained from the min/max values of the five experiments for each condition, are also reported for a representative condition (E100). It is worth noting that experimental uncertainty increases with pressure to reach  $\pm 3$  cm/s at 1 MPa. Indeed, increasing the pressure leads to less repeatable measurements due to cellular effects which can appear at high pressure on small part of the flame front (less than 25%, otherwise experiment is removed). Even if these zones are not used for the  $u_n^0$  determination, they may affect the repeatability. The expected exponential decrease is observed with a linear fit in Fig. X.5. Similar behaviors are observed for other conditions ( $\phi = [0.8; 0.9 \text{ and } 1.1]$ ), with no obvious dependence of the mixtures (pure or blended fuels). To quantify these evolutions, a non-least square fit method is used to find the  $\beta$  parameter. Table X.3 and Fig. X.6 show the corresponding  $\beta$  values as a function of equivalence ratio and mixture. These parameters illustrate that the pressure dependence of the laminar burning velocity is rather a function of the equivalence ratio, and the mixture type has no quantifiable influence. Simultaneously, we report also the value of  $\beta$  obtained in literature, and we see globally a good agreement with Marshall *et al.* [98] for lean and stoichiometric ethanol/air flames and with Bradley *et al.* [97]. Although the range of equivalence ratio covered by the experiments is relatively restricted (at higher equivalence ratio, the flame becomes unstable as the pressure increases and does not keep its spherical shape), the data underlines the minimum in  $\beta$  for stoichiometric mixtures, as it was also reported by Bradley *et al.* [97]. To complete this finding, the laminar burning velocities calculated using the Marinov [2], the Saxena [4] and the Jerzembeck [5] mechanisms are processed to derive the power exponent  $\beta$  (Figures X.5 and X.6). The non-linear behavior with the equivalence ratio is also numerically observed with a minimum close to the stoichiometry. For ethanol/air flames, a very good agreement with experimental data is found for the range of the investigated equivalence ratio. More detailed investigations

would be required with other combustion mechanisms to assess this fuel composition impact. From the experimental data, Eq. X.5 and Eq. X.6 can be simplified with  $\beta_{iso}(\phi) = \beta_{eth}(\phi) = \beta(\phi)$  and an expression of  $\beta$ , independent of  $\epsilon$ , can be proposed:

$\phi$	E100	Marinov mech.	$\phi$	E100	Saxena mech.	$\phi$	E0	Jerzembeck mech.
-	-	-	0.7	-	-0.380	-	-	-
0.8	-0.31	-0.318	0.8	-0.31	-0.328	0.8	-0.31	-0.24
0.9	-0.29	-0.295	0.9	-0.29	-0.308	0.9	-0.30	-0.23
1	-0.26	-0.280	1	-0.26	-0.300	1	-0.27	-0.23
1.1	-0.32	-0.29	1.1	-0.32	-0.312	1.1	-0.29	-0.24
-	-	-	1.2	-	-0.344	-	-	-

Table X.3: Dependence of pressure parameter  $\beta$  with equivalence ratio (Eq. X.4).

$$\beta(\phi) = \beta_1 + \beta_2(\phi - 1) + \beta_3(\phi - 1)^2 \quad (\text{X.8})$$

The values of  $\beta_i$  are listed in Table X.2. This correlation remains similar to Metghalchi and

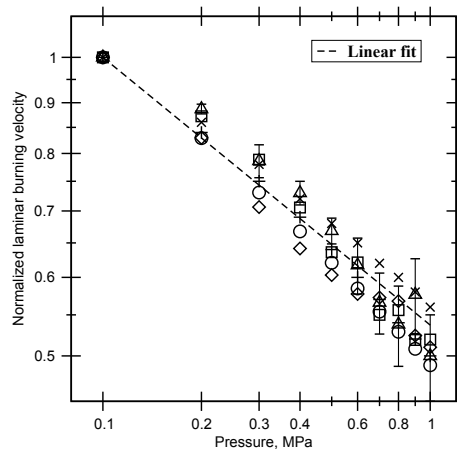


Figure X.5: Log-log scatter-plot of normalized laminar burning velocities  $u_n(\phi, P)/u_n(\phi, P^0)$  up to 0.1 MPa, for stoichiometric condition.  $T = 373$  K. Symbols: experiments, dashed line: linear fit. Triangles up: E100; squares: E50; diamonds: E0; plus: Marinov mechanism [2]; circles: Saxena mechanism [4]; cross: Jerzembeck mechanism [5].

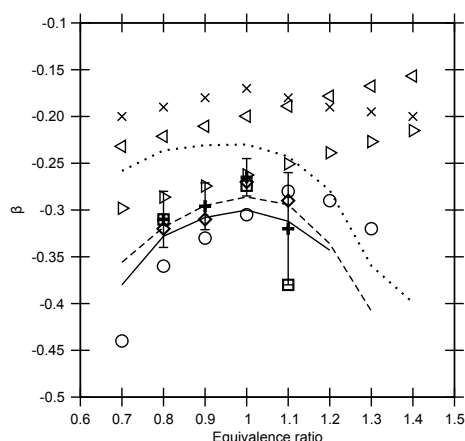


Figure X.6:  $\beta$  parameter as a function of equivalence ratio. Symbols: experiments, dashed lines: kinetic mechanisms. Plus: E100; squares: E50; diamonds: E0; circles: [97]; cross: [96]; triangles right: E100 [98]; triangles left: E0 [98]. Dashed line: Marinov mechanism [2]; solid line: Saxena mechanism [4]; point line: Jerzembeck mechanism [5].

Keck [103] who proposed a linear formulation, but a quadratic term is required to take into account this equivalence ratio dependence, which is also observed numerically.

Markstein lengths  $L_u$  have also been calculated with respect to pressure increase. Fig. X.7 shows the variation of  $L_u$  depending on pressure at  $\phi = 1$ . Whatever the fuel composition, a global and strong decrease of  $L_u$  is observed to reach highly negative value for pressure values less than 0.5 MPa. That means the higher the pressure, the higher the burning velocity sensitivity to stretch. In those cases, the flame was increasingly susceptible to any sources of perturbation, which inevitably led to cellular behavior with respect to pressure. These trends were also observed for the Markstein length relative to the burned gases for methane/air flames [31]. For higher pressure, the evolution remains less sensitive to pressure for all the mixtures studied in this work. This change in the slope was also reported for isooctane and methane by Gu *et al.* [35] for the Markstein length relative to the burned gases at a constant temperature of 358 K.

### X.3.3 Correlation validation

The last objective of this work was to demonstrate the performance of a new laminar burning velocity correlation for a large range of pressure, equivalence ratio and ethanol mole fraction in

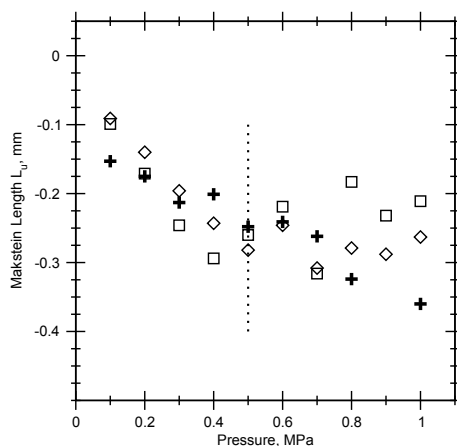


Figure X.7: Variations of stoichiometric Markstein length relative to fresh gas ( $L_u$ ) with pressure up to 1 MPa.  $T = 373$  K.  $\phi = 1$ . Plus: E100; squares: E50; diamonds: E0.

isooctane. All the coefficients of the correlation determined by fitting our experimental results are listed in Table X.2. Validity is ensured for ranges of equivalence ratio  $\phi = [0.7 ; 1.4]$  and pressure up to 1 MPa for a constant temperature of 373 K. The overall accuracy of the correlation is shown on Fig. X.8. In this figure, we report the calculated burning velocity,  $u_{n,corr}^0$ , with the experimental burning velocity,  $u_{n,exp}^0$ . The uncertainties of the correlation based from the  $2\sigma$  intervals ( $2 \times 1.8 = 3.6$  cm/s) of the residue  $\Delta S_L^0 = (u_{n,exp}^0 - u_{n,corr}^0)$  are reported in Fig. X.8 (dashed lines:  $\pm \sigma$ ). This can be compared to experimental uncertainties evaluated from the min/max of the series of 5 experiments, varying from less than 1.5 cm/s at  $P = 0.1$  MPa and close to 3 cm/s at 1 MPa. These experimental uncertainties are similar to the  $2\sigma$  intervals of the correlation which demonstrate the reliability of the correlation.

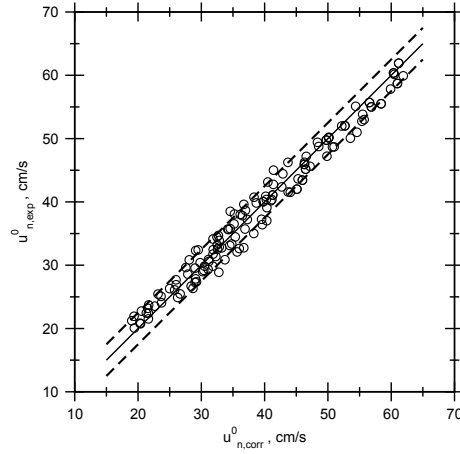


Figure X.8: Burning velocity obtained by correlation compared with the experimental data. Dashed lines indicate  $2\sigma$  uncertainties interval obtained from the residual  $\Delta S_L^0$  distribution. Solid line:  $u_{n,corr}^0 = u_{n,exp}^0$ .

## X.4 Conclusion

Based from a new tool for extracting the laminar burning velocity from the flame speed and the local fresh gas velocity at the entrance of the flame front, experiments have been conducted to evaluate the influences of pressure, equivalence ratio and ethanol mole fraction on isooctane/air flames on laminar burning velocity. This approach gives additional information in terms of flame sensitivity to flame stretch represented by the Markstein length relative to the fresh gases  $L_u$  and a direct measurement of the unstretched laminar burning velocity without any assumptions on adiabaticity and on the fuel mixture properties. The overall accuracy of the measurements obtained from the repeatability of the experiments is less than  $\pm 1.5$  cm/s at  $P = 0.1$  MPa and increases with pressure to, reach  $\pm 3$  cm/s at  $P = 1$  MPa.

Fundamental burning velocities and  $L_u$  have been experimentally determined and compared with numerical results. A globally good agreement is obtained with literature data for pure fuels, and with Saxena mechanism [4] for pure ethanol/air mixtures and with Jerzembek mechanism [5] for pure isooctane/air flames.

The effect of pressure on the burning velocity of pure fuel is interpreted using the correlation  $u_n^0(P) = u_n^0(P^0)(P/P^0)^\beta$ . Particular attention has been paid to the effect of equivalence ratio

and fuel blending on the power exponent  $\beta$ . Both experimental and numerical data show the existence of a minimum in  $\beta$  for stoichiometric mixtures and a globally quadratic approximation with  $\phi$ . From the high level of accuracy of the measurements, we demonstrate that  $\beta$  parameter is independent of fuel blending (i.e.  $\epsilon$ ) for ethanol/isooctane/air mixtures.

A general correlation is then proposed to express the effect of pressure, equivalence ratio and ethanol mole fraction in isooctane at a constant temperature of 373 K. The accuracy of this correlation and the ranges of validity are also provided. Therefore, the matrix of experimental conditions should be completed, to include the temperature effect to achieve thermodynamical conditions similar to those encountered in SI engines, which is the objective of further works.



## Part III

# Conclusion & Appendixes



# Chapter XI

## Conclusion

### XI.1 Summary

Even though it has been long studied and investigated, experimental laminar burning velocity still remains a complex problem. Accurate data are needed and different real flame configurations have been developed and improved over the past decades. The present work goes further and proposes to extract burning velocity and its sensitivity to stretch from the classical spherically expanding flame configuration.

The present work aims to solve the following issues:

- What are the formulations of burning velocity and corresponding assumptions/limitations considering the spherically expanding flame configuration?
- How do we clearly measure laminar burning velocity in this configuration?

A thorough literature review has been presented. Theoretically, the exact formulation of laminar burning velocity corresponds to the consumption speed – integral of the reaction rate along the flame brush. Because this is a complex notion, 1D expressions of absolute and displacement flame speeds are given. To determine these velocities, the observer is alternatively positioned on the reference laboratory frame or on the flame front. Velocities are of deep interest because they can be achieved experimentally for real stretched flames. However, determining displacement speed from the spherical configuration is complex, and is therefore the most significant

achievement of this study. This technique enabled us to extract laminar burning velocity without introducing any hypothesis. Concurrently, expressions of the consumption speed are exposed in a theoretical review, along with their respective limitations.

Finally, to conclude this theoretical part, three formulations made it possible to extract laminar burning velocity and its dependence to stretch. The hypotheses and limitations involved are clearly identified.

The experimental setup focuses on describing the combustion chamber that has been designed and equipped for high-speed tomography diagnostic. High pressure and high temperature initial conditions with either gaseous or liquid fuels (vaporized) can be achieved in this particular facility. The evolution of spherically expanding flame in time makes it possible to determine the absolute flame speed. However, in order to measure displacement speed, the fresh gas velocity profile ahead of the flame front must be estimated. Specific post-processing tools have been developed in order to extract this crucial information.

This work provides burning velocity values from three formulations: propagation speed, displacement speed and consumption speed. They are presented as follows:

- The propagation speed formulation,  $S_f$  – mostly used in literature – and displacement speed,  $u_n$  have been investigated. In this work, methane, isooctane and ethanol/air flames have been studied under various experimental conditions in terms of equivalence ratio, temperature and pressure.  $S_f^0$  and  $u_n^0$  unstretched laminar burning velocities have been nonlinearly extracted and results have been compared. The following conclusions are drawn:
  - In methane/air mixtures, propagation speed formulation and displacement speed yield very similar results.
  - Differences appear in isooctane and ethanol/air mixtures.

These differences between both methods are mostly due to burned gas density estimation (computed for burned gases at chemical equilibrium assuming adiabatic combustion). In isooctane and ethanol/air mixtures, burned gases do not reach the chemical equilibrium

state. Due to the finite size of the flame kernels (maximum radius 2 cm), the time or the distance to reach the equilibrium state cannot be achieved in such an experimental configuration. Using an equilibrium solver for the density ratio could produce some errors in these conditions because it would artificially decrease the density ratio, and therefore the unstretched burning velocity. This result indicates that assumptions involved in the standard method – propagation flame speed – may or may not be fully satisfied, depending on the fuel considered.

- The consumption speed formulation has been studied experimentally. Four formulations have been tested and Bradley’s model has been retained for comparison with propagation speed formulation,  $S_f$ , and displacement speed,  $u_n$ .
- Propagation speed, displacement speed and Bradley’s consumption speed model have been compared and their respective sensitivity to stretch have been studied. Three representative fuels have been selected which because their properties would enable us to clearly identify the effects of preferential diffusivity. Methane has been chosen because of its near-unity Lewis number; hydrogen and propane have been chosen because their Lewis numbers are respectively lower and greater than unity. We observe that, for off-unity Lewis numbers, burned gas density estimation is, once again, problematic. For propane,  $Le > 1$ , or hydrogen,  $Le < 1$ , the three velocities do not yield similar values. One possible issue lies in the effect of stretch on flame temperature. For off-unity Lewis numbers, flames can reach respectively sub or super-adiabatic temperatures. Burned gas density diverges from the adiabatic value. We must therefore be very careful when dealing with formulations where burned gas density appears. Their use is clearly restricted to mixtures of near-unity Lewis numbers.
- As a result, the displacement speed formulation was used to study the effect of pressure on burning velocity and Markstein length in isooctane/ethanol blends. A general correlation was proposed to express the effect of pressure, equivalence ratio and ethanol mole fraction ( $\epsilon$ ) in isooctane at a constant temperature of 373 K. Based on highly accurate results, we

demonstrated that  $\beta$  parameter, corresponding to the effect of pressure, does not depend on fuel blending for ethanol/isooctane/air mixtures.

## XI.2 Perspectives

This study provides very useful information on the way to determine burning velocity in a spherically expanding flame configuration. However, some questions and recommendations for further investigation can be proposed.

- Improving the experimental apparatus by increasing the chamber's radius would, quite obviously, lead to better quality experiments and results. In our case, we have been limited to small flame radius ( $\leq 2\text{ cm}$ ) to perform measurements at constant pressure. In addition, a limited maximum flame radius reduces the accuracy of extrapolation to zero stretch. There is, nonetheless, a trade-off in enlarging the chamber's radius because instabilities will appear at large radius, in particular at elevated pressures.
- To provide a full database for kinetics validation, the matrix of experimental conditions concerning the isooctane/ethanol blends should be completed to include the temperature effect similar to these of SI engines.
- In propagation speed formulation, burned gases are assumed to have no motion. Using seeding particles that remain on the burned side (titanium dioxide, aluminum oxide) could enable us to measure and determine the position at which the velocity of gases is null. The entire profile of gases from burned to fresh side could therefore be established. However, using solid particles is experimentally complex, for optical accesses can be fouled and particle density tends to decrease when passing the flame front.
- Because no assumptions are needed to extract burning velocity from the displacement speed formulation, it could be very interesting to apply this technique on highly diluted fuels – EGR (exhaust gas recirculation). These gases are composed of carbon dioxide,  $CO_2$ , carbon monoxide,  $CO$ , and water vapor,  $H_2O$ , which have strong spectral radiation

absorption. Because of the thermal, transport, and chemical effects of these components on the combustion mechanism, real flame temperatures clearly differ from the adiabatic temperature. It is therefore erroneous to calculate unstretched burning velocity using adiabatic assumptions. Such conclusions have been reported in previous studies: Yu *et al.* [85] showed, for instance, that radiation absorption leads to higher flame temperature and burning velocity than adiabatic flame in the case of  $CH_4/CO_2$  mixtures.

- As a last comment, we would like to offer an interesting perspective. It is more a general thought than a real perspective but it could be of interest to compute , for a simple case – methane/air flame, for instance – a full 3D DNS of a spherically expanding flame with detailed chemistry and transport. A comparison between both experimental and numerical results could be a starting point to clearly identify the sources of uncertainties.

Lastly, and despite the growing interest of stretch effects for turbulent modeling, experimentalists and simulation teams should first reach a consensus on the type of flame response to stretch they need to achieve better models.





## Appendix A

# Lewis number calculation

In this section, the role of Lewis number on stretched flame dynamic is discussed. Lewis numbers play a crucial role in the determination of the Markstein lengths and their formulations and calculations must be accurate. In the early stage of the flame, following energy deposit, the flame kernel develops and does not extinguish if the amount of energy is sufficiently high, i.e. if the kernel temperature is higher than that of the adiabatic flame temperature. Concurrently, stretch affects the flame and therefore could also sustain the flame or extinguish it. Analytical approaches studied the dynamics of such constrained flames [105, 62, 44] and more recently, in the case of spherical expanding flame with positive stretch [106, 82, 107]. Once the flame is propagating and no more perturbed by ignition, thermo-diffusive instabilities, due to preferred diffusion between thermal ( $\alpha$ ) and molecular diffusions ( $D$ ), can either stabilize or turn it cellular. Those are intrinsic instabilities due to non-uniform flame temperature field and highlighted by the Lewis number  $Le = \alpha/D$ . Considering the Fig. A.1 as a physical model to explain thermo-diffusive effects on positive stretched flame, it is relevant to investigate Lewis numbers and their action on flame wrinkling.

- $Le < 1$ : Molecular diffusivity is greater than thermal diffusivity  $D > \alpha$ . For convex flame toward the fresh gas, the reactants diffuse towards burned gas faster than heat diffuses towards cold fresh gases. The reactants are heated and the stretched flame's reactivity and velocity are enhanced. It implies that the stretched burning velocity exceeds that of the

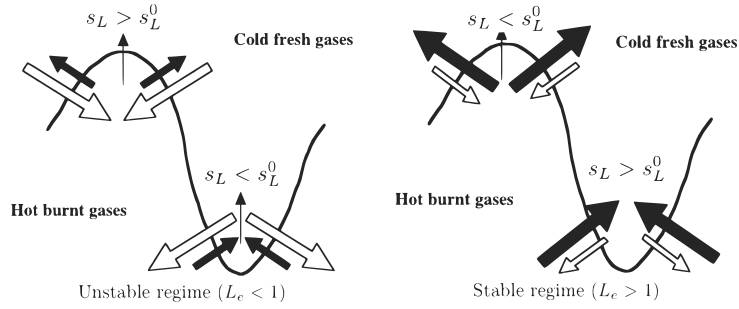


Figure A.1: Sketch of thermodiffusive instabilities from *Poinsot, Veynante* [26]

unstretched one. On the contrary, reactivity is expected to decrease on negatively curved flames.

- $Le > 1$ : In this case, reactants and heat diffuse so that if wrinkles appear, the phenomenon is aborted and the flame stabilizes.

Lewis numberplay an important role on flame development and stabilization. Determination of Lewis numbersrelative to fresh gases requires specific attention, and is described in the subsection below.

## A.1 Lewis number calculation

The first step to determine Lewis numberreactant calculation consists in determining the values of the ternary mixture  $Fuel - O_2 - N_2$  as:  $Le_{mix} = \alpha_{mix}/D_{mix}$  where the species involved are Fuel,  $O_2$  and  $N_2$  with respectively pure Lewis numbers:  $Le_F$ ,  $Le_{O_2}$  and  $Le_{N_2}$ . As seen in Eq. A.1,  $\lambda_{mix}$ : thermal conductivity,  $C_{p_{mix}}$ : specific heat value,  $\rho_{mix}$  and  $D_{mix}$  have to be calculated beforehand.

$$Le_{mix} = \frac{\alpha_{mix}}{D_{mix}} = \frac{\lambda_{mix}}{\rho_{mix} C_{p_{mix}} D_{mix}} \quad (A.1)$$

Special attention must be given to  $\lambda_{mix}$  and  $D_{mix}$  estimation. Referring to Kee *et al.* [108], for mixtures,  $\lambda_{mix}$  is expressed as:

$$\lambda_{mix} = \frac{1}{2} \left[ \left( \sum_{k=1}^n X_k \lambda_k \right) + \frac{1}{\sum_{k=1}^n \frac{X_k}{\lambda_k}} \right] \quad (A.2)$$

where  $X_k$  is the mole fraction of species k. Thermal conductivity of pure species,  $\lambda_k$ , have been extracted from empiric correlations established by Le Neindre [109]. For molecular diffusion,

Hirschfelder *et al.* [110] give the relation for a deficient reactant  $k$  diffusing either air or fuel one into the other as well as in  $N_2$  (see Eq. A.3)

$$D_{mix}^k = \frac{1 - Y_k}{\sum_{j \neq k}^n X_j / D_{kj}} \quad (\text{A.3})$$

where  $Y_k$  is the mass fraction of specie  $k$  and  $D_{kj}$  the molecular diffusion of specie  $k$  in  $j$ .  $D_{kj}$  is calculated from [110] with the relation Eq. A.4:

$$D_{kj} = 0.002680 \frac{\sqrt{T^3 (M_k + M_j) / 2 M_k M_j}}{\rho \sigma_{kj}^2 \omega_{kj}^{(1,1)}} \quad (\text{A.4})$$

For ternary mixtures, Lewis number calculation depends on the deficient reactant for of-stoichiometric conditions. If  $\phi \leq 1$ , fuel as a limitant of the reaction and  $D_{mix}^{fuel}$  is calculated. If  $\phi \geq 1$ ,  $D_{mix}^{O_2}$  is calculated. To avoid discontinuity close to the stoichiometric value, the approach of Bechtold *et al.* [11] is used and defined as Eq. A.5:

$$Le_{eff} = 1 + \frac{(Le_E - 1) + (Le_D - 1)A}{1 + A} \quad (\text{A.5})$$

where:  $Le_{D/E}$  are respectively the Lewis numbers of deficient and excess reactants;  $A = 1 + \beta(\theta - 1)$  and  $\beta$  is the Zeldovich number.

Everyone agrees on the calculation of Lewis numbers for ternary mixtures. However, in the case of blended fuels, different approaches could appear in the definition of an *effective blend Lewis number*:  $Le_{eff,blend}$ .

- The recent work of Dinkelacker *et al.* [111] uses a weighted average of fuel Lewis numbers as Eq. A.6

$$\frac{1}{Le_{eff,blend}} = \frac{X_1}{Le_1} + \frac{X_2}{Le_2} \quad (\text{A.6})$$

where  $X_i$  is the mass fraction of  $Fuel_i$  in mixture. Subscript  $i$  can be either isoctane or ethanol.

- $Le_{eff}$  can be calculated using a heat-release weighted approach, as proposed by Law and Kwon [112]

$$Le_{eff,blend} = 1 + [q_{Le_1}(Le_1 - 1) + q_{Le_2}(Le_2 - 1)]/q \quad (\text{A.7})$$

where  $q_{Le_i}$  is the combustion heat release of fuel  $i$  and  $q$  is the total heat release ( $q = \sum_i q_i$ ).

A crucial point is the hypotheses that are involved in the theory development. Most of the time, the theory assumes a one-step reaction where reactants are directly transformed into products. It could yield a Lewis number calculation based on diffusivity (thermal and molecular) of reactants. In real configurations, however, a multiplicity of Lewis numbers can be observed. It is due to complex chemical reactions involving hundreds (or thousands) of species. Care should therefore be taken when comparing result on Markstein lengths or numbers to the theory.

## Appendix B

# Confined spherically expanding flame: a criterion for pressure rise

When a spherical flame expands in a spherical vessel, it is possible to estimate pressure rise in the chamber. It leads to the integration of Eq. IV.6 in the case of an infinitely thin flame thickness. This part will only expose theoretical results. The constant volume chamber technique for laminar burning velocity determination implies a limited pressure rise in the chamber during the combustion process. In fact, if the pressure rises, the thermodynamical initial conditions change (temperature and pressure). Therefore, the pressure rise has to be neglected – burned gas volume is supposed to be null. Fig. B.1, from [57], represents the evolution of normalized flame speed with normalized stretch and corresponding radius ( $R_f/R^0$ ) for a stoichiometric methane/air flame. Three speeds are evaluated: one is corrected by both pressure and temperature rise due to compression, the second one is only corrected by pressure rise and the third one represents the classical method considering constant pressure method. [57, 105] and others studies have derived the equations and found  $R_f/R^0 < 0.3$  to verify that pressure can be the neglected (see Fig. B.1) ( $R_f$  flame radius;  $R^0$  spherical vessel radius).

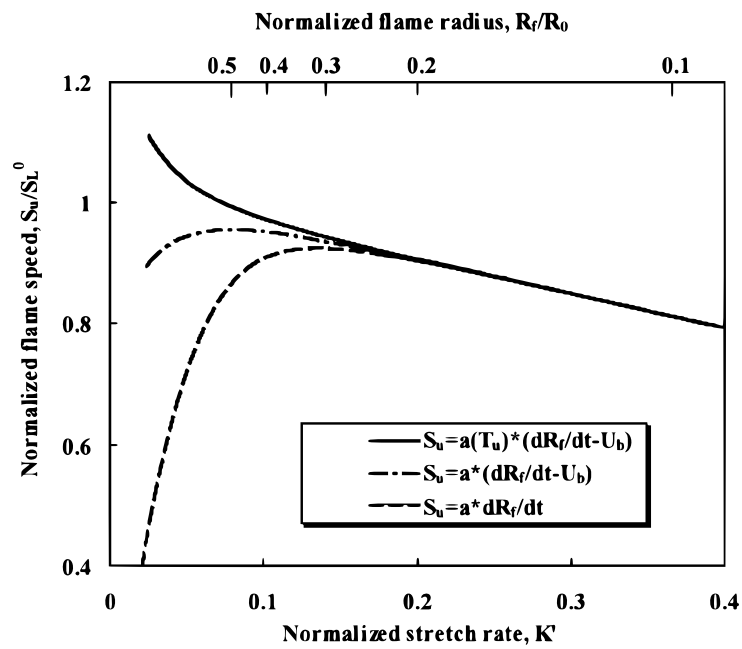


Figure B.1: Normalized stretched flame speed as a function of normalized stretch rate and flame radius for a stoichiometric  $CH_4$ /air flame from [57].

# Bibliography

- [1] W.D. Hsieh, R.H. Chen, T.L. Wu, and T.H. Lin. Engine performance and pollutant emission of an si engine using ethanol-gasoline blended fuels. *Atmospheric Environment*, 36:403–410, 2002. *pages 2 and 133*
- [2] N.M. Marinov. A detailed chemical kinetic model for high temperature ethanol oxidation. *International Journal of Chemical Kinetics*, 31:183–220, 1999. *pages 3, 4, 133, 137, 139, 143, 144 and 145*
- [3] A.A. Konnov. Development and validation of a detailed reaction mechanism for the combustion of small hydrocarbons. *Proceedings of the Combustion Institute*, 28:317–325, 2000. *pages 3, 4, 133 and 139*
- [4] P. Saxena and F.A. Williams. Numerical and experimental studies of ethanol flames. *Proceedings of the Combustion Institute*, 31:1149–1156, 2007. *pages 3, 133, 137, 140, 143, 144, 145 and 147*
- [5] S. Jerzembeck, N. Peters, P. Pepiot-Desjardins, and H. Pitsch. Laminar burning velocities at high pressure for primary reference fuels and gasoline: Experimental and numerical investigation. *Combustion and Flame*, 156:292–301, 2009. *pages 3, 133, 137, 140, 143, 144, 145 and 147*
- [6] H.J. Curran, P. Gaffuri, W.J. Pitz, and C.K. Westbrook. A comprehensive modeling study of iso-octane oxidation. *Combustion and Flame*, 129:253–280, 2002. *pages 3 and 133*

- [7] M. Mehl, H.J. Curran, W.J. Pitz, and C.K. Westbrook. Chemical kinetic modeling of component mixtures relevant to gasoline. In *4th European Combustion Meeting*, Vienna (Austria), 2009. *pages 3 and 133*
- [8] L. Vervisch and D. Veynante. Interlinks between approaches for modeling turbulent flames. *Proceedings of the Combustion Institute*, 28:175–183, 2000. *page 3*
- [9] K.N.C. Bray. Studies of the turbulent burning velocity. *Proceedings of the Royal Society of London A*, 431:315–335, 1990. *page 3*
- [10] J. Tien and M. Matalon. On the burning velocity of stretched flames. *Combustion and Flame*, 84:238–248, 1991. *page 3*
- [11] J.K. Bechtold and M. Matalon. The dependence of the markstein length on stoichiometry. *Combustion and Flame*, 127:1906–1913, 2001. *pages 3 and 159*
- [12] B. Fiorina, R. Vicquelin, P. Auzillon, N. Darabiha, O. Gicquel, and D. Veynante. A filtered tabulated chemistry model for les of premixed combustion. *Combustion and Flame*, 157:465–475, 2010. *page 4*
- [13] V. Subramanian, P. Domingo, and L. Vervisch. Large eddy simulation of forced ignition of an annular bluff-body burner. *Combustion and Flame*, 157:579–601, 2010. *page 4*
- [14] P. Laffitte. La propagation des flammes dans les melanges gazeux. *Hermann et Cie, Actualites scientifiques et industrielles, Paris*, 1939. *page 4*
- [15] E. Mallard and H. Le Chatelier. Sur la vitesse de propagation de l’inflammation dans les melanges explosifs. *Comptes rendus de l’Academie des Sciences, Paris*, 93:145, 1881. *page 4*
- [16] N. Bouvet. Experimental and numerical studies of the fundamental flame speeds of methane/air and syngas ( $h_2/co$ )/air mixtures. *PhD Thesis*, 2010. *pages 5, 36 and 37*
- [17] G.E. Andrews and D. Bradley. Determination of burning velocities: A critical review. *Combustion and Flame*, 18:133–153, 1972. *pages 5, 6, 9, 40 and 52*



- [18] C.K. Law. Combustion at a crossroads: Status and prospects. *Proceedings of the Combustion Institute*, 31:1–29, 2007. pages 6, 42 and 43
- [19] C.K. Wu and C.K. Law. On the determination of laminar flame speeds from stretched flames. *Proceedings of the Combustion Institute*, 20:1941–1949, 1984. pages 6, 42 and 45
- [20] A.P. Kelley and C.K. Law. Nonlinear effects in the experimental determination of laminar flame properties from stretched flames. In *Eastern State Fall Technical Meeting, Chemical & Physical Processes in Combustion*, University of Virginia (US), 2007. pages 6 and 43
- [21] E. Varea, V. Modica, A. Vandel, and B. Renou. Measurement of laminar burning velocity and markstein length relative to fresh gases using a new postprocessing procedure: Application to laminar spherical flames for methane, ethanol and isooctane/air mixtures. *Combustion and Flame*, 159:577–590, 2012. pages 9, 11, 69 and 89
- [22] E. Varea, V. Modica, B. Renou, and A. Boukhalfa. Pressure effects on laminar burning velocities and markstein lengths for isooctane-ethanol-air mixtures. *Proceedings of the Combustion Institute*, *In press*, 2012. pages 11 and 133
- [23] C.K. Law and C.J. Sung. Structure, aerodynamics, and geometry of premixed flamelets. *Progress in Energy and Combustion Science*, 26:459–505, 2000. page 16
- [24] F.A. Williams. *Combustion Theory*. Benjamin Cummings, Menlo Park, CA, 1985. page 17
- [25] R.J. Blint. The relationship of the laminar flame width to flame speed. *Combustion Science and Technology*, 49:79–92, 1986. page 18
- [26] T. Poinso and D. Veynante. *Theoretical and Numerical Combustion*. R.T. Edwards, 2001. pages 18, 24, 27, 57, 58, 134 and 158
- [27] G.P. Smith, D.M. Golden, M. Frenklach, N.W. Moriarty, B. Eiteneer, M. Goldenberg, C.T. Bowman, R.K. Hanson, S. Song, W.C. Gardiner Jr., V.V. Lissianski, and Z. Qin. Gri-mech homepage, gas research institute,. 1999. pages 24, 90 and 91

- [28] D. Bradley, P.H. Gaskell, and X.J. Gu. Burning velocities, markstein lengths, and flame quenching for spherical methane-air flames: a computational study. *Combustion and Flame*, 104:176–198, 1996.  
*pages 27, 45, 53, 56, 93, 100, 102, 104, 120, 121, 126, 127, 128, 129, 130 and 131*
- [29] X. Qin and Y. Ju. Measurements of burning velocities of dimethyl ether and air premixed flames at elevated pressures. *Proceedings of the Combustion Institute*, 30:233–240, 2005.  
*pages 31, 90 and 91*
- [30] Z. Chen, X. Qin, Y. Ju, Z. Zhao, M. Chaos, and F.L. Dryer. High temperature ignition and combustion enhancement by dimethyl ether addition to methane/air mixtures. *Proceedings of the Combustion Institute*, 31:1215–1222, 2007. *pages 31 and 90*
- [31] F. Halter, C. Chauveau, N. Djebaili-Chaumeix, and I. Gokalp. Characterization of the effects of pressure and hydrogen concentration on laminar burning velocities of methane-hydrogen-air mixtures. *Proceedings of the Combustion Institute*, 30:201–208, 2005.  
*pages 31, 90, 91 and 145*
- [32] S.Y. Liao, J. Gao, and Z.H. Huang. Measurements of markstein numbers and laminar burning velocities for natural gas-air mixtures. *Energy & Fuels*, 19:328–328, 2004.  
*pages 31, 90 and 91*
- [33] K. Tanoue, F. Shimada, and T. Hamatake. The effects of flame stretch on outwardly propagating flames. *JSME international journal. Ser. B, Fluids and thermal engineering*, 46:416–424, 2003.  
*pages 31, 90 and 91*
- [34] G. Rozenchan, D.L. Zhu, C.K. Law, and S.D. Tse. Outward propagation, burning velocities, and chemical effects of methane flames up to 60 atm. volume 29, pages 1461–1469, 2002.  
*pages 31, 90 and 91*
- [35] X.J. Gu, M.Z. Haq, M. Lawes, and R. Woolley. Laminar burning velocity and markstein lengths of methane-air mixtures. *Combustion and Flame*, 121:41–58, 2000.  
*pages 31, 90, 91, 126 and 145*

- [36] M.I. Hassan, K.T. Aung, and G.M. Faeth. Measured and predicted properties of laminar premixed methane/air flames at various pressures. *Combustion and Flame*, 115:539–550, 1998. *pages 31 and 90*
- [37] W. Lowry, J. De Vries, M. Krejci, E. Petersen, Z. Serinyel, W. Metcalfe, H. Curran, and G. Bourque. Laminar flame speed measurements and modeling of pure alkanes and alkane blends at elevated pressures. *Journal of Engineering for Gas Turbines and Power*, 133, 2011. *pages 31 and 90*
- [38] T. Tahtouh, F. Halter, and C. Mounaim-Rousselle. Measurement of laminar burning speeds and markstein lengths using a novel methodology. *Combustion and Flame*, 156:1735–1743, 2009. *pages 31, 39, 90 and 91*
- [39] Y. Dong, C.M. Vagelopoulos, G.R. Spedding, and F.N. Egolfopoulos. Measurement of laminar flame speeds through digital particle image velocimetry: Mixtures of methane and ethane with hydrogen, oxygen, nitrogen, and helium. *Proceedings of the Combustion Institute*, pages 1419–1426, 2002. *page 31*
- [40] Y. Huang, C.J. Sung, and J.A. Eng. Laminar flame speeds of primary reference fuels and reformer gas mixtures. *Combustion and Flame*, 139:239–251, 2004. *pages 31, 90 and 91*
- [41] C.M. Vagelopoulos and F.N. Egolfopoulos. Direct experimental determination of laminar flame speeds. *Proceedings of the Combustion Institute*, 27:513–519, 1998. *pages 31 and 122*
- [42] C.M. Vagelopoulos, F.N. Egolfopoulos, and C.K. Law. Further considerations on the determination of laminar flame speeds with the counterflow twin-flame technique. *Proceedings of the Combustion Institute*, 25:1341–1347, 1994. *page 31*
- [43] F.N. Egolfopoulos, P. Cho, and C.K. Law. Laminar flame speeds of methane-air mixtures under reduced and elevated pressures. *Combustion and Flame*, 76:375–391, 1989. *page 31*
- [44] B. Lewis and G. von Elbe. *Combustion, Flames and Explosions of Gases*. Academic Press, 3rd edn. edition, 1987. *pages 31 and 157*

- [45] O. Kurata, S. Takahashi, and Y. Uchiyama. Influence of preheat temperature on the laminar burning velocity of methane-air mixtures. *SAE Technical Paper*, 1994. page 31
- [46] Y. Ogami and H. Kobayashi. Laminar burning velocity of stoichiometric ch<sub>4</sub>/air premixed flames at high-pressure and high-temperature. *JSME international journal. Ser. B, Fluids and thermal engineering*, 48:603–609, 2006. page 31
- [47] L.P.H. de Goey, A. Van Maaren, and R.M. Quax. Stabilization of adiabatic premixed laminar flames on a flat flame burner. *Combustion Science and Technology*, 92:201–207, 1993. page 31
- [48] F.A. Williams. A review of some theoretical combustions of turbulent flame structure. In *AGARD Conference Proceedings*, volume 164, 1975. page 32
- [49] M. Matalon. On flame stretch. *Combustion Science and Technology*, 31:169–181, 1983. pages 32 and 33
- [50] C.K. Law. Dynamics of stretched flames. *Proceedings of the Combustion Institute*, 22:1381–1402, 1989. pages 33, 35 and 36
- [51] L.P.H. De Goey and J.H.M. Ten Thije Boonkamp. A mass-based definition of flame stretch for flames with finite thickness. *Combustion Science and Technology*, 122:399–405, 1997. page 33
- [52] F.N. Egolfopoulos, D.L. Zhu, and C.K. Law. Experimental and numerical determination of laminar flame speeds: Mixtures of c<sub>2</sub>-hydrocarbons with oxygen and nitrogen. *Proceedings of the Combustion Institute*, 23:471–478, 1991. page 36
- [53] D.L. Zhu, F.N. Egolfopoulos, and C.K. Law. Experimental and numerical determination of laminar flame speeds of methane/(ar, n<sub>2</sub>, co<sub>2</sub>)-air mixtures as function of stoichiometry, pressure, and flame temperature. *Proceedings of the Combustion Institute*, 22:1537–1545, 1989. page 36

- [54] P. Clavin and G. Joulin. Premixed flames in large scale and high intensity turbulent flow. *Journal de Physique Lettres*, 44:1–12, 1983. pages 36 and 45
- [55] A. Matynia. *Mise en place d'un dispositif experimental pour l'analyse de la structure de flammes de premelanges a haute pression. Application aux flammes methane/air et biogaz/air*. PhD thesis, 2011. page 37
- [56] A.P. Kelley, G. Jomaas, and C.K. Law. Critical radius for sustained propagation of spark-ignited spherical flames. *Combustion and Flame*, 156:1006–1013, 2009. page 40
- [57] Z. Chen and Y. Ju. Effects of compression and stretch on the determination of laminar flame speeds using propagating spherical flames. *Combustion Theory and Modelling*, 13:343–343, 2009. pages 40, 161 and 162
- [58] L. Selle, T. Poinso, and B. Ferret. Experimental and numerical study of the accuracy of flame-speed measurements for methane/air combustion in a slot burner. *Combustion and Flame*, 158:146–154, 2011. page 41
- [59] F. Halter, T. Tahtouh, and C. Mounaim-Rousselle. Nonlinear effects of stretch on the flame front propagation. *Combustion and Flame*, 157:1825–1832, 2010. pages 43, 79, 90, 97, 126 and 139
- [60] T. Tahtouh, F. Halter, C. Caillol, F. Foucher, and C. Mounaim-Rousselle. Nonlinear effects of stretch on the flame propagation. In *4th European Combustion Meeting*, Vienna (Austria), 2009. pages 43 and 90
- [61] Z. Chen. On the extraction of laminar flame speed and markstein length from outwardly propagating spherical flames. *Combustion and Flame*, 158:291–300, 2011. page 44
- [62] P. Clavin and F.A. Williams. Effects of molecular diffusion and of thermal expansion on the structure and dynamics of premixed flames in turbulent flows of large scale and low intensity. *Journal of Fluid Mechanics*, 116:251–282, 1982. pages 45, 123 and 157

- [63] P. Clavin. Dynamic behavior of premixed flame fronts in laminar and turbulent flows. *Progress in Energy and Combustion Science*, 11:1–59, 1985. *pages 45, 46 and 127*
- [64] B. Deshaies and P. Cambray. The velocity of a premixed flame as a function of the flame stretch: an experimental study. *Combustion and Flame*, 82:361–375, 1990. *page 45*
- [65] A.N. Lipatnikov. Some issues of using markstein number for modeling premixed turbulent combustion. *Combustion Science and Technology*, 119:131–154, 1996. *page 45*
- [66] F. Baillot, D. Durox, and D. Demare. Experiments on imploding spherical flames: Effects of curvature. *Proceedings of the Combustion Institute*, 29:1453–1460, 2002. *pages 45 and 128*
- [67] G. Yu, C.K. Law, and C.K. Wu. Laminar flame speeds of hydrocarbon + air mixtures with hydrogen addition. *Combustion and Flame*, 63:339–347, 1986. *page 45*
- [68] D. Bradley, P.H. Gaskell, and X.J. Gu. The modeling of aerodynamic strain rate and flame curvature effects in premixed turbulent combustion. *Proceedings of the Combustion Institute*, 27:849–856, 1998. *page 45*
- [69] A. Trouvé and T. Poinso. The evolution equation for the flame surface density in turbulent premixed combustion. *Journal of Fluid Mechanics*, 278:1–31, 1994. *page 45*
- [70] S.G. Davis, J. Quinard, and G. Searby. Determination of markstein numbers in counterflow premixed flames. *Combustion and Flame*, 130:112–122, 2002. *pages 45, 46 and 128*
- [71] T. Poinso and D. Veynante. *Theoretical and Numerical Combustion*. Third Edition (www.cerfacs.fr/elearning), 2011. *pages 47, 49, 57 and 58*
- [72] D. Bradley and A. Mitcheson. Mathematical solutions for explosions in spherical vessels. *Combustion and Flame*, 26:201–217, 1976. *page 51*
- [73] A. Bonhomme, L. Selle, and T. Poinso. Curvature and confinement effects for flame speed measurements in laminar spherical and cylindrical flames. *Combustion and Flame*, *In press*, 2013. *page 51*

- [74] L.P.H. De Goey, T. Plessing, R.T.E. Hermanns, and N. Peters. Analysis of the flame thickness of turbulent flamelets in the thin reaction zones regime. *Proceedings of the Combustion Institute*, 30:859–866, 2005. page 58
- [75] S. Balusamy, A. Cessou, and B. Lecordier. Direct measurement of local instantaneous laminar burning velocity by a new piv algorithm. *Experiments in Fluids*, 50:1–13, 2010. pages 78, 80, 97, 121, 122, 123, 126 and 139
- [76] S. Suzuki and K. Abe. Topological structural analysis of digital binary images by border following. *Computer Vision, Graphics and Image Processing*, 30:32–46, 1985. page 79
- [77] A. Razet. Méthode des moindres carrés appliquée au cercle pour une utilisation en interférométrie. *Bulletin du BNM*, 108:39–48, 1997. page 79
- [78] A.P. Kelley and C.K. Law. Nonlinear effects in the extraction of laminar flame speeds from expanding spherical flames. *Combustion and Flame*, 156:1844–1851, 2009. pages 79 and 90
- [79] G.R.A. Groot and L.P.H. De Goey. A computational study on propagating spherical and cylindrical premixed flames. *Proceedings of the Combustion Institute*, 29:1445–1451, 2002. pages 82, 103 and 105
- [80] B. Lecordier. *Etude de l'interaction de la propagation d'une flamme de prémélange avec le champ aérodynamique par association de la tomographie laser et de la PIV*. Phd thesis report, 1997. pages 85 and 86
- [81] C.T. Bowman, R.K. Hanson, D.F. Davidson, W.C. Gardiner, V. Lissianski, G.P. Smith, D.M. Golden, M. Frenklach, and M. Goldenberg. Gri-mech homepage, gas research institute. 1994. pages 90 and 91
- [82] Z. Chen and Y. Ju. Theoretical analysis of the evolution from ignition kernel to flame ball and planar flame. *Combustion Theory and Modelling*, 11:427–435, 2007. pages 91 and 157

- [83] Z. Chen. Effects of radiation and compression on propagating spherical flames of methane/air mixtures near the lean flammability limit. *Combustion and Flame*, 157:2267–2276, 2010. page 97
- [84] G. Broustail, P. Seers, F. Halter, G. Moréac, and C. Mounaim-Rousselle. Experimental determination of laminar burning velocity for butanol and ethanol iso-octane blends. *Fuel*, 90:1–6, 2011. pages 98, 99, 139 and 140
- [85] Y. Ju, G. Masuya, and P.D. Ronney. Effects of radiative emission and absorption on the propagation and extinction of premixed gas flames. *Proceedings of the Combustion Institute*, 27:2619–2626, 1998. pages 99 and 155
- [86] S.K. Marley and W.L. Roberts. Measurements of laminar burning velocity and markstein number using high-speed chemiluminescence imaging. *Combustion and Flame*, 141:473–477, 2005. page 122
- [87] K.J. Bosschaart and L.P.H. de Goey. The laminar burning velocity of flames propagating in mixtures of hydrocarbons and air measured with the heat flux method. *Combustion and Flame*, 136:261–269, 2004. page 122
- [88] K.T. Aung, M.I. Hassan, and G.M. Faeth. Flame stretch interactions of laminar premixed hydrogen/air flames at normal temperature and pressure. *Combustion and Flame*, 109:1–24, 1997. pages 122 and 126
- [89] D.R. Dowdy, D.B. Smith, and S.C. Taylor. The use of expanding spherical flames to determine burning velocities and stretch effects in hydrogen/air mixtures. *Proceedings of the Combustion Institute*, pages 325 – 332, 1990. page 122
- [90] K.T. Aung, M.I. Hassan, and G.M. Faeth. Effects of pressure and nitrogen dilution on flame/stretch interactions of laminar premixed h<sub>2</sub>/o<sub>2</sub>/n<sub>2</sub> flames. *Combustion and Flame*, 112:1–15, 1998. page 122
- [91] M. Matkowsky and Matalon B. J. Flames as gas dynamic discontinuities. *Journal of Fluid Mechanics*, 124:239–259, 1982. page 123



- [92] C.K. Law, P. Cho, M. Mizomoto, and H. Yoshida. Flame curvature and preferential diffusion in the burning intensity of bunsen flames. *Proceedings of the Combustion Institute*, 21:1803–1809, 1988. page 123
- [93] C. Tang, J. He, Z. Huang, C. Jin, J. Wang, X0 Wang, and H. Miao. Measurements of laminar burning velocities and markstein lengths of propane-hydrogen-air mixtures at elevated pressures and temperatures. *International Journal of Hydrogen Energy*, 33:7274–7285, 2008. page 126
- [94] C.J. Sun, C.J. Sung, L. He, and C.K. Law. Dynamics of weakly stretched flames: quantitative description and extraction of global flame parameters. *Combustion and Flame*, 118:108–128, 1999. page 126
- [95] S.C. Taylor. *Burning Velocity and the Influence of Flame Stretch*,. PhD thesis, 1990. page 126
- [96] O.L. Gulder. Laminar burning velocities of methanol, ethanol and isooctane-air mixtures. *Symposium (International) on Combustion*, 19:275–281, 1982. pages 134 and 145
- [97] D. Bradley, M. Lawes, and M.S. Mansour. Explosion bomb measurements of ethanol-air laminar gaseous flame characteristics at pressures up to 1.4 mpa. *Combustion and Flame*, 156:1462–1470, 2009. pages 134, 139, 140, 143 and 145
- [98] S.P. Marshall, S. Taylor, C.R. Stone, T.J. Davies, and R.F. Cracknell. Laminar burning velocity measurements of liquid fuels at elevated pressures and temperatures with combustion residuals. *Combustion and Flame*, 158:1920–1932, 2011. pages 134, 139, 140, 143 and 145
- [99] K. Eisazadeh-Far, A. Moghaddas, J. Al-Mulki, and H. Metghalchi. Laminar burning speeds of ethanol/air/diluent mixtures. *Proceedings of the Combustion Institute*, 33:1021–1027, 2011. page 134
- [100] A.A. Konnov, R.J. Meuwissen, and L.P.H. de Goey. The temperature dependence of the laminar burning velocity of ethanol flames. *Proceedings of the Combustion Institute*, 33:1011–1019, 2011. pages 135, 139 and 140

- [101] C. Ji and F.N. Egolfopoulos. Flame propagation of mixtures of air with binary liquid fuel mixtures. *Proceedings of the Combustion Institute*, 33:955–961, 2011.  
*pages 135, 138 and 139*
- [102] E. Varea, A. Vandel, V. Modica, and B. Renou. Laminar burning velocity and markstein length relative to fresh gases determination for isooctane-ethanol air flames. *23rd ICDERS, Irvine, USA, July 24-29, 2011*.  
*pages 136 and 139*
- [103] M. Metghalchi and J.C. Keck. Burning velocities of mixtures of air with methanol, isooctane, and indolene at high pressure and temperature. *Combustion and Flame*, 48:191–210, 1982.  
*pages 138 and 145*
- [104] F.N. Egolfopoulos, D.X. Du, and C.K. Law. A study on ethanol oxidation kinetics in laminar premixed flames, flow reactors, and shock tubes. *Proceedings of the Combustion Institute*, 24:833–841, 1992.  
*page 140*
- [105] G.I. Sivashinsky. Hydrodynamic theory of flame propagation in an enclosed volume. *Acta Astronautica*, 6:631–645, 1979.  
*pages 157 and 161*
- [106] C.K. Law. *Combustion Physics*. Cambridge University Press, 2006.  
*page 157*
- [107] L. He. Critical conditions for spherical flame initiation in mixtures with high lewis numbers. *Combustion Theory and Modelling*, 4:159–172, 2000.  
*page 157*
- [108] R.J. Kee, F.M. Rupley, and J.A. Miller. Sandia national laboratories report. SAND89-8009, 1990.  
*page 158*
- [109] Le Neindre. Conductivité thermique des liquides et des gaz. *Techniques de l'ingénieur*, (K427), 1998.  
*page 158*
- [110] J.O Hirschfelder, C.F Curtiss, and R B. Bird. *The Molecular Theory of Gases and Liquids*, volume 1st Edition. 1964.  
*page 159*

- 
- [111] F. Dinkelacker, B. Manickam, and S.P.R. Muppala. Modelling and simulation of lean premixed turbulent methane/hydrogen/air flames with an effective lewis number approach. *Combustion and Flame*, 158:1742–1749, 2011. *page 159*
- [112] C.K. Law and O.C. Kwon. Effects of hydrocarbon substitution on atmospheric hydrogen-air flame propagation. *International Journal of Hydrogen Energy*, 29:867–879, 2004. *page 159*